Iodine-Fed μACFT Engineering Model for CubeSats

D. van Paridon

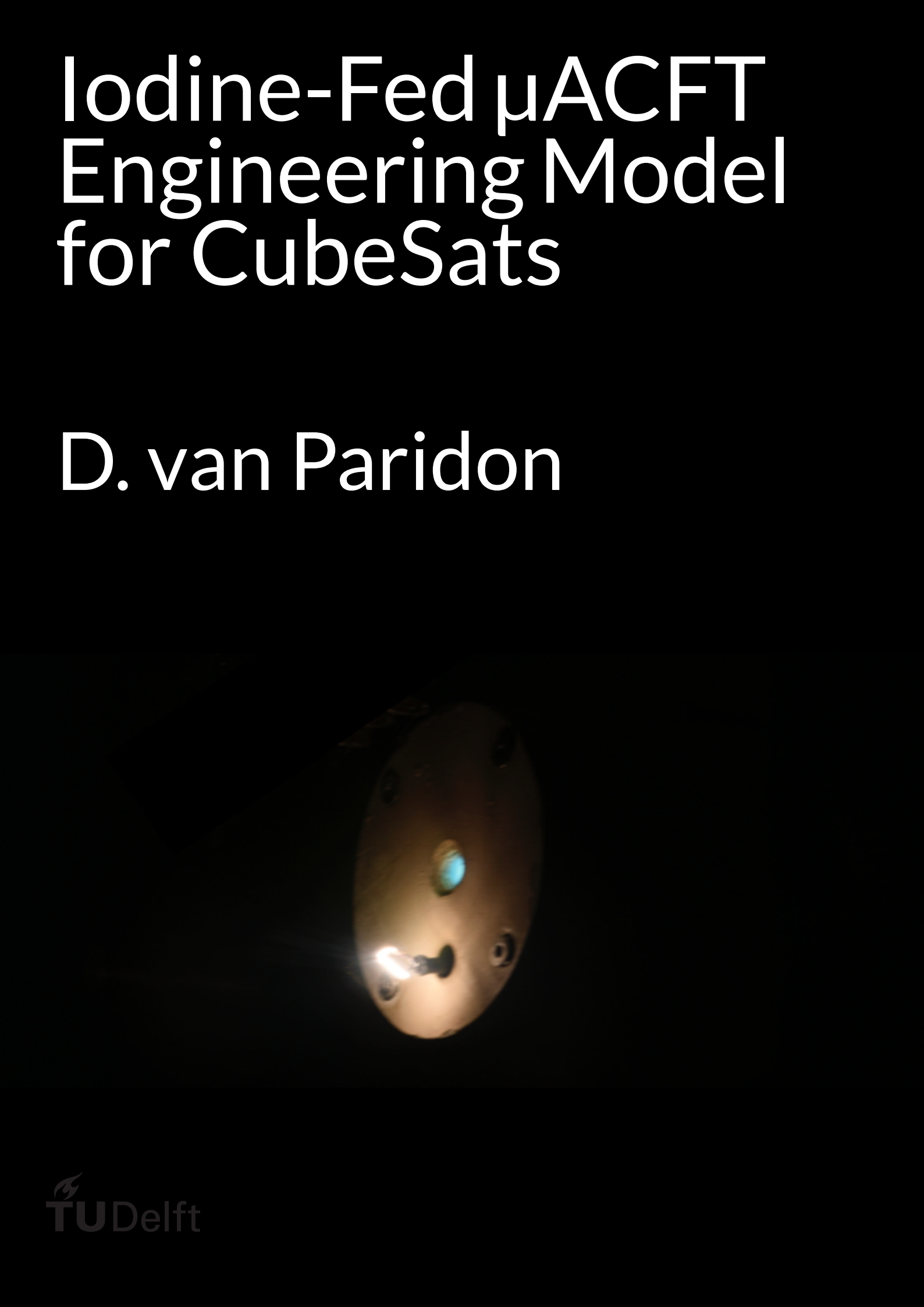

TU Delft

Iodine-Fed μACFT Engineering Model for CubeSats

by

D. van Paridon

to obtain the degree of Master of Science
at the Delft University of Technology,
to be defended publicly on May 13, 2019 at 2:30 PM.

Student number: 4701879
Project duration: August 1, 2018 – April 30, 2019
Thesis committee:

Ir. B.T.C. Zandbergen,	TU Delft, Committee Chair
Dr. A. Cervone,	TU Delft, Supervisor and Commitee Member
Ir. R. Noomen,	TU Delft, Committee Member

An electronic version of this thesis is available at `http://repository.tudelft.nl/`.

TU Delft

Preface

This document describes the research activities conducted over a period of eight months at the Laboratory for Enabling Technologies in Airbus Friedrichshafen. This thesis report is presented to the Delft University of Technology in order to complete the requirements for graduation from the MSc Aerospace Engineering program, with a specialization in Spaceflight.

I would like to acknowledge my project supervisors Dr. Franz G. Hey and Max Vaupel, as well as my academic supervisor Dr. Angelo Cervone for being mentors and providing good guidance during the project. I also extend my gratitude to the remainder of my colleagues at the Laboratory for Enabling Technologies and the Future Projects Department at Airbus, and at the Department of Aerospace Engineering in the Delft University of Technology for creating a pleasant and instructive working environment.

D. van Paridon
Airbus DS Friedrichshafen
Immenstaad am Bodensee, April 2019

Abstract

In the new space paradigm, CubeSats have become the go-to platform for researchers and industry developers across the world for gaining access to space. As CubeSat technologies are maturing, many developers are planning intricate and utilitarian missions for CubeSats. Many of these concepts involve formation flying or swarm dynamics, debris removal, and even deep space exploration. However in order for any of these missions to be realized in a long-term and sustainable way, the spacecraft will require propulsion systems.

This thesis describes the design, construction and testing of a miniature iodine-fed Advanced Cusped Field Thruster (μACFT) engineering model (EM) for the 3U+ CubeSat platform. With a dry mass of 280 g and a volume of 180 cm^3, the iodine μACFT EM is designed to fit inside of the tuna can extension of the 3U+ CubeSat structure. This form factor makes it incredibly small relative to other iodine thrusters. The measured thrust of the iodine μACFT is 227 - 254 μN, with a total system power consumption of 8.3 - 11.6 W. The small size and low power consumption make the μACFT the best suited iodine thruster candidate for the small 3U+ CubeSat platform.

Multiple distinct topics related to development of the μACFT engineering model are also explored in this the thesis. The fluidics of the two-stage iodine feed system are studied to create a thermodynamic model which can be used to predict the mass flow rate of the propellant as a function of temperature. A resonant DC/DC converter is designed and tested as a candidate for the power processing unit of the engineering model. The converter demonstrated inadequate performance, with respect to the power output and conversion efficiency which is linked to the simultaneous requirements on for a high voltage gain and low power consumption in the thruster. Lastly, a tungsten thermionic emitter cathode is verified as an effective option for neutralization of the exhaust plume.

Contents

List of Tables

List of Figures

Nomenclature

Acronyms

ACFT Advanced Cusped Field Thruster

AC Alternating Current

AHP Analytic Hierarchy Process

CAD Computer Aided Design

DC Direct Current

EMI Electromagnetic Interference

EM Engineering Model

EP Electric Propulsion

FHA Fundamental Harmonic Approximation

HEMPT High Efficiency Multistage Plasma Thruster

LET Laboratory for Enabling Technologies

LM Laboratory Model

MOSFET Metal Oxide Semiconductor Field Effect Transistor

O/C Open Circuit

PCB Printed Circuit Board

PWM Pulse Wave Modulation

RF Radio Frequency

RPA Retarding Potential Analyzer

RQ Research Question

Constants

σ Stefan-Boltzmann Constant

ε_0 Permittivity of Free Space

e Elemental Charge

h Planck Constant

k_B Boltzmann Constant

N_A Avogadro Number

R Ideal Gas Constant

Symbols

$\dot{m}$ Mass Flow Rate

η	Efficiency
γ	Secondary Electron Emission Fraction
μ	Adiabatic Invariant, Viscosity, or Gravitational Parameter
Ω	Right Angle of Ascending Node
ω	Frequency or Argument of Perigee
Φ	Flux
ϕ	Work Function
A	Area or Numeric Constant
a	Semi-major Axis
C	Capacitance
d	Diameter or Distance
e	Eccentricity
F	Force
f	Frequency
G	Gain
I	Current
i	Inclination
I_{sp}	Specific Impulse
J	Current Density
k_s	Specific Thermal Conductivity
L	Inductance or Length
L	Length
M or m	Mass
n	Turns Ratio
P	Power or Pressure
Q	Quality Factor
q	Charge
R	Resistance
T	Temperature
V	Voltage
v	Velocity
Whr	Watt Hour
Kn	Knudsen Number
PTTR	Power to Thrust Ratio

1 Introduction

Rapid development and miniaturization of technology, as well as commercialization of access to space have been defining characteristics of the space industry in the 21st century. This is a dramatic shift from the previous state of the industry, where commercialization was not economically viable and technological development periods spanned decades. The new paradigm is often referred to as "new space". It is in this new climate that the CubeSat has emerged as an incredibly popular standard platform with universities and private companies across the world for small experimental space missions. The CubeSat, invented in 1999 as a joint effort between the California Polytechnic State University and Stanford University's Space Systems Development Lab, prescribes a generalized approach to constructing nanosatellite (a class of spacecraft weighing between 1 - 10 kg) [67]. The approach put forward in the CubeSat design standard bases the entire spacecraft design around 10 cm cubes called U's (short for units). A variety of typical CubeSat configurations is shown in Figure 1.1. The small size of the CubeSat poses a challenge for spacecraft developers as both the power and volume available for components and instruments is extremely limited in comparison to a more traditional satellite platform. Yet the accessibility to CubeSat components and design resources has lead to an enormous up-swell in the number and frequency of nanosatellites launched into Earth orbit over the past two decades.

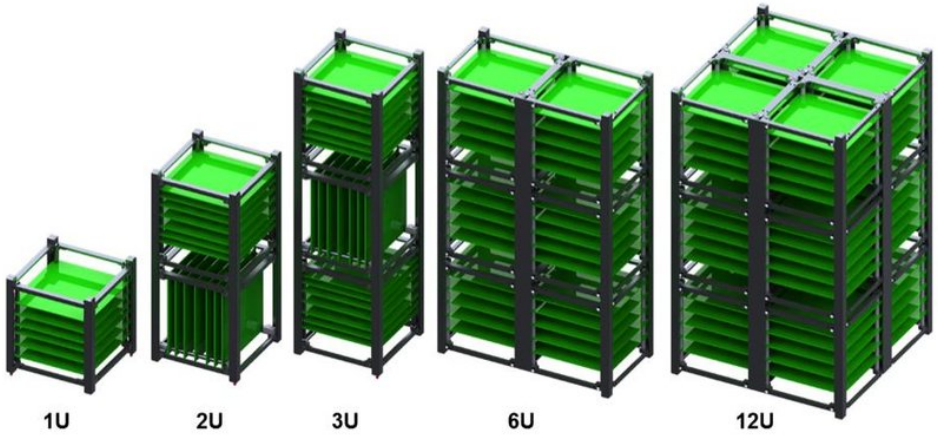

Figure 1.1: Typical CubeSat configurations based on 10 x 10 cm cubic units (U) [56]. Larger configurations such as the 3U and 6U are popular.

1.1. Motivation

As the number of nanosatellites launches continues to increase, space mission designers are looking for innovative ways to utilize CubeSats. A recent example is the Mars Cube One from NASA, which was launched alongside the InSight probe. The CubeSat performed a flyby of the planet and provided a communications relay to the probe during its entry descent and landing [71, 90]. Although Mars Cube One was the first CubeSat mission to leave geocentric orbit, many other CubeSat designers have similarly ambitious objectives.

Because of this, CubeSat missions of the future are likely to be more utilitarian than experimental. Other popular utilitarian nanosatellite mission concepts often involve large fleets known as swarms. A highly functional or long lasting CubeSat swarm would require performing orbital maneuvers. Nearly all CubeSat missions which will perform some useful function, whether that is forming a stable long-term Earth observation or communications swarm, transferring to the Moon, or deorbiting debris in orbit around Earth, will require a propulsion system.

Propulsion is a classical space engineering subsystem which can be found on virtually every modern full sized spacecraft. Typically, propulsion systems can be differentiated into two broad categories, electric and chemical. Electric propulsion (EP) is a method of generating thrust by transferring energy which is stored electrically into propellant which is expelled in order to transfer momentum to the body of a spacecraft. This transfer of momentum is what generates a thrusting force on the spacecraft. Using electrical energy to energize the propellant contrasts with chemical propulsion systems, in which the energy required to generate thrust is stored within the chemical structure of the propellant. A key advantage of the EP configuration is that energy storage does not monotonically decrease over time as propellant is expelled, since electrical energy can be regenerated. The concept of using an electrostatic potential difference to generate thrust can be dated back to 1917 with the invention credited to Robert H. Goddard via USA patent #1,363,037 [18]. However, the concept was not incorporated into space technology until the 1960s, when the onboard power available in satellites reached a level that enabled the use of EP systems. The first in-space demonstration of EP thrusters was performed in 1964 by NASA with the Space Electric Rocket Test 1, and by the Soviets with the Zond-2 satellite [66].

In modern times, many EP thruster configurations have emerged to meet important needs in space engineering, such as station-keeping for low-Earth orbit [36, 113] and geo-stationary [34, 62] satellites for communications or Earth-observation applications. More advanced concepts are proposed as well as, such as high-precision maintenance of spacecraft orientation such as in the LISA mission [12, 121]. Aside from applications in large satellites, electric propulsion is also being targeted for miniaturization in order to generate a suitable solution for propulsion of nanosatellites [59]. Over the past ten years, since the launch of the first CubeSat featuring a propulsion system (CANX-2, 2008 [119]), a significant amount of attention has been turned towards development of micropropulsion thrusters, generally based on electric propulsion, for CubeSat applications [58, 69].

Satellite electric propulsion systems are typically categorized into the following three types, [28].

1. *Electrothermal*: electricity is used to vaporize solid propellant or heat gaseous propellant, which expands through a nozzle to convert the thermal energy into kinetic energy, transferring momentum to the spacecraft.

2. *Electrostatic*: electricity is used to ionize the propellant and an electrostatic potential is used to accelerate the ions, which subsequently transfer their momentum to the spacecraft.

3. *Electrodynamic*: electronically ionized propellant is accelerated via a combined electric and magnetic field, and momentum is transferred to the spacecraft from the ejected ions.

In general, electrostatic and electrodynamic thrusters generate a plasma and use electromagnetic forces to propel the charged particles in the plasma, generating thrust. The general structure of an electrodynamic or electrostatic thruster includes a power processing unit for generating the accelerating potential and/or magnetic fields, a propellant feed system for supply fuel, a thruster chamber for accelerating ions, and a neutralizer for eliminating charge buildup on the spacecraft. On the other hand, the electrothermal thrusters rely on thermodynamic forces to accelerate the propellant. An electrothermal thruster is typically consists of a propellant feed system, a thermal management system, and a nozzle for generating thrust. Table 1.1 shows a brief overview of EP thruster concepts which are currently under development in the field of micropropulsion. Many of the thrusters listed are aimed at the CubeSat market, or have strong potential to be adapted for a nanosatellite platform.

Table 1.1: Summary of a variety of electric propulsion thruster types currently under development [58, 68, 69, 116].

Thruster	**Type**	**Propellant**	**Example**
Colloid (Electrospray)	Electrostatic	Cs, $C_3H_8O_3$	[46, 120]
Field Emission (Electrospray)	Electrostatic	Cs, In	[8]
Nanoparticle Field Extraction	Electrostatic	Au	[70]
Hall Effect	Electrostatic	Xe, I_2	[24, 78]
Cusped Magnetic Field	Electrodynamic	Xe, I_2	[27, 52]
Pulsed Plasma	Electrodynamic	PTFE, PFPE, H_2O	[7, 19, 87]
Vacuum Arc	Electrodynamic	Al, C, W, Bi, Cr	[64, 88]
Radio Frequency	Electrothermal	Xe, I, H_2O, Ar	[10, 80]
Resistojet	Electrothermal	R134a, NH_3, SO_2, H_2O, N	[14, 101]
MEMS Gas	Electrothermal	Im, In, BF_4, C_4H_{10}	[55]
Microcavity Discharge (Electrospray)	Electrothermal	Al, AL_2O_3	[13]

Throughout the brief history of electric propulsion systems which have been flown on CubeSats, electrothermal and cold gas thrusters have been popular. This is because of the relative simplicity of the devices, the relatively good power to thrust ratio, and small size. However the cusped field thruster, an electrodynamic system, shows great potential for future CubeSat missions for a variety of reasons. It is a highly scalable technology, which allows for miniaturization to the degree that it is compatible with small CubeSats (3U or less) [43]. The design of a cusped field thruster is of the same level of complexity as a cold gas thruster, but offers a significant advantage in propellant efficiency [41]. Additionally, the fact that the system can operate on solid propellant (iodine) means that opportunities for miniaturizing the system extend to include the entire propellant feed system as well. Solid iodine as propellant can be stored in a small unpressurized reservoir, leading to volume savings in the thruster design. It is also inexpensive and readily available, making the cost to benefit ratio of adding this propulsion system to a CubeSat quite low. Furthermore, at low thrust levels the cusped field concept consumes very little power, while still providing enough thrust to be compatible a variety of mission options [91].

The Laboratory for Enabling Technologies (LET) at Airbus Friedrichshafen develops cusped field thruster systems for low thrust applications. The thrusters built and tested at the LET are a variation of the High Efficiency Multistage Plasma Thruster (HEMPT), which was previously known as the Next Generation µHEMPT [41], but now referred to as the Advanced Cusped Field Thruster (ACFT) [111]. The ACFT system is associated with technological developments for the LISA mission [12], which is a space-based gravitational wave detector based on a laser interferometer with an arm length on the order of millions of kilometers [41]. System requirements for the LISA mission call for a µN - mN range propulsion system for performing the small attitude adjustments necessary for the mission. In recent years, multiple scaled-down ACFT systems have been tested to demonstrate the viability of the concept for CubeSat applications, culminating in the development of the first engineering model (EM) of a CubeSat ACFT device in 2017 [91]. However, as the EM used xenon propellant, the outlook for integrating the thruster into a small CubeSat system could be greatly improved by switching to solid iodine propellant.

Currently, iodine is seen by many electrodynamic thruster developers as a desirable alternative to xenon propellant for a variety of reasons. Key reasons include a significant decrease in propellant cost, and no need for a pressurized fuel tank since the propellant is solid at standard storage conditions. Despite this, development of iodine-based electric thrusters is still an emerging field with only a few systems having been tested and discussed in scientific literature by NASA/Busek, the LET, and University Giessen [45, 49, 75, 103, 111]. The benefits to cost, mass and feed system complexity are sure to draw CubeSat developers toward iodine-fed cusped field thrusters as it has the potential to allow nanosatellites to perform more complex and useful missions.

1.2. Research Outline

The focus of this thesis is development of a iodine-fed cusped field thruster engineering model for CubeSats based on the existing ACFT concept at Airbus Friedrichshafen. All activities of this project take places at the LET at Airbus Friedrichshafen.

The European Cooperation for Space Standardization defines an engineering model as a "flight representative model in terms of form, fit and function used for functional and failure effect verification" [35]. The key challenge of the project is creating an operating ACFT system which complies with the tight power and volume constraints of the CubeSat platform.

In the context of V-model systems engineering, which is illustrated in Figure 1.2, the activities in this thesis mostly take part at the tip of the V. During this stage of the process, component design, fabrication and procurement, and testing are the focus. Synthesis of system requirements is also a part of this project. The approach taken in development of the engineering model falls in line with the so-called new space approach often associated with CubeSat development. In the new space design approach, simple and inexpensive designs are preferred, and the use of commercial off-the-shelf (COTS) components is common, despite the relative risk of failure.

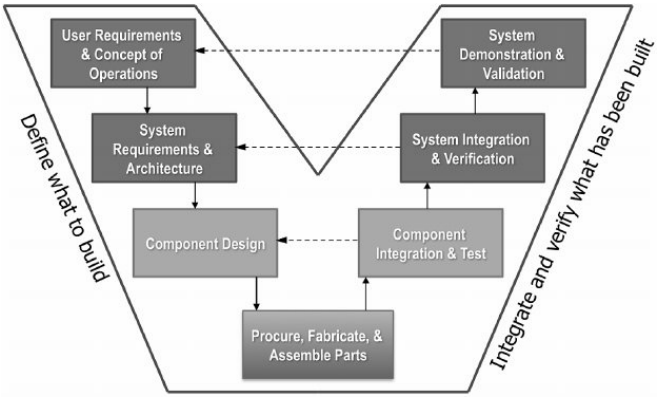

Figure 1.2: V-model of systems engineering. [86]. Activities in this thesis take place in the tip of the V, at component design, fabrication, procurement, assembly and testing.

Research Objective The engineering model, hereby referred to as the μACFT or μACFT EM, will be used to investigate the compatibility of the miniaturized ACFT system using iodine as propellant with a CubeSat system. The μACFT system will also be a demonstration of the miniaturization of electrodynamic thrusters. Characterization of the μACFT performance will help to understand the capabilities, advantages and shortcomings of this miniature thruster architecture. In addition, the measurements can be compared to a legacy of measurements made at the LET for miniaturized ACFT systems using xenon to determine whether the choice of propellant has an effect on overall thruster performance. The research objective is summarized in the statement OBJ-1.

> **OBJ-1**: To investigate the viability of iodine as a propellant alternative (to xenon) for ion electric propulsion systems in the context of CubeSat applications by constructing and testing a fully integrated engineering model of an iodine-fed μACFT device.

Research Questions In pursuit of the research objective of this thesis, multiple research questions will also be addressed. Research questions were drafted following a large review of the literature covering CubeSat electric propulsion, iodine electric propulsion and iodine feed system design, high efficiency DC/DC converters, spacecraft thermal control technologies, as well as theoretical and experimental methods for characterizing ion thruster performance. Key issues which remained following the literature study included the predicting the rate of generation and flow of iodine vapour in the thruster feed system, and the performance which could achieved with a high gain and low power DC/DC converter based on the high efficiency LLC resonant converter topology. Additionally, a simple and low power solution to neutralization of the exhaust plume which comply with the strict requirements of the CubeSat platform and the new space design philosophy is desired. In previous work at Airbus Friedrichshafen, thermionic emitters were identified and explored as a potential design choice over the commonly used, but bulkier and more complex, gridded extractors, hollow or radio frequency cathodes [108]. Lastly, the question of the performance in terms of thrust, specific impulse and power consumption, of a miniature (< 1 kg) iodine electrodynamic thruster is unknown at the time of writing.

With these issues, the project objective and motivation in mind, the following research questions were drafted for this thesis project:

RQ-1: How does the thruster performance compare in the context of the legacy of miniaturized ACFT devices?

RQ-1A: How does the device compare relative to other iodine thrusters?

RQ-1B: How does the performance compare to other CubeSat thruster alternatives?

RQ-1C: Aside from propellant choice, what other aspects of the μACFT design impact the performance?

RQ-2: What flow regime(s) characterizes the iodine vapour feed system?

RQ-2A: What is the sublimation rate of iodine in the context of the feed system? To what extent is it described by the Langmuir sublimation model?

RQ-2B: What is the mass flow rate through the thruster?

RQ-3: What performance can an LLC resonant converter achieve in the proposed low-power, high-voltage application?

RQ-4: Can a thermionic cathode technology effectively neutralize the thruster ion plume?

Project Planning This activities described in this thesis take place over a period of six months. Including the time required for reviewing literature and project planning, the entire thesis period lasts eight months. The planning for the project is organized around the research questions. The key tasks associated with each research question are organized into a workflow diagram. Then each task in the workflow diagrams is systematically broken down into sub-tasks in a work breakdown structure. The tasks of the workflow diagrams and the associated sub-tasks are then sequenced on the project timeline using a Gantt chart. The workflow diagrams, work breakdown structures and Gantt chart can be seen in Appendix A.

2

Fundamentals

In this chapter is an introduction to all the foundational concepts and equations used in the development of the iodine-fed μACFT and addressing the research questions which guide the thesis. First, an introduction to the basics of electric propulsion is necessary. A description of the ACFT concept is also provided, alongside definitions and relevant concepts from plasma physics. Furthermore, the particular details and benefits of iodine electric propulsion are discussed. Following on are dedicated sections for iodine feed system fluidics, LLC DC/DC converter theory and design, and thermionic cathode theory.

2.1. Electric Propulsion

The decoupling of the energy source for thrust from the propellant in electric propulsion (EP) has the advantage of increasing the energy density of the thruster system overall, resulting in a smaller subsystem footprint. In an ion EP system, thrust is typically generated by ionizing a propellant gas and accelerating the ions across a potential difference (V_b) of 1 kV or more, which results in ion exhaust velocities (v_i) on the order of 30 km/s [68]. The higher exhaust velocities achieved with EP systems imply that a smaller mass flow rate is required to achieve thrust and thus long term sustainable operations are possible. Due to the electrical energy transfer into the ionized propellant, EP systems are typically characterized by lower thrust (F_t) levels and higher specific impulse (I_{sp}) than chemical propulsion system counterparts. The characteristically high specific impulse of EP thrusters is achieved with large potential differences which accelerate the ionized propellant to high speeds, and the low thrust is a result of the limitations on the available power of the system. This is demonstrated in the following derivations.

The key relationships which define the thrust and specific impulse of an EP system, metrics that are generally used to characterize propulsion system performance, are:

$$F_t = \dot{m}_i v_i \tag{2.1}$$

$$I_{sp} = \frac{F_t}{\dot{m}_p g_0} \tag{2.2}$$

where $\dot{m}_i$ is the mass flow rate of ionized propellant, $\dot{m}_p$ is the flow rate of all propellant, and $g_0 = 9.81$ m/s^2 is the gravitational acceleration on Earth. Overall, the specific impulse for an EP system is expected to fall within the range of 100 - 10000 s [66]. In the case of an ion thruster, such as the ACFT, a differentiation is made between propellant flow rate and ionized propellant flow rate since only a fraction of all fuel is ionized when ejected. This quantity is relevant to the device performance since only the ions, and not the neutral propellant molecules, are accelerated through the thruster chamber. The mass efficiency is introduced to quantify this fraction:

$$\eta_m = \frac{\dot{m}_i}{\dot{m}_p} \tag{2.3}$$

such that $F_t = \eta_m \dot{m}_p v_i$ and $I_{sp} = \eta_m \frac{v_i}{g_0}$.

The specific impulse is a metric which describes the propellant efficiency of a thruster, ie. the ratio between the thrust provided to the rate of propellant usage. There is a fundamental trade-off between the specific impulse and thrust generated by a thruster. This is demonstrated by first defining the ionized propellant exhaust velocity due to acceleration across an electrostatic potential V_b which exists across the exhaust beam:

$$v_i = \sqrt{\frac{2qV_b}{M_i}} \tag{2.4}$$

where M_i and q are the mass and charge of the ions. When considering the momentum transferred to the spacecraft, the term η_d is included to take into account the divergence efficiency of the thruster:

$$\eta_d = \cos\theta \tag{2.5}$$

where θ is the average exit half-angle of the ions relative to the axis of symmetry of the thrust chamber. This measure quantifies the efficiency of momentum transfer to the spacecraft such that:

$$F_t = \dot{m}_i v_i \rightarrow \eta_d \eta_m \dot{m}_p v_i$$

Due to the kinetic motion of charged particles in the expelled propellant, there exists a current in the exhaust beam given by:

$$I_b = q\frac{\dot{m}_i}{M_i} \tag{2.6}$$

where q is the charge of the ions. Substituting Equations 2.4 and 2.6 into Equation 2.1 leads to the following relationship between thrust and total power:

$$F_t = \sqrt{\frac{2M_iV_b}{q}}I_b = \sqrt{\frac{2M_i}{qV_b}}\eta_e P_t \tag{2.7}$$

where η_e is the overall power efficiency of the thruster, which measures the rate of conversion of power consumed by the thruster (P_t) into electrical power in the propellant exhaust beam (P_b):

$$P_b = V_b I_b = \eta_e P_t \tag{2.8}$$

The electrical efficiency can be broken down into a discharge, η_i and acceleration efficiency, η_v, such that

$$\eta_e = \eta_i \eta_v \tag{2.9}$$

where

$$\eta_v = \frac{V_b}{V_a} \tag{2.10}$$

$$\eta_i = \frac{I_b}{I_a} \tag{2.11}$$

Lastly, there is the overall thruster efficiency, η_T. Noting that the total thrust generated is directly proportional to η_i, η_m and η_e, the total efficiency is calculated as the product of these:

$$\begin{aligned}\eta_T &= \eta_d \eta_m \eta_e \\ &= \eta_d \eta_m \eta_i \eta_v\end{aligned} \tag{2.12}$$

Considering Equations 2.4 and 2.7, one can see a trade off between I_{sp} and F_t. By using lighter ions (smaller M_i), the specific impulse increases at the expense of thrust. Alternatively, thrust can be improved by increasing the mass-to-charge ratio of the ions, at the expense of specific impulse. However, clearly both the thrust and specific impulse increase with the electrical power applied. Assuming singly ionized xenon is used as fuel, a power input of 100 W with a beam voltage of 1 kV and ideal power conversion at the anode ($\eta_e = 1$), a thrust of 5 mN can be achieved.

The thrust level scales linearly with power and thus theoretically the thrust which can be applied is unbounded. Note that the linear trend in increasing thrust with increasing power is characteristic of ion propulsion technologies but not necessarily of electric propulsion in general [54]. Furthermore, non-linearities may arise in relation to the efficiencies. The unbounded characteristic is in contrast to chemical propulsion thrusters in which the internal energy of the propellant is fundamentally limited [60]. However with standard spacecraft bus power limitations, large thrust levels (beyond multiple Newtons) cannot be realistically achieved.

Another metric which is used to describe the performance of EP systems is the power-to-thrust-ratio:

$$\text{PTTR} = \frac{P_t}{F_t} \tag{2.13}$$

which typically measures the electric power, P_t, which is consumed in the thruster for each milli-Newton of thrust generated. State of the art EP systems can achieve a PTTR between 20 - 70 W/mN [41] (PTTR = 20 W/mN demonstrated in the previous xenon example), where a lower PTTR is desirable due to the limitations on available power onboard a spacecraft.

Aside from the acute performance parameters of the thruster, the overall performance in mission context must be considered. The fundamental equation which defines the performance of a thruster in the context of space travel and orbital maneuvers is the classical rocket equation, originally derived by Tsiolkovsky in 1903:

$$\Delta v = v_i \ln\Big(\frac{M_{sc} + M_p}{M_{sc}}\Big) \tag{2.14}$$

where M_{sc} is the total dry mass of the spacecraft, M_p is the total mass of the propellant used, and Δv is the total velocity increment imparted on the spacecraft by the thruster. The Δv capability, and thus overall utility of a thruster is directly related to the total propellant mass and it's output velocity in operation.

2.1.1. µACFT Concept

The µACFT concept is an ion propulsion system consisting of a cusped magnetic field generated by permanent magnets and a high potential electric field [44]. The cusped nature of the field results in the formation of magnetic cells which confine electrons near the magnetic poles at the cell boundaries. Confinement is based on the concept of a magnetic mirror or magnetic trap from plasma physics. The magnetic mirror is a result of the principle of first adiabatic invariance in a plasma, which states that the ratio of the kinetic energy of a particle (in the direction perpendicular to the magnetic field vector) to the magnetic field strength is a constant, μ:

$$\mu = \frac{m v_\perp^2}{2B} \tag{2.15}$$

where m is the mass of the particle, $v_\perp$ is it's velocity in the direction perpendicular to the magnetic field lines, and B is the magnitude of the magnetic field.

The effect of adiabatic invariance is such that as particles enter a region with high magnetic field intensity, the velocity of that particle in the direction perpendicular to the field must increase as well. By conservation of energy, this implies that the velocity of the particle in the direction along the field line is reduced. If the energy of the particle is low enough, it can be completely stopped from proceeding into the high magnetic field region. Ultimately, in a periodically cusped magnetic field such as the one in the ACFT, net effect is particles which are confined between two cusps, where the field is strongest.

Electron confinement results in negative space charge which contributes to ionization and acceleration of the propellant as it traverses the chamber. Positive ions are generated inside and accelerated to toward the exit of the chamber via a large potential difference applied between the anode at the entrance to the chamber and the cathode at the exit of the chamber. The cathode emits electrons collected at the anode to complete the circuit and neutralize the ion exhaust plume, preventing negative charge build up on the spacecraft. Figure 2.1 shows the a schematic diagram of the magnetic cell configuration.

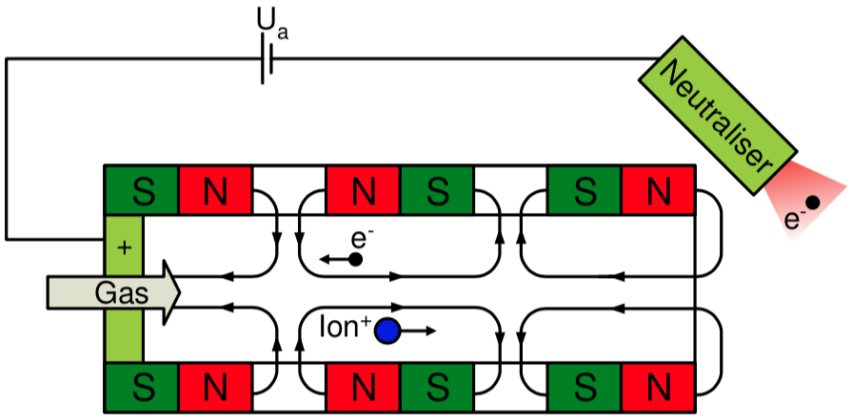

Figure 2.1: Diagram of cusped field thruster concept which is the basis of the μACFT magnetic cusped field thrust chamber design [41].

Due to the use of a magnetic field for confinement of the plasma in the chamber, an important parameter to consider in design of a μACFT system is the Larmor radius, r_L of the particles in the plasma:

$$r_L = \frac{m v_\perp}{|q|B} \tag{2.16}$$

where q is the charge of the particle. The Larmor radius, also known as gyro or cyclotron radius, is the radius of the circular motion undergone by charged particles travelling in a uniform magnetic field. The rate at which particles circulate is given by the Larmor frequency, ω_L:

$$\omega_L = \frac{|q|B}{m} \tag{2.17}$$

Highly charged, low mass particles oscillate much faster and with a much smaller radius. In order to avoid excessive collisions of the electrons and ions in the plasma with the walls of the chamber, the magnetic field amplitude should be as high as possible. The lifetime of the ions in the chamber is typically shorter than the period of the Larmor oscillations due to the large electrostatic force accelerating them toward the chamber exit. Thus the main concern is electrons, which dwell in the chamber longer due to confinement at the magnetic poles. In principle, the radius of the chamber should be larger than the Larmor radius of electrons for the provided magnetic field strength to avoid excessive losses to collisions with chamber walls.

Another effect from plasma physics which influences the performance of the thruster is E-cross-B drift. In general, when an external force is applied to a particle gyrating in a uniform magnetic field, the center point of the the particles circular motion begins to drift so long as the applied force is not parallel to the magnetic field lines. In the case of E-cross-B drift, the applied force is the electrostatic Lorentz force. The velocity with which the center point drifts is given by:

$$\vec{v}_d = \frac{\vec{E} \times \vec{B}}{qB^2} \tag{2.18}$$

Since both magnetic and electric fields play a significant role in the μACFT concept, the E-cross-B drift motion of the plasma can impact the performance and overall functioning of the thruster. For instance, at the cusp-points of the thruster, where the magnetic field and electric field are perpendicular, the E-cross-B drift is forcing ions toward the chamber walls.

The final effect from plasma physics which is related to the dimensions and performance of the μACFT is Paschen's law. The law is used to predict the electric potential required to initiate a plasma breakdown between two electrodes in a gaseous medium. The so called breakdown voltage V is described by the equation:

$$V = \frac{BPd}{\ln(APd) - \ln\left(\ln(1 + \frac{1}{\gamma}\right)} \tag{2.19}$$

where P is the pressure of the medium, d is the gap distance over which the arc of the plasma breakdown traverses, γ is the rate of secondary electron emission by ions in the arc, and A and B are the Townsend coefficients which empirically fit the relation to a given gaseous medium. When plotting the breakdown voltage versus the product pd, there is a minimum which occurs at $Pd = \frac{2.71828}{A}\ln(\frac{1}{\gamma} + 1)$.

2.1.2. Iodine Electric Propulsion

In the case of chemical propulsion systems, the choice of propellant is very closely linked to the thermal and chemical properties of the substance, as well as the storage density. However in electric propulsion systems, the selection of propellant is also based on various other properties such as corrosiveness, atomic or molecular mass, ionization and dissociation potential, as well as melting and boiling temperatures. For example, Equation 2.7 shows that thrust is maximized if an ionic propellant with a high mass-to-charge ratio is selected. Generally, xenon has been a favoured propellant for ion propulsion due to it's relatively high mass-to-charge ratio and it's inert gaseous state at standard storage conditions. Although pressurized vessels are required to store xenon propellant, there is significant space-heritage as it has long been an industry standard. However, in the case of CubeSat applications, pressurized gas propellants are highly undesirable due to strict launcher requirements on secondary payloads. In response to this specific constraint on CubeSat missions, a search for fuels which could be effective alternatives to the market-established xenon began, led to a great extent by NASA and Busek.

In August 2003, the first United States patent was issued to R. A. Dressler et al. for an iodine-fed electric propulsion thruster [32]. In the following decade, iodine as emerged as a favoured alternative fuel to xenon in Hall thrusters [30]. During that time, Busek and NASA have been collaborating on iodine-fed Hall thruster development with the objective of targeting two niche applications: very low power small satellites and high power exploration-class EP systems [30]. The joint developments are based around retrofitting of the Busek Hall thruster designs to incorporate iodine as propellant [49, 99], and design of a seperate gridded radio-frequency ion thruster (RIT) [105]. The developments will culminate in the proof-of-concept missions, incorporating the iodine thruster technologies, called iSAT and LunarCube [29, 104]. The iSAT mission is based on a 12U CubeSat architecture flying a BHT-200-I thruster (modified from the BHT-200 xenon-fed model) from Busek. Performance of the iodine-fed propellant system is reported to be similar to the xenon-fed counterpart [74, 76]. The Physikalisches Institut at University Giessen has also demonstrated performance testing using both xenon and iodine in the RIT-10 thruster from Justus Liebig University, with the former performing better at higher mass flow, and the latter at lower mass flow [45].

As the μACFT system is also an electrodynamic thruster, the propellant compatibility is similar to that of the other iodine thrusters. This is promising as using iodine would be an advantage of the μACFT for CubeSat missions. Adaption of the current μACFT device models to accommodate iodine as propellant is mostly centered around the feed system. However, the differences in other factors of the thruster design and performance should be observed when switching to iodine propellant.

Figure 2.2: Busek BHT-200-I thruster firing using iodine propellant and xenon gas RF cathode neutralizer. The yellow color is characteristic of the iodine plasma.

The physical properties of the propellant play a crucial role in the operation of an ion thruster. The ideal propellant for an ion propulsion system on a CubeSat platform should have the properties listed in Table 2.1. A propellant which meets these criteria can be stored in a compact tank, converted into an ionized vapour at low energy cost, and can provide a high thrust level per ion. Some potential propellant candidates which subscribe to these requirements, to differing degrees, are shown in Table 2.2.

Table 2.1: Properties which make a propellant excellent for electric propulsion on a CubeSat platform.

Property	**Reasoning**
Low ionization potential	A lower ionization potential implies that particles are ionized more easily and less energy overall is consumed in the process of generating ions. However a larger potential for higher order ionization is desirable to keep charge to mass ratio low.
High atomic mass	A higher atomic mass implies that a greater amount of momentum is transferred to the spacecraft when the ions are accelerated out the thruster.
Low boiling point	A lower boiling point implies that a lower heat energy is required to convert the propellant to a gaseous state or to maintain it in a gaseous state. However, with a boiling point above room temperature, the propellant can be stored as a solid.
High vapour pressure	A high vapour pressure implies that propellant continues to evaporate at a high rate at a given pressure compared to a propellant with a lower vapour pressure.
High storage density	A high storage density implies that the a high total propellant mass can be stored in a propellant reservoir with a small total volume.

Table 2.2: Comparison of properties of xenon and alternative propellant options at standard conditions [6, 30, 89, 99, 114].

Element	**Iodine**	**Xenon**	**Bismuth**	**Magnesium**
Atomic Mass [AMU]	126.9	131.3	209.0	24.3
First Ionization Potential [eV]	10.5	12.1	7.3	7.6
Boiling Point [°C]	184.3	-108.1	1564	1091
Melting Point [°C]	113.7	-111.8	271.4	650.0
Melting Point Vapor Pressure [mbar]	129	830	11.8	4.08
Storage Density [g/cm^3]	4.9	1.6	9.8	1.7

Although iodine does not have the distinct advantage in each of the properties mentioned, it is the combination of it's properties that make it a favoured propellant option for CubeSats applications. Specific arguments for iodine usage include it's comparable molecular mass to xenon, a relatively low ionization potential and boiling temperature, and a moderate vapour pressure (meaning it continues to vaporize quickly at moderate pressures). Another advantage of iodine is that it is relatively inexpensive, and particularly cheap in comparison to xenon. Perhaps most importantly, iodine is in a solid state at standard atmospheric conditions, meaning no pressurized vessels are required to store the propellant. However the downside of this feature is that the entire feed system must be heated to generate vapour and to ensure it does not deposit and clog the feedlines. Heating of the feed system will cost extra power, which is typically limited on CubeSats. Furthermore, management of the excess heat is necessary. Iodine vapour can be corrosive to both materials and humans, meaning it is critical to design a feed system which avoids any leaking, and incorporates robust corrosion resistant materials.

2.2. Feed System Fluidics

The pressure and mass flow rate of a typical gas-fed thruster feed system are set by a mass flow controller. This device releases the propellant from a pressurized vessel, directly setting the mass flow rate and pressure in the feed lines. However in the case of an iodine-fed thruster, the solid propellant must be converted to a solid state and thus an additional step is added to the feed system design concept. In the following section, the basic theories governing the rate of sublimation of a material is described so that the rate of propellant generation can be characterized in the μACFT device. Furthermore, the principles of flow regime are introduced so that the rate of propellant flow through the feed system can be estimated in the case that no mass flow controller is present.

Evaporation The sublimation or evaporation rate of a material at a given temperature is directly related to the vapour pressure of the material at that temperature [45, 65]. The vapour pressure of a material is the pressure exerted on the surface of a solid when that solid and it's surrounding gaseous environment are at equilibrium in terms of exchanging particles. The Antoine equation is a commonly used empirical relationship which describes the vapour pressure of a substance as a function of temperature [100]:

$$\log P_{vap} = A - \frac{B}{T+C} \tag{2.20}$$

Where for iodine, $A = 3.36429$, $B = 1039.159$, and $C = -146.589$, validated for measurements in the range 40 - 180°C [98]. The mass evolution rate of solid granular iodine into vapour can be estimated using the Langmuir equation for quasi-steady sublimation [77]:

$$\dot{m} = \alpha A \sqrt{\frac{M}{2\pi RT}} (P_{vap} - P) \tag{2.21}$$

where α is the sticking ratio (typically assumed to be 1), A is the exposed surface area of propellant, M is the molecular mass of iodine, R is the ideal gas constant, P and T are the ambient pressure and temperature, and P_{vap} is the vapour pressure of iodine. An alternative relation, which describes the maximum molar flux of substance which is evaporating from its condensed form to its gaseous form, is the Hertz-Knudsen equation [83]:

$$\Phi = \frac{P_{vap} - P}{\sqrt{2\pi MRT}} \tag{2.22}$$

With the units of this equation converted so that it describes an evaporation mass flow rate, it becomes:

$$\dot{m} = N_A A M_{I_2} \frac{P_{vap} - P}{\sqrt{2\pi MRT}} \tag{2.23}$$

where N_A is the Avogardro number and M_{I_2} is the mass of a single iodine molecule. In principle these two different relationships describe the same phenomena, but they are defined on different principles. Derivation of the Langmuir quasi-equilibrium sublimation equation is predicated on the assumption that the number of particles condensing back into the material substrate is nearly equal to the number of particles escaping into the gaseous state [57]. On the other hand, the Hertz-Knudsen equation is derived as the limit on the rate of evaporation of a condensed material into a gas, a state which can sometimes be reached in vacuum conditions [83]. Therefore, as the difference between P and P_{vap} increases, the accuracy of the Hertz-Knudsen equation increases relative to that of the Langmuir equation.

Flow The mass flow rate of gas through a feed system is dependant on the geometry and pressure inside the feed lines. For the μACFT, the feed system will operate in a vacuum environment and thus the pressure inside the feed system may be very low. Gas flow in the very low pressure regime is typically referred to as rarified. Two parameters relating to rarified flow of iodine through the feedlines are the geometry of the piping and the Knudsen number, Kn, defined by [94]:

$$\mathrm{Kn} = \frac{k_B T}{\sqrt{2}\pi d^2 P L} \tag{2.24}$$

where d is the diameter of the piping, L is the characteristic length scale of the pipe.

Kn is generally used to differentiate between sub-regimes of flow. For Kn ≥ 1, the gas particles very rarely collide, and this is referred to as the free-molecular limit. When Kn < 0.01, the flow is characterized as laminar, or continuous. This is the flow regime which is most typical for gas or liquid feed systems at standard atmospheric conditions. Between the laminar and free-molecular regimes (0.01 < Kn < 1) there is a transition regime [61]. The mass flow rate of sublimated iodine flowing through the short tubes at the free-molecular limit (Kn ≥ 1) can be calculated analytically as [109]:

$$\dot{m} = \sqrt{\frac{\pi M}{32 k_B T}} d^2 P \tag{2.25}$$

In the vicinity of the free-molecular limit this analytic equation approximates the vapour flow through the lines. In the laminar flow limit, the mass flow through a circular pipe is given by the analytic relation:

$$\dot{m} = \frac{\pi d^4 \rho}{128 \mu} \Delta P \tag{2.26}$$

where μ is the viscosity of the gas, ρ is it's density, and ΔP is the pressure differential driving the flow. The viscosity can be approximated via Sutherland's formula:

$$\mu = \mu_0 \frac{(T/T_0)^{3/2}}{1 + T/T_0} \tag{2.27}$$

where $\mu_0 = 3.85 \pm 0.36 \times 10^{-5}$ kg/m·s and $T_0 = 417 \pm 41$ K are fitting parameters for iodine vapour [79]. The density of the vapour can be determined with the ideal gas law:

$$\rho = \frac{MP}{RT} \tag{2.28}$$

where R is the ideal gas constant. In the case that the gas flows through an orifice instead of a pipe, and the flow is laminar, it is described by the equation:

$$\dot{m} = C_v A \sqrt{2 \rho \Delta P} \tag{2.29}$$

where A is the cross-sectional area of the orifice and C_v is the dimensionless flow coefficient of the orifice.

Aside from mass flow rate, $\dot{m}$, another common way to express the amount of propellant travelling through the feed system is in a volumetric flow rate, $\dot{V}$. Mass flow rate and volumetric flow rate are linked through the equation of state:

$$P\dot{V} = \frac{\dot{m}}{M} RT \tag{2.30}$$

The volumetric flow rate of propellant is often measured in units of standard cubic centimeter per minute (sccm).

2.3. Resonant DC/DC Converter

A DC/DC converter is a device which is used to transform a known DC voltage signal input into a desired DC voltage signal output. In the case of the μACFT, a DC/DC converter is required to supply a high voltage to the thruster anode using only the CubeSat bus voltage (5 or 12 V) as input. Many different DC/DC converter topologies have been developed over the years for high-voltage applications such as connecting to the power grid, operating medical devices or video displays [81, 102, 117]. However in modern device-based applications the typical converter architecture consists of a bridge driving inverter acting as a switching regulator, followed by a high step-up transformer, a rectifier with a low-pass filter, and voltage multipliers (if necessary) to deliver the final DC voltage [115]. The switching regulator is not a fundamental element of a DC/DC converter, however it improves the efficiency and lowers the thermal load of the converter in comparison to a linear regulator, which requires a voltage drop and power dissipation in the regulation scheme.

Resonant converters were investigated extensively in the 80's and are a popular choice for modular DC converter applications. This is because of the resonant topology leads to very low switching losses. The concept of the resonant converter is based on the resonant inverter, a device which converts a DC voltage to a sinusoidal signal. Typically a switch network generates a square wave which is fed into a resonant circuit tuned to the fundamental frequency of the square pulse pattern [97]. In order to achieve DC/DC conversion, this sinusoidal signal passes through a transformer and rectifier.

Topology The entire family of resonant and multi-resonant converters is broad and difficult to describe exhaustively. Figure 2.3 shows an outline of the general structure of a resonant converter, and the signal transformation which takes place at each stage of the converter assuming a step-up transformer is used.

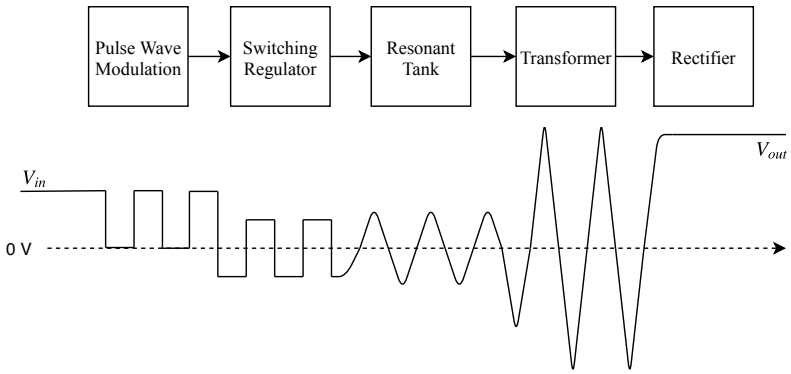

Figure 2.3: Block diagram schematic of simple resonant converter topology and signal transformation which takes place at each stage of the converter.

The pulse wave modulator is responsible for generating pulses at a frequency f_{sw}. In the switching regulator, this series of square pulses is converted into a square wave oscillating signal. The switching regulator achieves this with switching transistors, typically MOSFETs, in either a half bridge or full bridge configuration.

The two key identifying features of a resonant converter are the resonant tank elements (series or parallel, inductors and/or capacitors), and the switching scheme of the transistors (half bridge or full bridge). The first determines how many resonant frequencies the converter has, and what those frequencies are. The second identifier determines what the maximum gain and power throughput can be achieved with the converter.

The key to the relative high efficiency of the resonant converter topology is the resonant tank. Consisting of inductors (L) and capacitors (C) to generate a first or second order resonance, the resonant tank allows circulation of the input AC signal through the transformer and switching transistors with significantly reduced losses [118]. There are a variety of possible resonant circuit configurations, with two to three components combined in parallel, in series, or both.

Various popular LLC resonant converter topologies are summarized in Figure 2.4, along with a brief description of the different design options for switching regulator and resonant tank.

Half Bridge: Two transistors are alternately switched, and never on at the same time. Voltage gain is given by $V_{out} = V_{pk}\frac{T_{on}}{T_p}$, where T_{on} is the total on time of a single MOSFET, T_p is the switching period, and $V_{pk} = n(\frac{1}{2}V_{in} - V_{sw}) - V_{rec}$ with the voltage drops due to the switching regulator (V_{sw}) and rectifier (V_{rec}) taken into account.

Full Bridge: The number of MOSFET switch pairs is doubled, and as a result the full bridge configuration provides twice the output power of the half bridge at the same switching frequency. Furthermore, the gain of the resonant converter at the point $f_{sw} = f_r$ is doubled: $V_{pk} = n(V_{in} - 2V_{sw}) - V_{rec}$.

Series Resonant Tank: A capacitor and inductor in series with the transformer, generating a first order resonance.

Parallel Resonant Tank: One element of the resonant tank is in parallel with the transformer.

Series-Parallel Resonant Tank: A third element is introduced so that both the series and and parallel resonant tanks are implemented, generating a second order resonance.

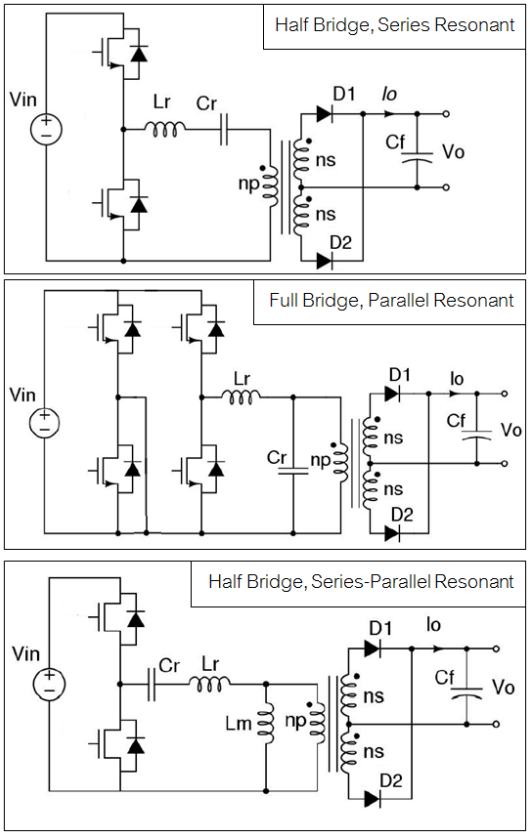

Figure 2.4: Common resonant converter topologies [118].

Power losses in the resonant converter topologies arise from many factors. These include the impedances of the resonant tank components, which scale with the switching frequency of the converter, the AC and DC impedances of the transformer and diodes, as well as hard switching losses in the switching regulator when there is a mismatch between resonant and switching frequencies. As frequency increases in the circuit, the AC impedances of the circuit increase and thus relatively more energy circulates in the resonant tank and is not transferred to the output. Furthermore, the series and parallel resonant tanks result in greater circulating energy than the series parallel, making the series parallel more power efficient [118].

Soft Switching The overall efficiency of a switching regulator is closely linked to the switching scheme implemented. The behaviour of the resonant circuit following the switching regulator creates the conditions for what is called soft switching. Soft switching refers to a switching scheme which achieves zero voltage or zero current switching. This occurs when either the voltage or current (respectively) falls to zero before the following current or voltage (respectively) signal enters the regulator MOSFET. This is in contrast to hard switching, in which the trailing edge of the voltage (or current) signal overlaps with the leading edge of the current (or voltage) signal, leading to power dissipation in the MOSFET during switching. Hard switching losses can be reduced by increasing the switching speed, but this inevitably leads to significant electromagnetic interference (EMI) due to the large rate of change in the current signals. Soft switching is generally achieved by introducing a resonant element in the circuit which synchronizes with the switching frequency. As a result, the resonating signal falls to zero when the MOSFETs switch, and hard switching power losses are mitigated.

The preferred mode for soft switching in a resonant converter is zero-voltage switching, which occurs when the circuit is driven at a frequency above the resonant frequency of the converter [118]. More specifically, zero voltage switching occurs when the derivative of the gain curve with respect to switching frequency is negative.

Half Bridge LLC Converter Design The half bridge LLC converter is a popular resonant converter topology for applications which require high efficiency. A common methodology for half bridge design is shown in Figure 2.5, alongside the relevant design equations. Since the LLC resonant tank consists of three reactive elements, it corresponds to two resonant frequencies, $f_{r,1}$ and $f_{r,2}$ (Equations 2.32 and 2.34). Normally the higher frequency $f_{r,1}$ is referred to as the resonant frequency of the LLC circuit, as $f_{r,2}$ occurs when the two inductors appear as a single element. The separation of the two frequencies depends on the ratio of L_m to L_r (L_n).

By virtue of the resonant nature of the LLC converter, the circuit lends itself to Fourier harmonic analysis based around the fundamental driving frequency f_{sw}. The typically used approach is known as Fundamental Harmonic Approximation (FHA) [31, 33]. Using the FHA approach, the load R_e (Equation 2.36), quality factor Q (Equation 2.37), and gain M_g (Equation 2.38) of the LLC resonant circuit are derived. The load seen by the resonant tank, R_e, is directly related to the actual load of the converter and the turns ratio of the transformer, n. The output voltage is a function of frequency and is calculated as $V_{out} = \frac{1}{2} n M_g V_{in}$ where the total gain is defined as $G = \frac{1}{2} n M_g$ for a half bridge converter (Equation 2.39). The FHA approach is appropriate for a first design iteration, however it takes into account only the effects of the primary harmonics of the circuit. As a result, higher order effects, which may lead to changes in the gain curve and power conversion efficiency, are ignored. Therefore circuit simulation and hardware demonstration is necessary to identify shortcomings which are ignored in the simplifications.

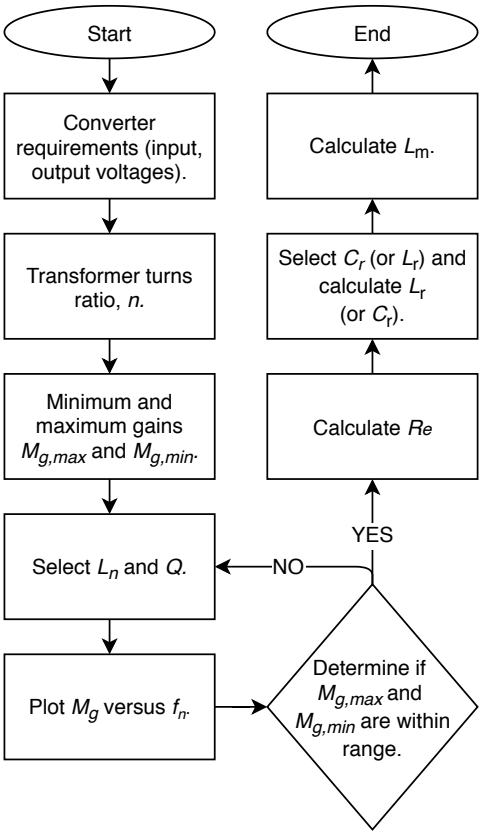

Figure 2.5: Typical design process flow for an LLC DC/DC converter.

$$n = \frac{2V_{out}}{V_{in}} \tag{2.31}$$

$$f_{r,1} = \frac{1}{2\pi\sqrt{L_r C_r}} \tag{2.32}$$

$$L_n = \frac{L_m}{L_r} \tag{2.33}$$

$$f_{r,2} = \frac{f_{r,1}}{\sqrt{1+L_n}} \tag{2.34}$$

$$f_n = \frac{f_{sw}}{f_r} \tag{2.35}$$

$$R_e = \frac{8n^2 R_L}{\pi^2} \tag{2.36}$$

$$Q = \sqrt{\frac{L_r}{C_r}} \frac{1}{R_e} \tag{2.37}$$

$$M_g = \frac{|L_n f_n^2|}{\sqrt{((L_n+1)f_n^2 - 1)^2 + (((f_n^2-1) f_n Q L_n)^2}} \tag{2.38}$$

$$G = \frac{1}{2} n M_g \tag{2.39}$$

The operating range of the converter should be defined in terms of the allowable variations of the input and output voltages. The ranges translate into maximum and minimum necessary resonant tank gains (Equations 2.40 and 2.41). The maximum and minimum gains are considered to be within range if they are intersected by the gain curve representing the chosen Q-factor. The range in gain translates to a defined operating frequency range.

$$M_{g,max} = \frac{V_{out,max}}{V_{in,min}} \tag{2.40}$$

$$M_{g,min} = \frac{V_{out,min}}{V_{in,max}} \tag{2.41}$$

2.4. Thermionic Cathode

The need for a cathode neutralizer for an ion propulsion system stems from the fact that expelling a charged ion plume for an extended period of time leads to a build-up of negative charge on the spacecraft. In turn, the negative charge would exert an electrostatic force on the positive ions, resulting in an overall elimination of the thrust generated by the system. Therefore a method of neutralization is necessary in order to minimize the negative charge build-up on the spacecraft. A common approach is to use an emitter technology to inject electrons into the exhaust plume from a cathode device onboard the spacecraft, effectively neutralizing the ion beam and the limiting negative charge build-up on the satellite simultaneously.

Cathode emitters are typically radio-frequency (RF) cathodes, hollow cathode, or thermionic cathodes [53]. Both the RF and hollow cathodes are plasma-based devices which require a gas feed in order to generate a beam of free electrons. With control of the gas feed system, the density of the cathode plasma can be increased and due to the quasi-neutral characteristic of the plasma, space charge limitations are negated and relatively high currents can be extracted from these devices. This feature makes the hollow and RF cathodes popular with high power EP systems [39]. On the other hand, for a thermionic cathode the source of electrons is the cathode material itself.

In an RF cathode, a changing magnetic field is generated via an electromagnet operated with a high frequency alternating current. The electrons in the plasma respond to the changes in magnetic field, while the larger ions, which are too heavy to respond at a high frequency, are removed with an ion collector. The circulating electrons collide with incoming neutral gas, sustaining the plasma and electron emission.

The hollow cathode concept uses a heated internal electron emitting surface inserted into the cathode to initiate ionization of the incoming neutral gas. Very fast moving electrons are known to oscillate between temporary regions of high potential in the plasma in a motion referred to as the pendulum effect, which is a primary factor in the generation of electrons [39]. Other factors include photoelectric emission stimulated by the glow of the plasma, and ion and electron impacts on the emitting insert. Ultimately the plasma flows through an exit orifice at which point some of the energy is used to heat the emitting cathode insert and sustain the generation of electrons and plasma.

On the other hand, a thermionic cathode is based on the simple principle of thermionic emission of electrons. Thermionic electron emission occurs when a material is heated to the increase the energy of free electrons, which become more likely to be ejected from the material as the temperature increases. The current density emitted from a thermionic cathode is limited by the temperature of of the material, and the space charge limitations related to the geometry of the cathode/anode setup. Furthermore, due to the high temperature operations of thermionic cathodes, a relatively high proportion of the input power can be wasted via thermal radiation.

Thermionic Emission Thermionic emission of an electron from a material is dependant on an increase in the energy of free electrons. Increasing the energy of free electrons overall is achieved via increasing the temperature of the material. The minimum energy required for an electron to fully escape a material is referred to as the work function. For a material with a temperature T and a work function ϕ, the thermionic current density emitted J is given by the Richardson-Dushman equation [39]:

$$J = AT^2 \exp\Big(-\frac{e\phi}{k_B T}\Big) \tag{2.42}$$

where A is the Richardson constant:

$$A = \frac{4\pi m_e k_B^2 e}{h} = 1.2 \times 10^6 \mathrm{Am}^{-2}\mathrm{K}^{-2} \tag{2.43}$$

where m_e and e are the mass and charge of the electron, h is the Planck constant, and k_B is the Boltzmann constant. The exponential dependence on ϕ and quadratic dependence on T ensure that thermionic current density emitted increases rapidly with an increase in temperature, or with a decrease in work function.

In general the work function of a material is a function of temperature as well. Typically the following revision of the Richardson-Dushman equation is used to correct the work function to first order [108]:

$$\phi = \phi_0 + \alpha T \tag{2.44}$$

$$\begin{aligned} J &= A\exp\big(-\frac{e\alpha}{k_B}\big)T^2\exp\big(-\frac{e\phi_0}{k_B T}\big) \\ &= DT^2\exp\big(-\frac{e\phi_0}{k_B T}\big) \end{aligned} \tag{2.45}$$

where D is the modified Richardson constant.

The work function for common thermionic emitters is typically on the order of a few electron-volts. A small list of these materials are shown in Table 2.3. Typical metals have relatively high work functions (4 eV or higher), so that high temperatures are required to achieve moderate emission current. Ultimately, thermal radiation at these high temperatures is excessive and high evaporation rates lead to shorter lifetimes making standard metals unsuitable for long-term use. For this reason refractory ceramics and metals are often chosen since they are more tolerant to high temperatures. Alternatively, more complex boride and oxide cathode materials can be created which have much lower work functions (2 eV or lower). However, these materials are much more susceptible to corruption since often a sensitive coating or chemical composition is the key to increased emission efficacy [53].

Table 2.3: Work functions of typical thermionic emitter materials [108].

Material	ϕ [eV]
Tungsten	4.87
LaB_6	2.69
CeB_6	2.50
Lithium	2.50
$C_{12}A_7$	2.40
BaO	1.55
BaO-W	2.10
Caesium	1.81

Child Langmuir Law The flow of electrons from the neutralizing cathode to the exhaust plume beam closes the electric circuit in an electrodynamic thruster concept. However for a space-based EP system, the transfer of electrons from cathode to anode occurs through a vacuum medium. The space charge in a vacuum medium is generally described by the Poisson equation:

$$\nabla^2 V = \frac{\rho}{\epsilon_0} \tag{2.46}$$

which relates electric potential field V to space charge ρ, where ϵ_0 is the permittivity of free space. The Child Langmuir law is a special case solution to the Poisson equation which gives the upper limit on the space charge current density in a diode [17, 57]. In the context of the μACFT, the diode consists of the anode and cathode, where the cathode is generating electrons. A negative space charge can build-up around the electron emitter resulting in a repulsion of newly emitted electrons. Ultimately there is a saturation effect which occurs when the generation of new electrons is occurring at a rate faster than the rate of electrons being taken by the gradient in the potential field or recombining in the ion plume. In the case that the cathode and anode of the diode are infinite planes separated on a axis perpendicular to the planes by a distance d, the current density limit J is given by:

$$J = \frac{4\varepsilon_0}{9}\sqrt{\frac{2m_e}{e}}\frac{V_a^{3/2}}{d^2} \tag{2.47}$$

where A is the area of the cross-sectional area across which the electrons are distributed, V_a is the potential difference between the cathode and anode, and ε_0 is the permittivity of free space. In the case that the cathode and anode are infinitely long cylinders with radii r_c and r_a respectively (with $r_c < r_a$) the current density limit is [15]:

$$J = \frac{4\varepsilon_0}{9}\sqrt{\frac{2m_e}{e}}\Big(\frac{V_a}{r_c\ln(r_a/r_c)}\Big)^{3/2}\frac{1}{d^2} \tag{2.48}$$

3

Iodine-Fed μACFT Engineering Model

In this chapter, the design and testing of the iodine μACFT is outlined in detail. To begin, the system requirements of the device are synthesized based on the intended CubeSat application, as well as the known characteristics of the μACFT architecture and iodine thrusters. Following is a description of the overall system design along with relevant details regarding individual subsystem designs. The test results from performance characterization of the engineering model using both xenon and iodine propellant are presented. Lastly, the iodine μACFT EM performance is compared to previous μACFT devices, as well as other CubeSat thrusters, and other iodine thrusters.

3.1. μACFT System Requirements

The CubeSat design standard prescribes a number of constraints and requirements on the design and construction of a CubeSat. Although these constraints are not utterly strict, they offer a stable framework and useful guidelines for nanosatellite design that are subscribed to by many developers. Some of these constraints apply directly and indirectly to the design and integration of propulsion systems. The requirements of the μACFT arise from constraints on the system design imposed by the CubeSat platform, the launcher, mission concepts, and the selection of iodine propellant. A summary of all the system requirements is found in Section 3.1.5

3.1.1. Platform Constraints

The CubeSat design standard introduces a few constraints specifically for propulsion systems, and a few which are peripherally relevant for propulsion systems. Firstly, no pyrotechnics are permitted on the CubeSat platform (Requirement 3.1.3 [67]) and total stored chemical energy shall not exceed 100 Whr (Requirement 3.1.6 [67]). Furthermore, the use of hazardous materials in the CubeSat design should be compliant with the USA Air Force Space Command Range Safety User Requirements (AFSPCMAN 91-710 Volume 3 [20], Requirement 3.1.7 [67]). The combination of constraints strongly discourage the use of chemical propulsion systems and corrosive or otherwise dangerous propellant options. Requirements 3.1.4 and 3.1.5 [67] relate directly to propulsion systems. They state that any propulsion systems shall be designed, integrated and tested in accordance with the AFSPCMAN 91-710 V3. These requirements on the propulsion system are summarized as:

PRO-001: The thruster shall not incorporate pyrotechnics.

PRO-002: The thruster shall comply with the AFSPCMAN 91-710 hazardous materials allowances.

PRO-003: The thruster shall comply with the AFSPCMAN 91-710 inhibit requirements.

PRO-004: Stored chemical energy in the thruster shall not exceed 100 Whr.

Some efforts have been made in establishing safety standards with respect to CubeSat propulsion systems [16]. In terms of range safety, current standards and constraints are drawn from AFI 91-217, AFSPCMAN 91-710, and the user manuals of the specific launcher.

There are other key constraints related to launcher and range safety. The most relevant of these are the constraints on pressurized systems which are typical elements of propulsion systems. Although safety verification techniques have been proposed [16], in many cases pressurized vessels are simply not allowed for CubeSats. This is because CubeSats are typically launched as secondary payloads, which are subject to stricter constraints in order to ensure the safe and successful delivery of the primary payload [75]. The key requirement derived from the launcher and range safety guidelines is:

PRO-005: The thruster shall not incorporate pressurized vessels.

CubeSats are built up of individual units (U) of size 10.0 x 10.0 x 10.0 cm. Units are combined end-to-end via 0.85 x 0.85 cm rails which run along the edges of the cube or stack of cubes. The California Polytechnic State University CubeSat standard defines the acceptable dimensions for CubeSats of size 1U, 1.5U, 2U, 3U and 3U+. The 3U+ design is characterized by a tuna can cylindrical extension mounted on one of the end faces of the 3U construction with a diameter of 6.40 cm and a height of 3.60 cm [67]. These dimensions are summarized in Figure 3.1.

In recent years, developers have popularized larger CubeSats configurations, such as the 6U, 12U, or 24U because of the improved functionality that the size provides. Typically these larger configurations are built up from the 3U CubeSat as a base unit. In response Cal Poly has released a design specification for the 6U CubeSat design [72] which also accounts for the tuna can extension on each of the 3U sub-structures of the design.

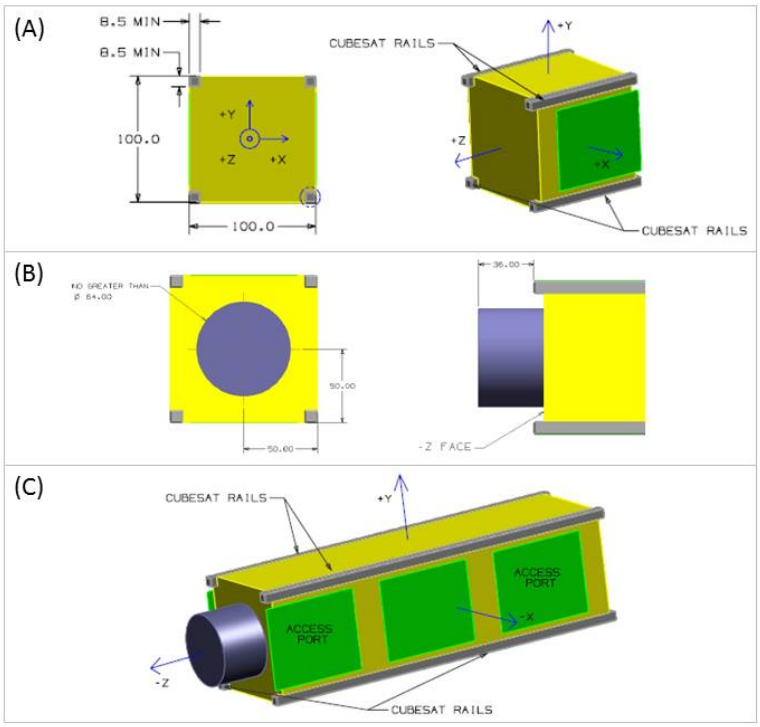

Figure 3.1: Dimensions of 3U+ CubeSat, the intended platform of the μACFT. In (A) is the dimensions of a single U, in (B) the dimensions of the 3U+ tuna can extension, and in (C) the dimensions of a full 3U+ CubeSat.

Currently, integration of ion propulsion system into a complete and functional 1U or 2U CubeSat system has not been successful. The key limitations are the the volume and power constraints. Firstly, a typical EP system can take up to 1U of volume and up to 1 kg of mass on its own [58], leaving little to no space for mission critical subsystems such as the on-board computer, power or communications systems. Furthermore, due to the smaller surface area of the 1U and 2U CubeSats, the electrical power generated by body mounted or deployable solar panels is typically not enough to provide power to an EP system and the other key subsystems such as the on-board computer and attitude control which would likely be active simultaneously.

On the other hand, the 3U platform has been show to host a variety of propulsion system with it's larger volume and power availability, making it the smallest CubeSat platform that is practically capable of using a propulsion system [85]. Since, the 3U and 3U+ platforms currently serve as the building blocks for larger CubeSat systems, the design objective for the μACFT is to achieve an envelope which can be integrated into a 3U+ platform. As a result, the thruster would be available for the smaller 3U and 3U+ CubeSat platforms, as well as larger systems. The requirement defining the thruster dimensions is:

MEC-001: The thruster shall fit within a 3U+ CubeSat platform.

The mass of the fundamental CubeSat unit is limited to 1.33 kg according to the CubeSat design standard. This scales to 2.00 kg for the 1.5U, 2.66 kg for the 2U and 4.00 kg for the 3U (Requirements 3.2.10-3.2.13 [67]). However, larger masses may be considered on a mission-to-mission basis. For this purpose, there is a waiver which must be submitted indicating non-compliance to the standard mass restriction.

An estimate of total propulsion system mass depends on the actual mission requirements. Fundamentally the mission requirements on Δv lead to a total propellant mass requirement (Equation 2.14), which in turn influences the overall mass. Giving a generous margin to mass of the thruster and CubeSat simultaneously, the requirement on the total thruster system mass is:

MEC-002: The thruster wet mass shall not exceed 1.00 kg, or 25% of the total 3U+ CubeSat mass.

Standardization of the printed circuit boards (PCB) used in the CubeSat designs is also covered in the design standard. Although the PC/104 standard predates the CubeSat design standard, it has been adopted as the de-facto standard for PCB subsystems in CubeSat designs [21]. The PC/104 standard is characterized by a form factor of 9.0 x 9.6 cm and 104 signal contacts on two bus connectors (P1 and P2), which can be connected via stacking without no further wiring. The PC/104 stack modules typically operate on ±12(±5%) V (P1 signal bus) or ±5(±5%) V (P1 or P2 signal bus) voltage rails.

PWR-001: The power processing unit shall operate on a 12 V regulated, or unregulated, input voltage.

PCB components which integrate with PC/104 systems are either PC/104 compliant, meaning they comply to all indicated mechanical and electrical specifications, or bus-compatible, meaning that the device provides either a male or female PC/104 bus connector but perhaps doesn't match the prescribed form-factor.

In terms of microcontroller communication between subsystems, there are no specified standards. However the most popular protocols used in CubeSats include I^2C (Inter-Integrated Circuit), SPI (Serial Peripheral Interface), RS-232, and CAN (Controller Area Network) bus standards. Of the most popular implementations (I^2C, RS-232 and SPI, in that order), I^2C was shown by Bouwmeester et al. to be the least reliable [9]. However, many COTS components and subsystems which are popular in CubeSat designs include integrated I^2C controllers. The thruster requirement which relates to the CubeSat design standard for electronics is:

PWR-002: The power processing unit shall be compliant with the PC/104 standard.

Much effort has been made towards accurately estimating the power levels available onboard CubeSat platforms in order to assess the feasibility of scientific or exploratory CubeSat missions which have high power requirements [23, 73]. It is estimated that power generation onboard a 3U CubeSat with deployable solar panels can reach 20 - 30 W [51, 92]. However, instantaneous power produced by solar panels in best case scenarios does not translate directly into consumable power. More conservative estimates of onboard available power are in the range of 2 - 10 W [22, 85, 91] depending on the configuration of the solar arrays (body-mounted vs. deployable) and orbit of the satellite. CANX-2, a 3U CubeSat with body-mounted solar panels and an experimental thruster system launched into Earth orbit in 2008, reportedly generated approximately 5 W of power on average, and consumed between 1 - 6 W in nominal and transmission modes respectively [84].

Due to the relatively low thrust provided by electric propulsion systems, significant changes in momentum are achieved over long periods of active operations. Therefore the power processing unit will be required to supply energy to the thruster over extended periods of time. However the limitations of the power available on the platform, which varies with the the orbital position and attitude of the spacecraft, will constrain the ability to sustain operations. Based on the published case studies of successful 3U CubeSats and the prospects for an increase of power with deployable solar panels, it is reasonable to assume that the thruster, typically consuming power in the range of 10 W, only operates while the CubeSat is actively generating power.

The most conservative case with respect to power generation is to assume a low earth equatorial orbit, where the satellite spend approximately half the time in eclipse. For this case the duty cycle of the thruster might be 50%. In practice, for a low Earth orbit CubeSat, this translates to approximately forty-five minutes of continuous operations. In a polar orbit, the CubeSat may be illuminated more frequently, or even permanently, and the duty cycle would be required to increase. Based on the estimated instantaneous power available as well as the duty cycle permitted by the illumination of the CubeSat, the following requirements are formulated:

PWR-003: The power processing unit shall provide up to 10 W of output power.

PWR-004: The power processing unit duty cycle shall be 50%, or greater.

Finally, as an electrodynamic ion thruster, the μACFT requires a high accelerating potential on the anode in order to help ionize propellant and accelerate the ions through the chamber. Based on previous tests conducted with miniature ACFT LM and EM, an anode potential in the range of 1000 - 15000 V has typically led to reliable ignition and operations of the thruster [41, 91]. However, operating a different anode potentials can lead to different performance with respect to divergence efficiency, for example. Therefore the requirement on the output potential of the power processing unit is:

PWR-005: The power processing unit shall provide up to 1.5 kV controllable output voltage.

As a general guideline, the CubeSat standard advises limiting the external magnetic field of the spacecraft, measurable outside the structure, to 0.5 Gauss above the Earth's magnetic field at most (Requirement 3.1.10 [67]). This constraint limits the chances of the CubeSat's magnetic field interfering with the deployment mechanism. Furthermore, electromagnetic interference (EMI) requirements are sometimes enforced by launch providers, and EMI risk must be taken into consideration in the system design of the spacecraft. Therefore the requirement on the system regarding magnetic influence is:

EMI-001: The thruster magnetic field shall not exceed 0.5 G greater than Earth's.

EMI-002: The thruster shall comply with the EMI requirements of the chosen launcher.

3.1.2. Launcher Constraints

The Cal Poly CubeSat standard also offers no specific structural requirements related to CubeSat design. Instead the structural requirements of the satellite are to be specified by the launch provider. Summarized in Table 3.1 are the structural requirements of possible CubeSat launchers [91]. The structural requirements of the CubeSat do not directly translate into the structural requirements of the individual components. However, they provide a relevant standard for comparison to the vibration frequencies and loads which can be sustained by subsystem structures. The generalized requirement which addresses structural requirements imposed by launchers is:

MEC-003: The thruster shall withstand vibrational and static loads of the chosen launcher.

Table 3.1: Summary of structural requirements for potential CubeSat launch providers [2–5, 48, 93, 95, 96]. MFEF: minimum fundamental eigenfrequency. QSL: quasi-static load.

Launcher	**Lateral MFEF** [Hz]	**Longitudinal MFEF** [Hz]	**Lateral QSL** [g]	**Longitudinal QSL** [g]
Ariane 5	10	31	±0.25	-4.55
Vega	15	60	±0.90	-7.00
Soyuz	15	35	±1.80	-5.00
Delta IV	8	30	±2.00	-6.50
Atlas V	8	15	±2.00	-6.00
Falcon 9	10	25	±3.00	-8.50
H-IIA	10	25	±1.80	-4.00
PSLV	45	90	±6.00	-7.00

3.1.3. Mission Concepts

Aside from the constraints imposed on the μACFT device with respect to the desired application on a CubeSat platform, there are also performance benchmarks which must be met in order for the system to be practically useful. Investigating proposed missions can provide guidelines for performance objectives for a 3U+ CubeSat EP system. The key performance parameter which is typically associated with a mission concept is the change in spacecraft velocity Δv which is necessary in order to perform a desired orbital maneuver. The Δv capacity of a given propulsion system is fundamentally related to the thrust and specific impulse of the thruster (Equation 2.14), and thus the metric forms a link between thruster performance and orbital maneuverability.

Near-term mission concepts which require CubeSat propulsion systems typically involve change in orbit, station-keeping, and formation flying in low Earth orbit. The objectives of these mission concepts are to improve scientific yield and general functionality of nanosatellite swarms by more precisely controlling the location and orientation of the satellites in orbit. In the context of these missions, there are both absolute orbital maneuvers and relative orbital maneuvers which must be considered.

Change Orbit Due to the fact that CubeSats are typically launched as a secondary payload, they are not often injected into an orbit which is ideal for the intended mission, but rather an orbit nearby that of the primary payload. Alteration of the satellite orbital elements can be achieved via a wide variety of impulsive or non-impulsive maneuvers. A summary of the Δv costs required in order to alter the orbital elements of the satellite with low thrust maneuvers is given in Table 3.2.

Table 3.2: Summary of Δv cost for correction of orbital elements with low thrust maneuvers [82]. Gravitational parameter μ is for Earth.

Orbital Element	Δv **Cost**
Semi-Major Axis, a	$\left\lvert\sqrt{\frac{\mu}{a_i}}-\sqrt{\frac{\mu}{a_f}}\right\rvert$
Argument of Perigee, ω	$\sqrt{\frac{\mu}{a}}\frac{2e}{3\sqrt{1-e^2}}\lvert\Delta\omega\rvert$
Inclination, i	$v\sqrt{2-2\cos(\frac{\pi}{2}\Delta i)}$
Eccentricity, e	$\sqrt{\frac{\mu}{a}}\frac{2}{3}\left\lvert\sin^{-1}e_i-\sin^{-1}e_f\right\rvert$
RAAN, Ω	$\sqrt{\frac{\mu}{a}}\frac{\pi}{2}\lvert\Delta\Omega\rvert\sin i$

Evaluating the above equations to determine the Δv required in order to re-position a spacecraft (a functional change in orbital elements) in Earth orbit with an altitude of approximately 400 - 500 km is on the order of magnitude of 100 - 10000 m/s [54]. For example, in order to de-orbit a 400 km altitude satellite (by bringing it into the atmosphere at 100 km altitude), a total of 176 m/s is necessary. Alternatively, to transform a circular 400 km equatorial orbit into a polar orbit, 14482 m/s is required. However for very minor changes in the the orbital elements (station keeping activities), the Δv requirement is smaller. Generally, station keeping is based on negation of drift in orbital elements which is due to higher order gravitational perturbations, as well as other perturbations resulting from solar wind, atmospheric drag, or magnetic torque. The change in orbital elements due to perturbations can be described by the Lagrange Planetary Equations. The many cases, the perturbations are relatively small and the Δv cost of orbital maintenance is not large (typically on the order of 10 m/s) [25, 37].

Formation Flying The orbital maneuvers necessary for formation flying concern maintenance of the relative orbit between satellites. The injection into the formation flying orbit can be described by the previous section, maintenance of the orbit can again be analyzed using Lagrange Planetary Equations, and formation flying maneuvers with the equations in Table 3.2. To address the requirements of a nanosatellite formation flying mission, Gill calculated in a 2013 study that a pair of 3U CubeSats could maintain a formation (fixed separation along track) over 60 days against atmospheric drag at a 300 km altitude with a Δv of 12.4 m/s [38]. The AAReST mission proposes to perform a proof of concept of in-space assembly of small spacecraft subunits. The mission is to be performed with CubeSat platform-based spacecraft (two 3U CubeSats docking on a larger 15U core) with propulsion systems requiring a total Δv of 10 m/s [107].

Lunar and Interplanetary Transit A popular, albeit futuristic mission concept for CubeSats is exploration of nearby planetary bodies. The ultimate goal is autonomous CubeSats which perform orbital transfers and solo exploration missions. For EP systems which provide little acceleration, constant thrust must be applied over long periods of time to achieve an orbital transfer. The Δv required for a spiralling low thrust orbital transfer between planets is:

$$\Delta v = \sqrt{\frac{\mu_s}{a_i}} - \sqrt{\frac{\mu_s}{a_f}} \tag{3.1}$$

where a_i and a_f are the semi-major axis of the initial and final orbits, and μ_s is the gravitational parameter of the Sun. The Δv for interplanetary transfer within the solar system starting from Earth is in the range of 6 - 23 km/s. A spiral transfer from low Earth orbit (400 km altitude) to the Moon would require about 6.7 km/s. Conversano has studied the space exploration capabilities of a 3U CubeSat with EP for this mission. In a 2011 study, it was shown that a CubeSat could perform the maneuver with a Δv capacity of 6.9 km/s [22]. Then in a 2013 parametric study of a miniature xenon propulsion payload with a volume up to 1.4U and a mass up to 6 kg, the Δv capabilities of the thruster design space was estimated to be in the range of 1.0 - 7.0 km/s [23]. Based on the assumed performance metrics of the thruster, such as 40 W power consumption and 3000 s specific impulse, the mission concepts are not likely achievable on a 3U platform in the short term. One mission design in progress, the LunarCube, incorporates the Busek BIT-3 iodine-fed RF thruster on a 6U platform in order to inject into a lunar orbit from a lunar transfer trajectory, with a maximum Δv capacity of 3.2 km/s [104]. Regardless of realistic capabilities, lunar and interplanetary CubeSat missions are popular. NASA has proposed multiple other missions using CubeSats as companion spacecraft on larger missions to the Moon and Mars [51, 90].

In summary, there are a variety of different CubeSat mission concepts for which propulsion system performance is a key requirement such as orbital injection, formation flying, or interplanetary travel. The Δv requirement for these missions vary by multiple orders of magnitude (10 - 10000 m/s). Therefore the minimum viable performance requirement for a CubeSat thruster system is a Δv capacity on the order of 10 m/s, however the mission concepts for which this thruster could be used are limited to formation flying or station keeping. Ideally a thruster would offer more flexibility and thus be applicable in more scenarios. However this metric can serve as a minimum allowable performance requirement. In principle, the Δv capability can improved by increasing the propellant capacity of the thruster in order to accommodate more mission scenarios as desired.

PRO-006: The thruster shall provide at least 10 m/s of Δv capability for a 3U+ CubeSat platform.

3.1.4. Feed System Constraints

The decision to use iodine as propellant has implications on the design of the thruster, and in particular the feed system. Ultimately, it is the properties of iodine that must be taken into account in the design. First, iodine is a reactive substance which readily forms compounds with many other materials. As a result, iodine can cause irreversible discoloring and corrosive damage to materials such as aluminium, copper or some plastics. Therefore the following requirement is drafted:

FL-001: The feed system shall incorporate materials which are resistant to iodine vapor corrosion.

Since the propellant is stored in a solid form, it must first be vaporized before it can be used in the thruster. This is simply achieved by heating the propellant reservoir. However, in order to avoid redeposition of the propellant in the feed system causing a clog, the feedlines must also be heated. As a measure of caution, the feedlines should be at a higher temperature than the reservoir to ensure the chance of clogging via redeposition is a low. Operating the feed system at high temperatures has implications on the performance of the entire system, as other components in the μACFT and the CubeSat are sensitive to excess thermal energy. To account for the thermally actuated nature of the feed system, the following requirements are needed:

FL-002: The reservoir shall reach a temperature high enough to sublimate Iodine.

FL-003: The feedline temperature shall exceed the reservoir temperature.

FL-004: All components shall remain within their operational temperature range.

3.1.5. System Requirements Summary

In this section, the synthesis of the main system requirements for the iodine μACFT EM is layed out. A complete list of the requirements can be found in Table 3.3. Many of the requirements are derived from the CubeSat standard and other related launcher and launch range safety manuals. Other requirements are derived from publications, surveys, and case studies related to CubeSat technologies and mission concepts. Requirements for the iodine feed system are based on publications outlining development of other iodine thrusters. This requirement set influences the system design as well as testing activities during the thruster development.

Table 3.3: List of system requirements for iodine μACFT CubeSat EM.

ID	Requirement
PRO-001	The thruster shall not incorporate pyrotechnics.
PRO-002	The thruster shall comply with the AFSPCMAN 91-710 hazardous materials allowances.
PRO-003	The thruster shall comply with AFSPCMAN 91-710 inhibit requirements.
PRO-004	Stored chemical energy in the thruster shall not exceed 100 Whr.
PRO-005	The thruster shall not incorporate pressurized vessels.
PRO-006	The thruster shall provide at least 10 m/s of $\Delta\nu$ capability for a 3U+ CubeSat platform.
MEC-001	The thruster shall fit within a 3U+ CubeSat platform.
MEC-002	The thruster wet mass shall not exceed 1.00 kg, or 25% of the total 3U+ CubeSat mass.
MEC-003	The thruster shall withstand vibrational and static loads of the chosen launcher.
FL-001	The feed system shall incorporate materials which are resistant to Iodine vapor corrosion.
FL-002	The reservoir shall reach a temperature high enough to sublimate iodine.
FL-003	The feedline temperature shall exceed the reservoir temperature.
FL-004	All components shall remain within their operational temperature range.
PWR-001	The power processing unit shall operate on a 12 V regulated, or unregulated, input voltage.
PWR-002	The power processing unit shall be compliant with the PC/104 standard.
PWR-003	The power processing unit shall provide up to 10 W of power.
PWR-004	The power processing unit duty cycle shall be 50%, or greater.
PWR-005	The power processing unit shall provide up to 1.5 kV controllable output voltage.
EMI-001	The thruster magnetic field shall not exceed 0.5 G greater than Earth's
EMI-002	The thruster shall comply with the EMI requirements of the chosen launcher.

3.2. Thruster Design and Assembly

The final design of the iodine µACFT can be seen in Figure 3.2, where all the main elements of the system are visible except for the DC/DC converter. On the left hand side, a cross section of the dual chamber feed system with thermally actuated valve can be seen. In the center of the feed system is the magnetic discharge chamber and high voltage anode, encased in a column of insulating ceramic. Propellant is vapourized in the large propellant reservoir, is transfered to the secondary chamber through the orifice which is sealed by the thermal actuator. From the secondary chamber, the vapour flows directly into the anode and then the magnetic chamber. On the right hand side of the ceramic insulation, there is a feed through in the face of the thruster where the thermionic cathode neutralizer is visible. A PTFE cap is used to cover the rear end, shielding the main body of the CubeSat from the thruster. Furthermore, the inner surface of the cap is covered in a reflective coating in order to reflect thermal radiation back to the feed system. A single feed through is offered by the cap for electric connections. The total dry mass of this assembly is 280 grams, and the total volume of the cylinder containing the thruster is 180 cm^3.

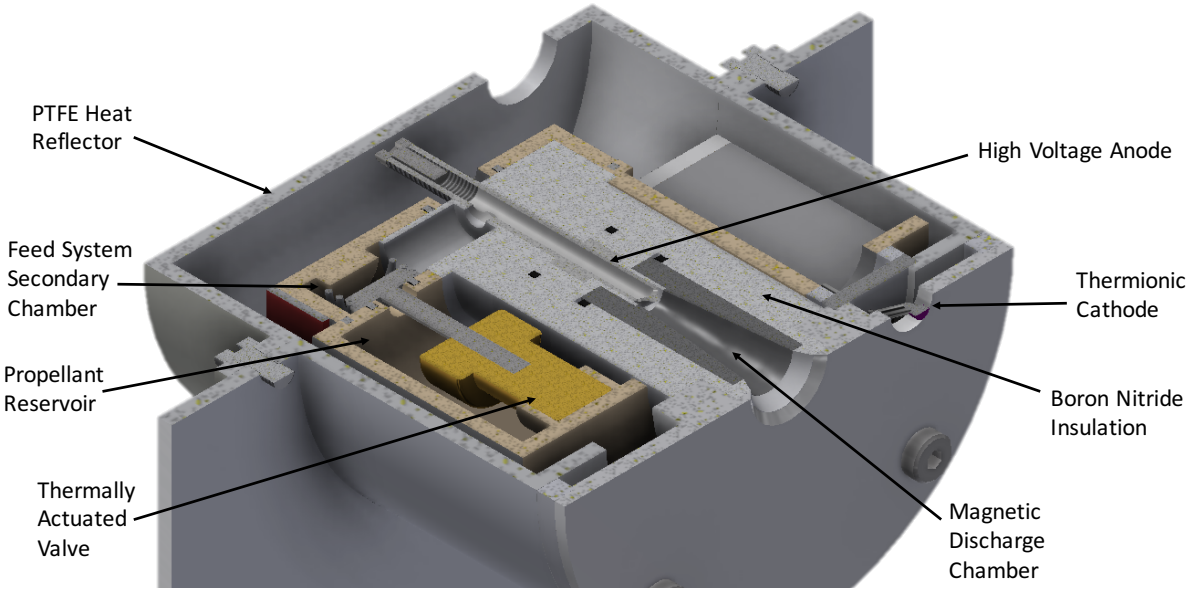

Figure 3.2: Half-section view of µACFT CAD model. Through the center is the magnetic thrust chamber and high voltage anode, encapsulated in ceramic insulation. The anode is fed iodine directly via the dual-chamber feed system which wraps around the insulation. The propellant reservoir and secondary chamber are separated by a thermally actuated valve. A section of the reservoir is cut out (right) for the cathode neutralizer and an electronic feedthrough. PTFE spacers and standoffs are insulate the feed system from panel which interfaces with the CubeSat structure.

3.2.1. Housing

The µACFT system is nearly completely housed inside of the so-called tuna can extension for the 3U+ CubeSat platform (Figure 3.1). The cylindrical housing measures 64 mm in diameter and 56 mm in height, with only a 20 mm extrusion into the main body of the satellite from the end face of the CubeSat. The housing (Figure 3.3) is constructed of aluminum, and includes an integrated end face for a CubeSat structure. The housing consists of three parts: the end face of the thruster, the end face of the CubeSat combined with the body of the tuna can extension, and the heat reflector cap. The entire feed system and thruster magnetic chamber assembly are mounted to the end face of the thruster. In practice, an additional volume margin would be necessary in the CubeSat system design to account for the dedicated DC/DC converter. In total, the entire thruster, with electronics, could be housed in the tuna can extension, and one third of the adjacent 1U.

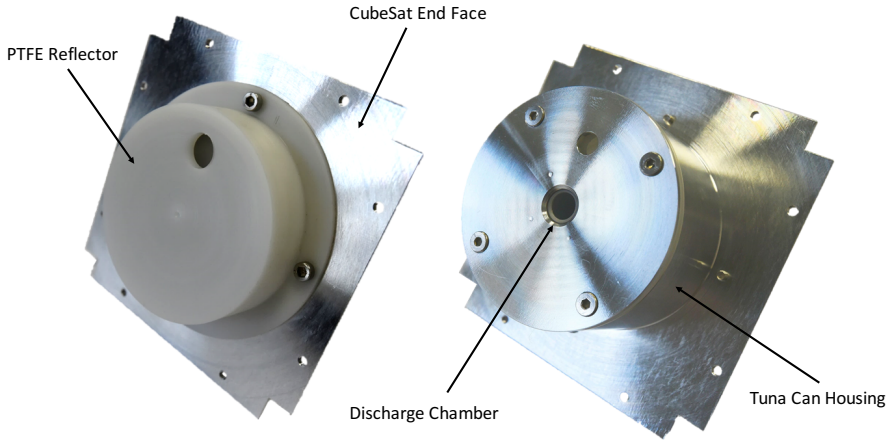

Figure 3.3: µACFT EM and magnetic chamber housing prior to feed system integration. The tuna can housing is aluminium and the cap is PTFE.

3.2.2. Feed System Design

A key aspect of the iodine-fed µACFT system is the feed system concept since the propellant is stored as a solid. As a result the concept of the feed system differs from that of a typical xenon gas-fed thruster. A few key characteristics of the iodine feed system are:

- Depressurized reservoir tank.
- Thermal control of vapour generation.
- Heated feed system to prevent redeposition and clogging.
- Material compatibility with corrosive iodine vapour.

A combination of the experimental results of NASA/Busek and Airbus Friedrichshafen with chemical resistance charts from material suppliers was consulted to generate a list of resistant material options which can be used in feed system construction, shown in Table 2.2.

Table 3.4: Materials (metals, plastics and elastomers) with moderate to excellent resistance to Iodine corrosion. [1] 20°C, [2] 60°C [26, 47].

No Effect		**Minor Effect**	**Moderate Effect**
Epoxy	Styrene butadiene (SBR)[1]	Ethylene propylene	Polyacetal
Viton	Polyvinylidene fluoride (PVDF)[1 2]	Buna N (NBR)	
Ceramic	Polypropylene (PP)[1]	Tygon (E-3606)	
Noryl	Titanium	Hastelloy C	
Teflon (PTFE)	Polyether ether ketone (PEEK)		

In designing the feed system for the µACFT system, the new space design philosophy was kept in mind. Firstly, it was decided that a mass flow controller would not be used in the feed system as it would increase complexity and impede the effort to miniaturize and simplify the thruster. Instead, the propellant feed system would be designed such that the propellant flow rate could be predicted as a function of the feed system dimensions and temperature. Thus in practice the mass flow rate in the thruster is controlled via the power supplied to the electric heaters used to vaporize the solid propellant. In order to limit the mass flow rate into the thrust chamber, an orifice is required. The area of the orifice, A_o is calculated based on Equation 2.29, where P_1 is the pressure in the main reservoir, P_2 is pressure in the secondary chamber, $\dot{m}$ is the desired mass flow rate and C_v is the dimensionless orifice flow coefficient.

$$A_o = \frac{\dot{m}}{C_v}\sqrt{\frac{k_B T}{2MP_1(P_1 - P_2)}} \tag{3.2}$$

The pressure P_2 is given by the equation:

$$P_2 = \sqrt{\frac{128\mu RT\dot{m}}{\pi d^4 M}} \tag{3.3}$$

where d is the inner diameter of the anode. In Equation 3.2, it is assumed that the density of the vapour is defined by the pressure inside the propellant reservoir, P_1. Equation 3.3 is derived from the equation for laminar flow through a pipe (Equation 2.26), where at one end the pressure is P_2 and at the other end of the pipe the pressure is the vacuum pressure P_{vac}, where $P_{vac} \ll P_2$ and is assumed to be negligible. The density of the vapour inside the pipe is assumed to be defined by the secondary chamber pressure P_2.

In order to further reduce complexity and improve overall system synergy, a traditional electric valve is eliminated in favour of a thermally actuated valve [42]. A thermal working element with kick-up temperature of 60°C is used. The actuator arm was replaced with a custom-made titanium valve head which seals the propellant reservoir. Viton o-rings are used to create seals between individual components of the feed system where possible in order to prevent propellant leaks.

Ultimately, polyether ether ketone (PEEK) was chosen for the feed system material, as it's resistance to corrosion, tolerance of high temperatures, high stiffness and low density are ideal characteristics. The glass temperature of PEEK is 143 °C [112], and thus this is the upper limit on the operating temperature of the feed system.

The feed system design concept can be seen in Figure 3.4. A dual chamber design with no piping was chosen to feed the iodine into the anode directly. The propellant reservoir opens into the secondary chamber when the thermally-actuated paraffin valve is opened. A 0.03 mm^2 orifice restricts mass flow between the two chambers. Electric heaters are wrapped around the inner wall of the reservoir and the outer wall of the secondary chamber. PT100 thermistor temperature sensors accompany the heaters in order monitor the temperature of the feed system. Raising the temperature of the device is necessary to activate propellant flow through the thruster, and by monitoring the temperature, the mass flow rate through the thruster can be estimated.

The secondary chamber is filled with an alumina crystal, which has a porous sponge-like structure, in order to insulate the feed system from the high voltage of the anode and to help increase the pressure in the feed system to prevent a plasma discharge.

The feed system reservoir which was constructed for this project (Figure 3.4) can hold up to 200 g of solid iodine. However if additional fuel were necessary to satisfy mission requirements, the reservoir of the feed system can be made taller. As a result, other components would need to be extended as well, such as the valve pin, anode, insulating ceramics, and the PTFE cap. Doing so increases the extent to which the thruster intrudes in the main body of the CubeSat. Regardless, the feed system concept remains the same in principle. Increasing the height of the reservoir allows for a 7 g/mm increase in capacity.

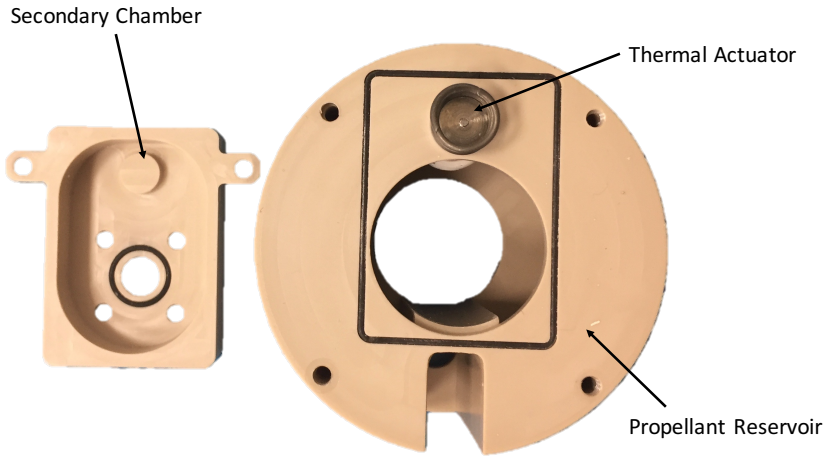

Figure 3.4: µACFT feed system for iodine. The reservoir and secondary chamber are made with PEEK.

3.2.3. Thermal Design

Since the generation of propellant vapour is thermally actuated, the iodine μACFT must operate at a relatively high temperature. Due to the intended CubeSat application, efficient use of heat is critical since the power available for heating and the tolerance to excessive thermal loads are both low. The thermal design concept of the μACFT EM accounts for this by insulating the feed system from the housing as much as possible, and minimizing the temperature of the housing which interfaces with the CubeSat. The objective of the thermal design is to contain as much heat as possible in the feed system, and to radiate away heat which reaches the housing. This is achieved by placing low thermal conductivity PTFE standoffs between the feed system and the housing. The outside of the feed system is covered with a low emissivity coating, so that the heat emitted by the outer surface is lower than that of the inner surface. Furthermore, the feed system is fully enclosed so it does not view the rest of the CubeSat. The inner surface of the housing which views the feed system is covered in a reflective silver lining to increase the proportion of heat radiated from the feed system which is reflected back. Lastly, the outside of the housing is covered in a white coating to increase it's emissivity and reduce the thermal load on the CubeSat structure.

The main source of heat in the thruster is the electric heaters on the secondary chamber and reservoir. However the anode is typically the hottest component in the system [91], thus heat is generated in the center of the feed system as well.

Thermal Network Model In order to evaluate thermal design choices as well as estimate the total amount of heat required to maintain the operating temperature of the feed system, the author has implemented a simple steady state thermal network model in Multisim. Since electric heater power is necessary for initiating propellant flow, the thermal design of the thruster impacts the overall power consumption of the system. In order to ensure the heater power is low, the model is used to rapidly assess changes to the thermal design of the thruster such as locations of the heaters, using different materials or surface finishes, or changing the dimensions of an insulator or standoff.

The thermal network model is based on the basic equations of heat transfer, namely conductive (Equation 3.4) and radiative (Equation 3.5) heat transfer.

$$Q_c = k\Delta T = \frac{k_s A}{L}\Delta T \tag{3.4}$$

$$Q_r = 4\epsilon\sigma F_{12} A T^4 \tag{3.5}$$

Q_c in Equation 3.4 is the heat transferred from one surface to another via a thermally conductive interface with an area A, depth L, and specific thermal conductivity k_s when a temperature differential of ΔT exists. In the case of thermal radiation, the heat exchange is driven by the Stefan-Boltzmann law. Q_r is the amount of heat radiated by a surface with area A which is incident on another surface. The received heat is related to the geometry relating the two surfaces in space, which is encapsulated in the view factor F_{12}.

The thermal network model implemented is based on a simple analogy between the heat transfer equations and Ohm's law. Considering $Q_c = k\Delta T$ and $\Delta V = IR$, one can see that ΔV is equivalent to ΔT, I is equivalent to Q_c and k is the inverse of R. Thus a network of thermally conducting interfaces could be treated like an electrical circuit with the correct substitutions. However radiative heat exchange must also be taken into account. Simplifications must be made regarding the radiative heat transfer between components since it is a non-linear effect (unlike conduction of electricity and heat). Firstly, Q_r is linearized around a constant bias temperature T_{lin}, such that for a small range around that temperature, the linearized result is approximately equal to the true value.

$$Q_{r,lin} = 4\epsilon\sigma F_{12} A T_{lin}^3 T \tag{3.6}$$

A target temperature of 100° C is used in the analysis, based on the operating temperatures reported by developers of other iodine thrusters, namely NASA/Busek and University Giessen [45, 77]. This temperature is also used for linearization of the radiated heat. The more the temperature of nodes in the model deviate from T_r, the less accurate the simulated radiative heat transfer becomes.

A key simplification in the model is neglecting the thrust balance arm on which the thruster is mounted, which could conduct considerable heat. Furthermore, the view factors were not treated in full detail due to the complex geometry of the device. Instead, view factors are considered to be zero or one for situations where components are fully separated or directly viewing each other. View factors of one-half or one-third were used in situations where the component views two or three others more or less equally.

Due to the simplifications used in the thermal network model, the numeric results of the simulations are not highly accurate. Instead the results are used only to estimate the heat power required to sustain a high operating temperature in testing and in the actual use case in space. The model is also used to evaluate the temperature gradients between components in order to assess the effectiveness of thermal insulation, and to the approximate heat load on the CubeSat structure. The results are used to iterate on the design choices related to material choices and dimensions in order to reduce the overall heat required. The main conclusions drawn from the thermal network model are as follows:

- Steady state temperature gradients between components are very small (< 5 ° C) as a result of the miniaturized geometry of the system.
- Much less than 10 W of heater power would be required to maintain a 100 °C temperature in the feed system while in the vacuum chamber, whereas more than 10 W would be necessary in space.
- If operating at high temperatures, volume margin should be assigned to the thruster in a CubeSat system design in order to account for sufficient thermal insulation.

Overall the power consumption of the feed systems heaters is expected to be less than 10 W in testing, and more for an actual CubeSat system in space. This power consumption, being only a part of the total power budget, would be daunting for a 3U+ CubeSat. Furthermore, the heat load on the CubeSat is large and significant thermal insulation would be necessary. However, operating at a lower temperatures reduces the input power required and the heat load on the CubeSat structure.

3.2.4. Discharge Chamber

The discharge chamber is responsible for generating the cusped magnetic field configuration of the ACFT device, and as such it's design has significant impact on the thrusters performance. Sintered NdFeB magnets with a conical internal diameter are used for the chamber. They are chosen for their relatively high magnetic flux density ($B_r \sim 1$ T) and a maximum working temperature ($T_c \sim 150$°C) which is compatible with the system operating temperature. The magnetic field strength B outside of the cylindrical NdFeB magnets used can be calculated using Equation 3.7.

$$B = \frac{B_r}{2}\left(\frac{L+z}{\sqrt{r_o^2+(L+z)^2}} - \frac{z}{\sqrt{r_o^2+z^2}} - \frac{L+z}{\sqrt{r_i^2+(L+z)^2}} + \frac{z}{\sqrt{r_i^2+z^2}}\right) \tag{3.7}$$

where B_r is the magnetic remanence field for sintered NdFeB, z is the distance from a pole face, L is the length of the magnet, and r_o and r_i are the inner and outer diameters [11]. At the magnetic pole ($z = 0$), the field strength is between 40 - 50 μG for the magnets used, beyond which the decrease in B is rapid.

The inner surface of the magnets is electrically insulated from the anode and plasma discharge via a patented thin boron nitride ceramic coating [40]. The ceramic has exceptional properties for the task. It's high dielectric constant (4 - 4.6 [1]) and specific resistance (> 10^{14} Ωcm [1]) ensure that a thin coating of boron nitride can insulate the magnets from the anode sufficiently. However increasing the thickness of the discharge chamber coating increases collisions of ions with the chamber walls, leading to a reduction in thrust overall. Furthermore, creating a reliably symmetric coating in the magnet chamber is difficult due to its size.

The entire magnet chamber itself is housed with the anode in a pillar of boron nitride along. This stack of boron nitride cylinders holds the magnets and anode in configuration, while insulating the rest of the thruster from the high voltage of the anode and the plasma. The relatively high thermal conductivity of the ceramic (typically 30 W/K [1]) allows heat to conduct between the anode and chamber, and the surrounding feed system reservoir. O-rings are used to seal the interfaces between the individual boron nitride parts to prevent leaks.

3.3. Performance Characterization

The performance of the µACFT EM is measured using both xenon and iodine propellant. Characterization of the thruster performance includes measuring the thrust generated, the exhaust plume current density and profile, and the total power consumed. When using xenon, the mass flow rate is known and thus the specific impulse can also be calculated. On the other hand, with iodine propellant, the mass flow rate is not known and thus values such as the specific impulse or total Δv can only be estimated.

First, a description of the test facilities, methodologies, and measurements uncertainties is provided. Following is a discussion of observations regarding thruster operations during testing and the resulting performance measurements. Lastly, comparisons are made between the measurements made with the iodine µACFT and previous µACFT devices, as well as other CubeSat thrusters and other iodine thrusters.

3.3.1. Methodology

Historically, experimental characterization of all ACFT devices has been performed at the Laboratory for Enabling Technologies (LET) at Airbus Friedrichshafen. A thorough and detailed description of the Micro-Newton Thruster Test Facility, with all the related plasma diagnostics equipment and the direct thrust measurement tool, is given in the PhD dissertation of F. G. Hey [41]. A general overview can be seen in Figure 3.5. The key elements are the vacuum chamber and pump system, the plasma diagnostics setup, and the micro-Newton thrust balance.

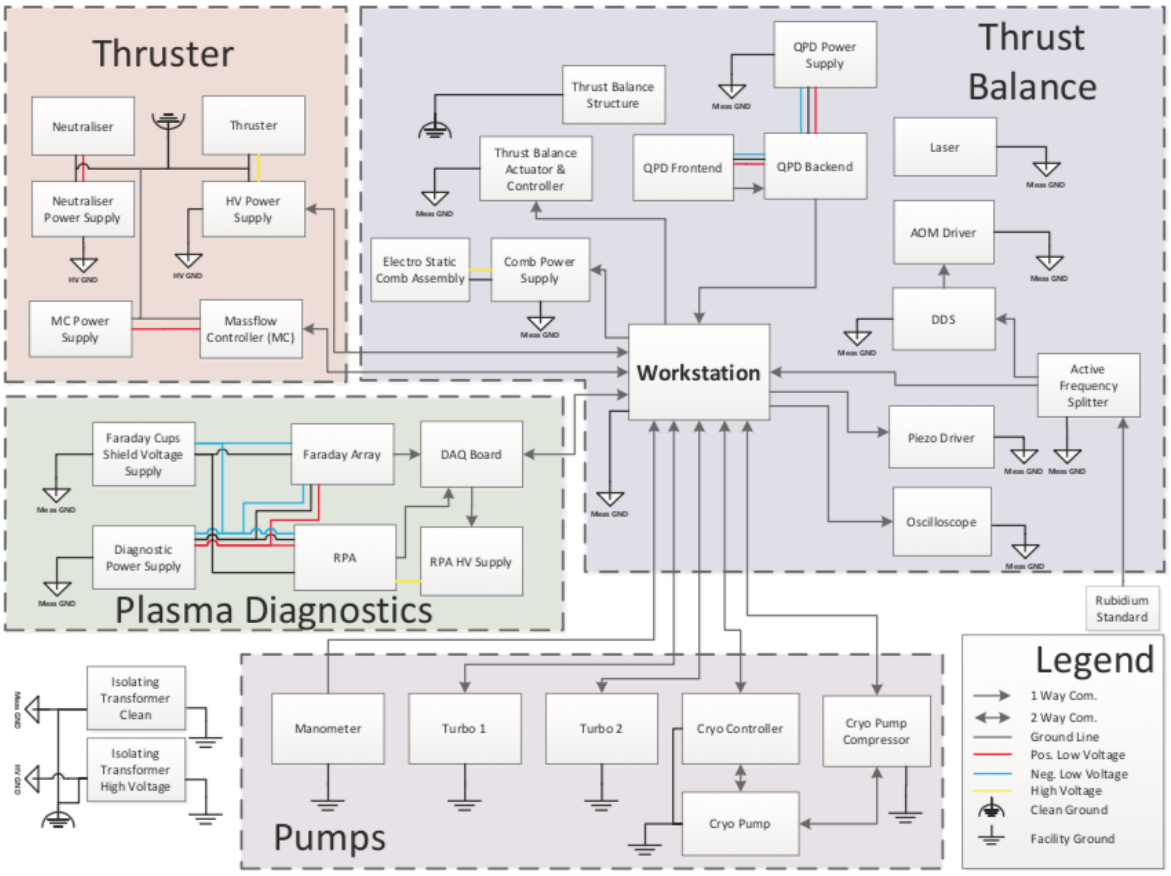

Figure 3.5: Schematic diagram of LET µACFT test facility [41]. All facility controls and data processing are handled by the workstation. There are three vacuum pumps and a large chamber, a direct thrust measurement pendulum, and a plasma diagnostics jib arm used in thruster testing.

Vacuum The vacuum system is necessary in order to test thruster models in an atmosphere which approximates the space environment. The chamber in which the thrusters are placed is roughly 3 m^3, large enough such that the walls do not impose negative influence on the tests, and that the tests do not damage the walls. The tank is isolated from the seismic background noise of the laboratory in order to allow for precise force measurements. The pumping system, composed of a rotary pump, one turbopump, and two cryopumps, achieves an operational pressure of approximately 3×10^{-7} mbar.

Plasma Diagnostics The plasma diagnostics system, used for measurement and characterization of the thruster exhaust plume, consists of a single Faraday cup, which doubles as a retarding potential analyzer (RPA), and one E-cross-B probe on a jib arm. The jib arm rotates about an axis centered underneath the thruster, driving the sensor through a cross section of the plume. The distance between the detectors and thruster can be modulated to account for high or low plume current densities. The Faraday cup is used to measure the current density in the output beam as a function of position, so that the plume divergence and total beam current can be calculated. On the other hand, the RPA is used to obtain information about the energy of the ions. This is achieved by applying a retarding potential in front of the Faraday cup to repel ions with a kinetic energy lower than the electric potential energy of the RPA. By incrementally increasing the retarding potential, a distribution of the ion energies can be constructed. This is also used to measure the actual beam voltage, which relates to the acceleration efficiency of the thruster. The E-cross-B probe applies both a magnetic and electric field to the incoming plume ions in order to separate the particles based on their total charge. In this way the relative abundance of ionization states in the plume can be quantified. However ultimately the E-cross-B probe was not used in characterization of the μACFT as it is still under development at the time of writing.

Measurement uncertainties associated with the plasma diagnostics measurements include alignment errors and asymmetry in the alignment, inaccuracy in measurement extrapolation and numerical integration, dark currents, and electromagnetic interference introduced by the measurement device on the thruster operations.

Thrust Balance The ability to measure micro-Newton thrust forces is a key feature of the overall test facility. The system was specifically designed to test candidate attitude and orbital control thrusters for the LISA mission, and other high precision space science missions in the future. The thrust balance consists of two hanging pendulums: a measurement pendulum and reference pendulum. A heterodyne laser interferometer is used to measure the deflection of the measurement pendulum relative to the reference pendulum with the thruster mounted on measurement pendulum and a symmetric mass on the other. Due to the symmetry of the dual-pendulum setup, many known and unknown noise sources are rejected from the measurements since they are adopted equally by both the reference and measurement pendulums. With adequate damping of the pendulums, the system could be used to detect forces of less than 0.1 μN [41].

Measurement uncertainties associated with the thrust balance include the seismic noise introduced to the pendulums by the cryopump and laboratory workers, uncertainty in the alignment of the thruster on the measurement pendulum, error in balancing the mass of the measurement and reference pendulums, and thermal energy introducing a drift in the pendulum position.

3.3.2. Test Results

A summary of the measurements which are made for performance characterization of the iodine μACFT is shown in Table 3.5. Taken together, the measurements can be used to assess the overall efficiency of the thruster, as well as it's performance with respect total thrust generated, total power consumed, the power-to-thrust-ratio, and the specific impulse. These are standard performance characteristics in the field of the EP, and thus they can be used for comparison of the performance of the μACFT EM to a variety of other similar systems. Characterization of the thruster performance was done through direct measurements when possible. In other cases, the outcome must be calculated based on multiple measurements, or estimated based on a model.

In general, only the anode potential and current and mass flow rate were recorded throughout the entire testing campaign. The other measurements, such as direct thruster and plasma diagnostics, were only conducted on a smaller subset of the operating points as the processes are much more intensive.

Table 3.5: Summary of thruster performance characterization measurements, alongside the intended outcomes and underlying motivation.

Measurement	**Outcomes**	**Motivation**
Direct thrust	Thrust generated, specific impulse (if mass flow rate is known).	RQ-1 and all sub-questions, PRO-006.
Mass flow rate	Specific impulse, mass efficiency.	RQ-1 and all sub-questions, PRO-006.
Plasma plume profile	Ion beam current, divergence efficiency, discharge efficiency, mass efficiency.	RQ-1 and all sub-questions.
Ion energy	Kinetic energy of beam, acceleration efficiency.	RQ-1 and all sub-questions.
Anode potential and current	Contribution to total system power, power-to-thrust-ratio, discharge efficiency.	RQ-1 and all sub-questions.
Cathode power	Contribution to total system power.	RQ-4, RQ-1 and all sub-questions.
Heater power	Contribution to total system power.	RQ-1 and all sub-questions.

Performance with Xenon In order to fully characterize the performance of the μACFT, the system was first tested with xenon. Using xenon allows the thruster specific impulse to be calculated since the mass flow is controlled. Furthermore, with performance benchmarks established using xenon as fuel, differences in performance due to the switch to iodine can be more easily identified. The tests were performed before integrating the iodine feed system. Xenon was fed directly into the anode from a mass flow controller and gas tank outside the vacuum chamber.

Ignition of the thruster was achieved with mass flows between 0.15 - 0.8 sccm, and anode voltages between 800 - 1300 V. Various operating points were observed during the xenon test runs. However, a complete measurement and diagnostics test run was not conducted for each operating point. In general, only the anode voltage, anode current, and mass flow rate are recorded. The observed stable operating points could be grouped into two states, standard operation and current limited operation, based on the current being drawn to the anode. The standard operations were typically characterized and anode voltage in the range 700 - 1500 V, with a mass flow of 0.2 - 0.6 sccm, and resulting anode current between 1.5 - 7.5 mA. These operating points are referred to as standard since they are very comparable to operating points which had been demonstrated with each of the previous μACFT systems [41, 91]. The current limited operation state was encountered with higher mass flow rates, typically 0.4 - 0.6 sccm, where the anode current spiked to the current limit set by the power supply of 20 mA, and the anode voltage fell below 300 V. Operating points of the thruster for which the complete set of diagnostic measurements has been recorded is in Table 3.6.

Table 3.6: Measured operating points of μACFT with xenon propellant.

Voltage [V]	**Mass Flow** [sccm]	**Current** [mA]	**Thrust** [μN]	**Specific Impulse** [s]	**PTTR** [W/mN]
1500	0.30	5.0 ± 0.2	55 ± 1	192 ± 3	136.4 ± 5.2
900	0.60	1.5 ± 0.2	35 ± 1	63 ± 2	42.5 ± 5.7
145	0.60	20.0 ± 0.1	137 ± 1	238 ± 2	21.2 ± 0.1
230	0.35	20.0 ± 0.1	142 ± 1	423 ± 3	31.9 ± 0.2

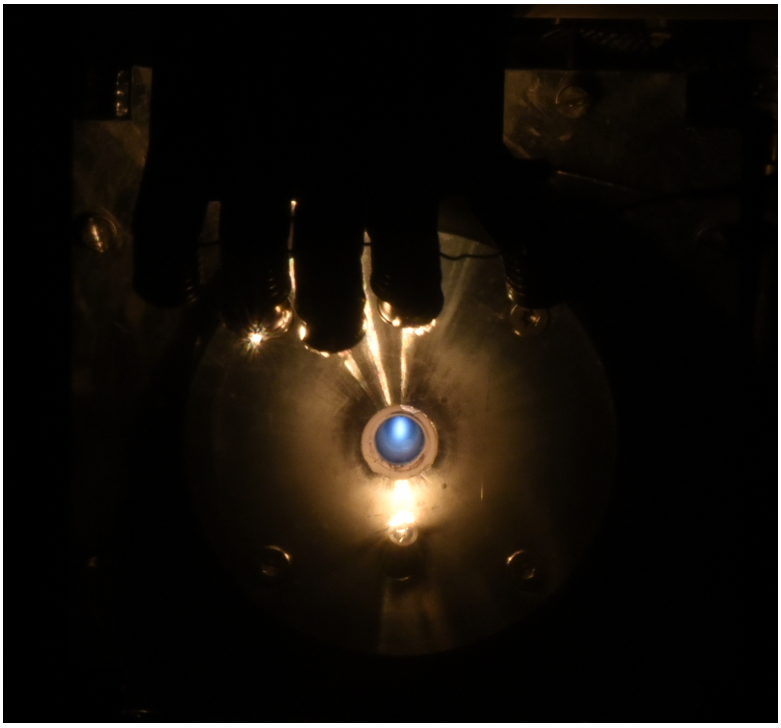

Figure 3.6: µACFT operating with xenon propellant. The blue color is characteristic of the xenon plasma. Multiple tungsten emitters are used for neutralization.

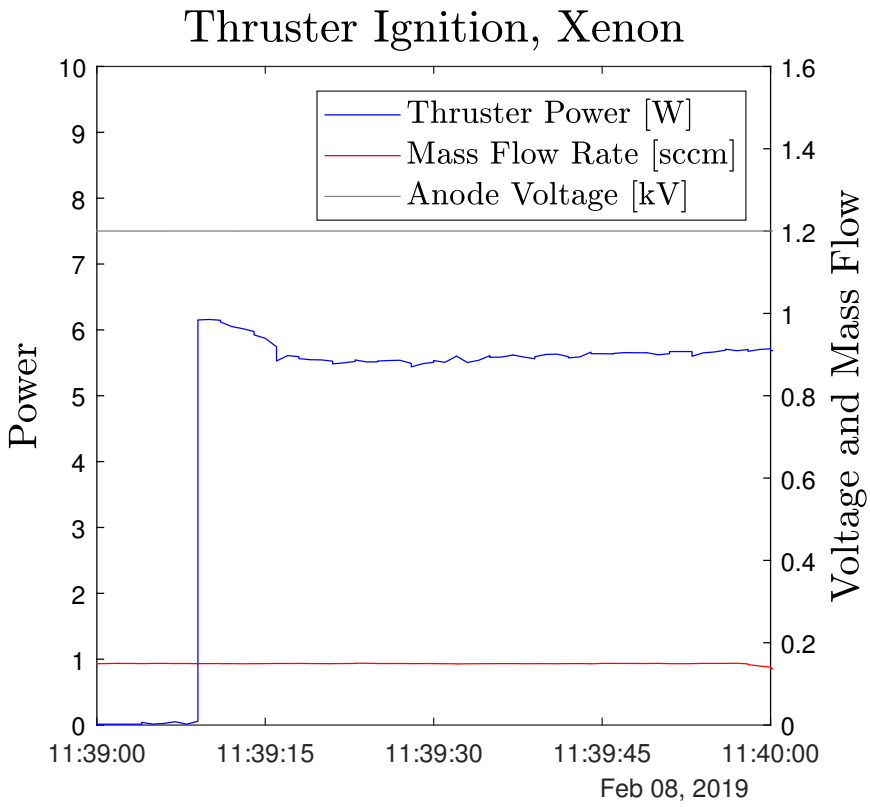

Figure 3.7: Measurements during thruster ignition with 0.15 sccm xenon mass flow and 1200 V anode potential, resulting in a 5 mA current consumption at the anode. No deviation in mass flow or voltage occurs when the current begins to flow.

The 1500 V operating point is most exemplary of typical operating points of the xenon μACFT, where the voltage is high and mass flow is low. The 900 V operating point, where mass flow is high and the ion beam current is low, is closer to the performance of a cold gas thruster and is not a desirable operating point for the μACFT. However in this state, only 3.15 W of power was consumed by the total thruster system. The remaining 145 V and 230 V operating points are representative of the current limited operating state.

The current limited operating state was encountered following an observation that a current composed of thermionic electrons, which varied proportionally with the cathode input power, was reaching the anode before igniting the thruster. By increasing the mass flow rate of xenon to 0.4 sccm or higher while operating at the 900 V standard operating point, the thruster could be forced to transition into the current limited operating state. Figure 3.8 shows the transition, where the anode voltage drops to 235 V while the current and power consumption peak at 20 mA and 4.7 W. At the operating point shown in the figure, the total power consumption of the system 11.6 W. If the power of the neutralizer is decreased further, the thruster would transition back to the 900 V standard operating point, even if a high mass flow rate was maintained. The 900 V operating point in Table 3.6 demonstrates the poor performance of the μACFT after transitioning from current limited to standard operating conditions if the high mass flow is sustained.

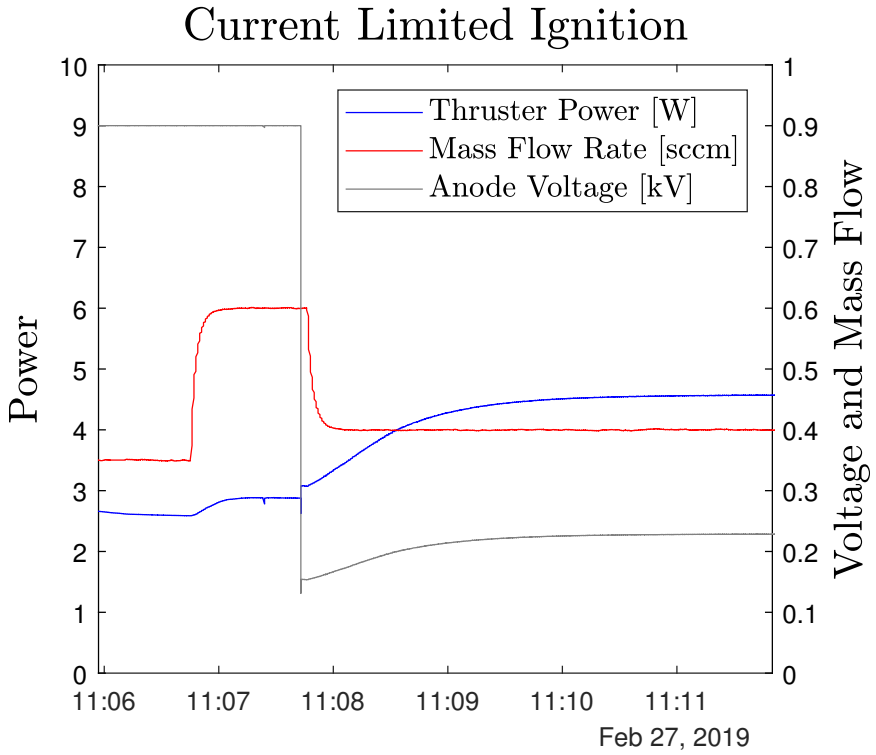

Figure 3.8: Transition into current limited operating state from standard operation state. The transition is achieved shortly after increasing the mass flow rate above 0.4 sccm. It is characterized by a drop in anode potential to less than 300 V, and the anode current rising to 20 mA.

Plasma plume diagnostics measurements were also performed for both the standard and current limited operating states. The retarding potential analyzer (RPA) is positioned at the point where maximum current density is measured in order to characterize the ion energy distribution in the plume. The RPA measurements (Figure 3.9) reveal that ion energies are more widely distributed in the current limited operating state, and in the standard operating state the majority of ions possess kinetic energy nearly equal to the potential energy of the accelerating anode voltage. Thus the total kinetic energy of the beam relative to the accelerating anode potential is higher when the anode potential is higher, if the mass flow is similar. The acceleration efficiency of the thruster is $\eta_v = 99.3\%$ for 1300 V and $\eta_v = 88.4\%$ for 145 V. This is determined by the retarding potential relative to the anode voltage ($\eta_v = V_b/V_a$) at the point where the ion beam current falls to zero.

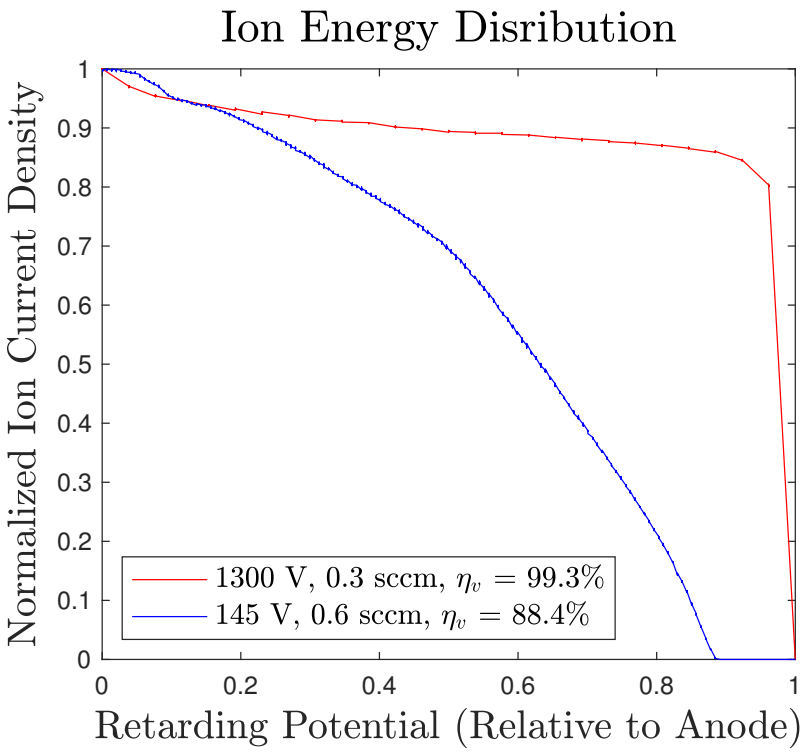

Figure 3.9: Xenon ion energy density distribution for 1300 V and 145 V thruster operating points. The results indicates that at high voltage, the particles kinetic energy is tightly bound to the accelerating potential energy of the anode, while at lower voltage the distribution is wider. This results in a lower acceleration efficiency (88.4%) at 145 V and compared to at 1300 V (99.3%), which are determined by the point at which the current density falls to zero.

Figures 3.10 and 3.11 shows the current density and plume profile of the μACFT for both states. The total beam current, I_b, is determined by performing a numerical integration of the cross-sectional measurement of the plume across a semi-sphere:

$$I_b = \sum J_{meas} A \cdot 4\pi R^2 |\sin(\phi)| \sin(\Delta\phi/2) \tag{3.8}$$

where R is the distance between the thruster and Faraday cup, ϕ is the angular position of the Faraday cup relative to the thruster, $\Delta\phi$ is the angular resolution of the measurements, A is the area of the inlet to the Faraday cup, and J_{meas} is the discrete current density measurement [50]. The direct plume measurements are indicated by red markers. The blue line is fitted to the direct measurements, and extrapolated, assuming perfect symmetry of the plume, to account for measurements which were missed due to obstructions in the path of the jib arm and asymmetry in the measurement setup.

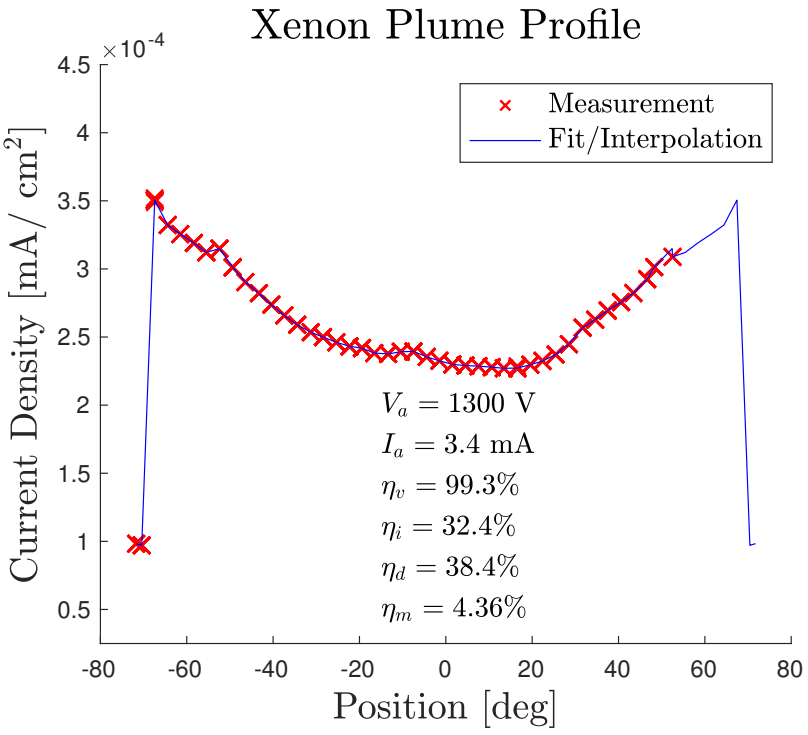

Figure 3.10: Xenon ion plume profiles at high anode potential. "U" shaped profile at 1300 V indicates significant E-cross-B drift causing the plume to diverge. In combination with the low discharge and mass efficiencies, the result is an overall low total efficiency.

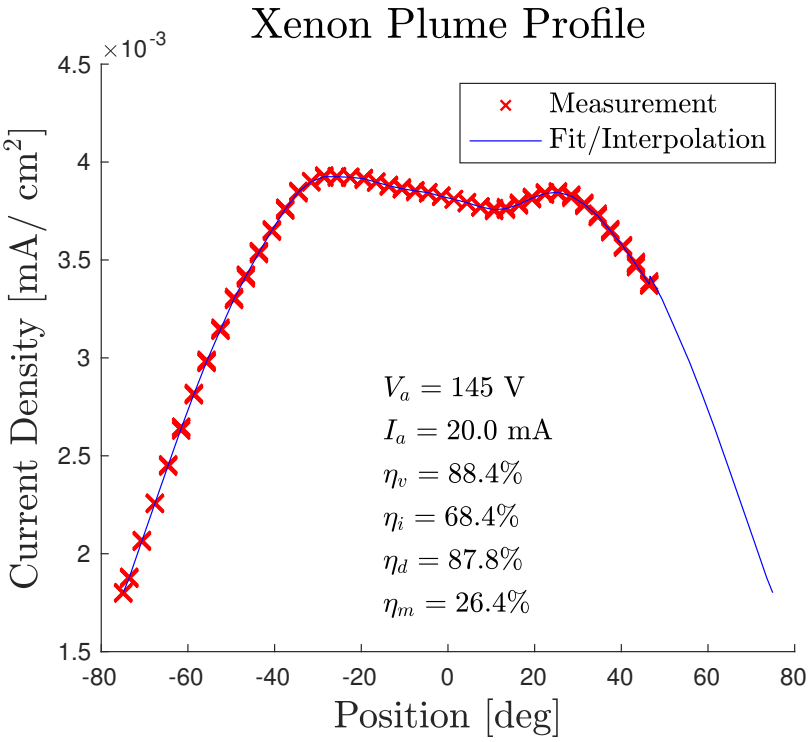

Figure 3.11: Xenon ion plume profiles at low anode potential. The overall efficiency of the thruster is high since the beam divergence is very low and the discharge and mass efficiencies are relatively high.

The plume profile measured at 1300 V is similar to measurements made with previous ACFT systems [41, 91] in that at high anode voltages, the plume takes on a "U" shape. For comparison, the measured plasma plume profile of the previous xenon μACFT EM is included in Appendix B (Figure B.3). The large beam divergence which occurs at high anode potentials is a result of the increased E-cross-B drift force pushing the ions in the radial direction toward the chamber walls. The sharp drop off in beam current at the edges of the 1300 V plume indicates ions are colliding with the chamber walls. The reduction of the anode voltage results in a in an inversion and narrowing of the plume profile compared to the high voltage measurement. The narrowing of the beam may be a driver in stimulating a larger plasma breakdown, which is noted by the 20 mA anode current and order of magnitude increase in the plasma plume current density.

The mass efficiencies presented in the plot are calculated assuming that 20% of the ions in the plume are doubly ionized, and that 80% are singly ionized [110]. This implies that on average, an ion in the plume has a charge of $Q = 1.1q$. The mass efficiency is then calculated with Equation 3.9, where M_i is the mass of an ion.

$$\eta_m = \frac{I_b M_i}{Q\dot{m}} \tag{3.9}$$

The overall efficiency of the thruster was 0.6% (1300 V, 0.3 sccm) and 13.9% (145 V, 0.6 sccm) according to Equation 2.12. The performance of the thruster improved in almost all respects in the current limited operation state, with the exception being the acceleration efficiency. A comparison of the characteristics of the two operation modes is shown in Table 3.7.

Table 3.7: Comparison of standard and current limited operating modes.

Operating Mode	**Characteristics**
Standard	$V_a = 700 - 1500$ V
	$I_a < 7.5$ mA
	$F_t < 100$ μN
	Higher η_v.
	Lower $\eta_m, \eta_i, \eta_d, \eta_T$.
Current Limited	$V_a = 150 - 300$ V
	$I_a = 20$ mA
	$F_t > 100$ μN
	Higher η_m, η_i, η_d and η_T.
	Lower η_v.

The performance in the current limited case is greater for few reasons. First, the lower voltage leads to a lower beam divergence and thus a greater efficiency with respect to momentum transferred to the thruster by each ion. Furthermore, the larger plasma discharge ultimately lead to higher mass and discharge efficiencies.

Performance with Iodine By switching to iodine propellant, direct control and monitoring of the mass flow rate is lost. Furthermore, since both too little and too much propellant can restrict the ability of the thruster to function, ignition of the μACFT using iodine propellant proved to be more difficult than with xenon.

First of all, the mass flow rate of iodine through the thruster appears to be significantly higher than the mass flow rate used in operations with xenon, and thus it was not possible to test at all of the points which had been previously mapped using xenon. Furthermore, backfiring became a common issue when attempting to ignite the thruster. During so-called backfiring events, only very short, high power sparks would form in the discharge chamber. These short discharges could be as high as 60 W. Instead, a sustainable plasma breakdown would be generated in the reverse direction, inside the feed system of the thruster. The ignition of such a plasma is shown in Figure B.2 in Appendix B. The discharge shown is similar in power to 900 V standard operating points measured during xenon testing. Since any conductor inside the feed system could act as a ground and electron source for the discharge, all had to be removed or concealed to prevent the vapour from coming in contact with a grounded conductor. Thus the valve head sealing the propellant reservoir was removed and replaced with a pinhole orifice during testing.

The backfiring of the thruster into the feed system is explained by the Paschen breakdown curve. Figure 3.12 shows the Paschen breakdown curve for a small range of secondary electron emission fractions assuming a 30 mm discharge length. This discharge length is chosen as it is nearly identical for a discharge from the anode to the cathode or to the edge of the aluminum tuna can housing. For this plot the Townsend coefficients of air are used, since the coefficients are not readily known for iodine. As a result, there is an unknown error incurred between the voltages and pressures shown in the figure, and what the reality would be for a pure iodine vapour. The errors are not critical as the analysis is used to mount an argument for why thruster backfiring occurs based on the form of the Paschen curve.

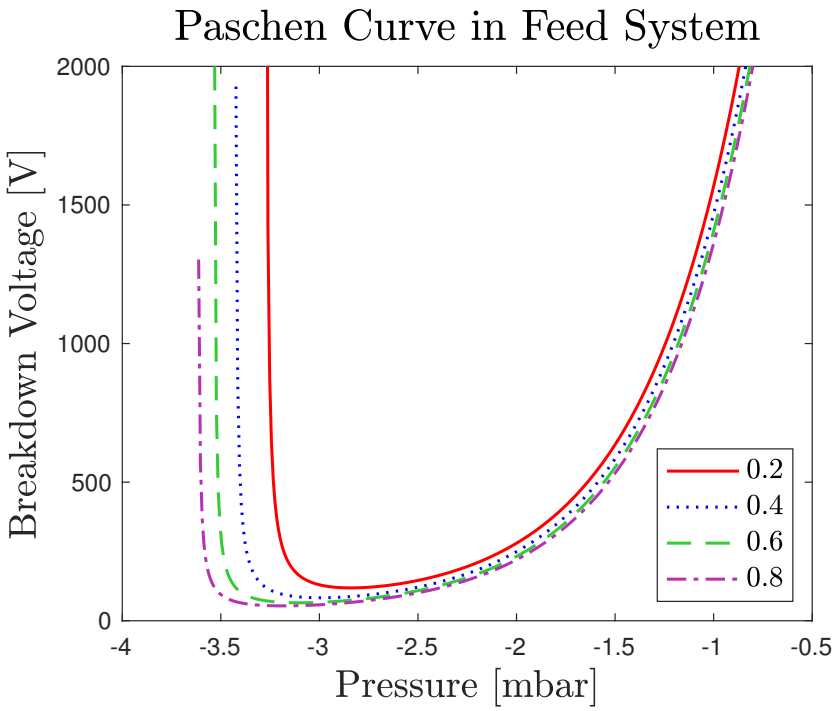

Figure 3.12: Paschen curve is based on Townsend coefficients of air, and is shown for various secondary electron emission coefficients. At room temperature and slightly higher, the pressure inside the secondary chamber of the feed system is near the minimum of this Paschen breakdown curve. However in the chamber the pressure is closer to the surrounding vacuum pressure and thus on the steep left-hand side of the curve. As a result, the breakdown voltage inside the feed system is lower.

The breakdown voltage is near the minimum when the gas pressure is in the range of 10^{-3} - 10^{-2} mbar. The breakdown voltage at this minimum is below what is necessary to ignite the thruster and thus operating at this pressure level will consistently lead to backfiring before ignition. In the multistage orifice-separated feed system design for the μACFT, the pressure in the secondary chamber is near the upper end of this range at room temperature (detailed description in Section 4.2). As a result, the risk of plasma breakdown inside the feed system is high during ignition. According to Figure 3.12, the issue of backfiring can be addressed either by increasing or decreasing the pressure in the secondary chamber reach the regions of the curve where the breakdown voltage is much higher.

In order to reduce the pressure, the orifice size must be decreased. However achieving the required pressure gradient while simultaneously maintaining mass flow through the orifice becomes impossible. There are no solutions to Equation 3.2 which would allow for a mass flow rate greater than 0.2 sccm at a temperature above 20°C while generating a pressure in the secondary chamber which is lower than the minimum of the breakdown curve.

Instead the pressure in the feed system is increased by operating at a higher temperature. At 60°C, an order of magnitude improvement in vapour pressure and a doubling of the breakdown voltage inside the secondary chamber is achieved. However, mass flow rate of the feed system increases exponentially with temperature. As a result, the iodine μACFT could not be tested at the low mass flow standard operating points which could be achieved with xenon. Nonetheless the thruster could be ignited directly into a current limited operating state. However, the ignition was always proceeded by a series of high power, short duration discharges inside the magnetic chamber. This is evident in the spikes in anode voltage seen in Figure 3.13

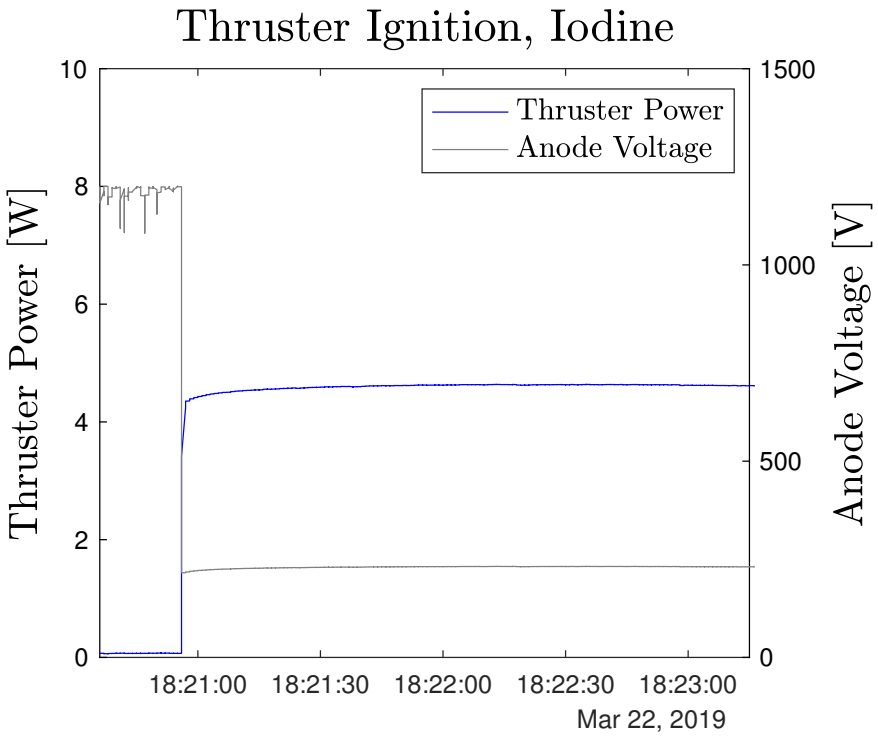

Figure 3.13: Thruster power consumption and anode voltage during thruster ignition into current limited state with iodine. Sparking is evident due to the spikes in anode voltage prior to ignition. Temperature of the reservoir is 50°C and secondary chamber temperature is 62°C.

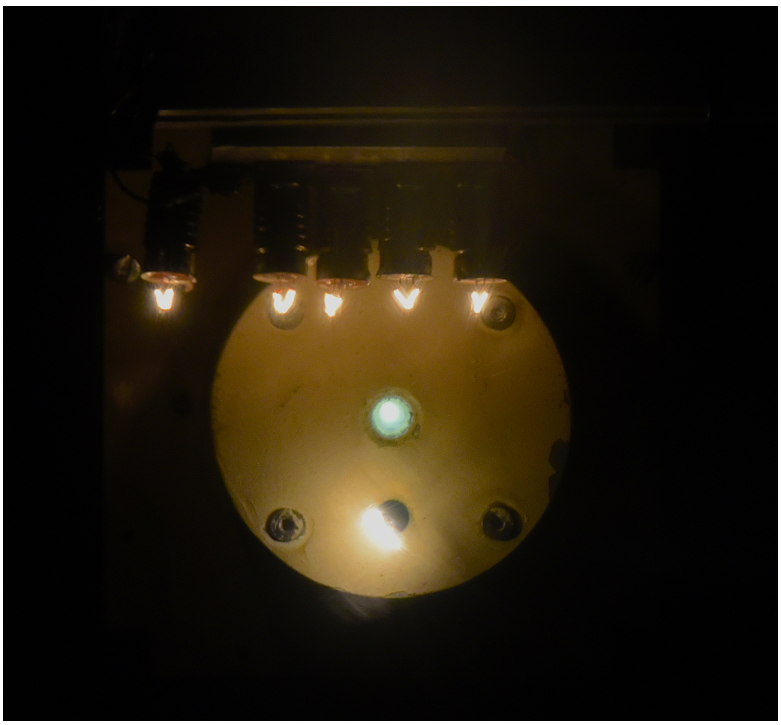

Figure 3.14: µACFT operating with iodine propellant. The iodine plasma emits a pale yellow light. The thruster is covered in a emissive coating to increase radiation and reduce thermal loading on the pendulum arm. Multiple tungsten emitters are used for neutralization.

Following ignition, the anode voltage would sometimes rise up to 400 V, but ultimately settle into the range 210 - 250 V. This observation could be an indication of a release of iodine deposits in the feed system giving a short-lived surge of propellant and power. The range of thruster power consumption is 4.2 - 8.0 W. An operating state at about 240 V could be maintained so long as the reservoir temperature did not exceed 50°C and the secondary chamber temperature did not fall below 60°C. At these operating temperatures, the power required to maintain the feed system temperature in the vacuum chamber is 0.9 W. However with the thruster running, the temperature would slowly rise. This leads to an extinction of the plasma discharge as excess mass flow is introduced.

Table 3.8: Measured operating point of μACFT with iodine propellant. * indicates estimated quantity.

Voltage [V]	**Mass Flow** [sccm]	**Current** [mA]	**Thrust** [μN]	**Specific Impulse** [s]	**PTTR** [W/mN]
241 - 245 ± 5	2.07 ± 1.00 *	20.0 ± 0.1	227 - 254 ± 1	115 - 128 ± 48 *	19.1 - 21.3 ± 0.4

The thruster is photographed in Figure 3.14 at the 240 V operating point. At this operating point, the entire system consumes a total 8.3 W of power. The performance of the thruster is summarized in Table 3.8. The mass flow rate in the thruster is estimated based on the feed system model described in Section 4.2, assuming a 0.03 mm^2 orifice size. However since this model is an approximation and the actual mass flow rate is not measured, the uncertainty is high.

The ion energy density distribution of the iodine discharge is shown in Figure 3.15. The ion energy distribution of the iodine plume is a more closely grouped around the anode voltage than the 145 V point discussed previously, but still much less tightly than in the 1300 V case (Figure 3.9). The acceleration efficiency of the thruster at this 210 V operating point is 96.7%, and thus is also in between that of the 1300 V and 145 V operating points. However, due to the higher estimated mass flow rate of the iodine propellant, the total kinetic energy of the beam is high.

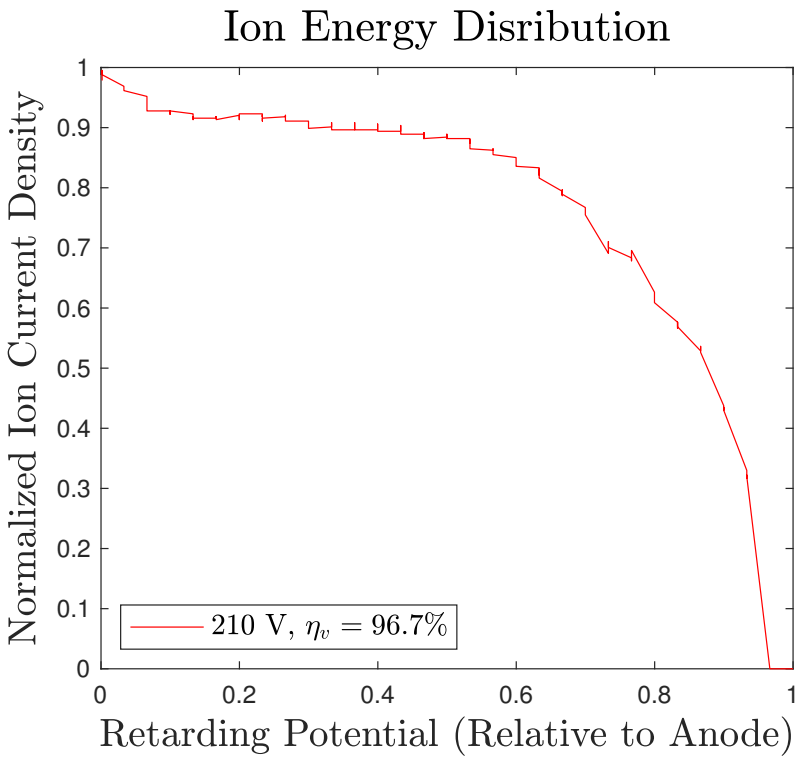

Figure 3.15: Iodine energy density distribution. The acceleration efficiency is determined by the point at which the current density falls to zero. Furthermore, the kinetic energies of the particles are not tightly grouped around the accelerating potential energy of the anode.

The iodine plume profile presented in Figure 3.16 is quite different from the those measured in the xenon testing campaign (Figures 3.10 and 3.11), but again comparable to the the ion plume profiles measured with previous µACFT and ACFT systems. The "M" shaped plume profile is characteristic of a thruster operated at a moderate anode potential (300 - 400 V), and is also comparable to a measurement made with the previous µACFT EM (Figure B.3) [41, 91]. The plume profile appears lopsided because the cathode neutralizer was not correctly centered underneath the discharge chamber exit, visible in Figure 3.14. The mass efficiency presented is also calculated assuming a 20% rate of double ionization in the ion plume (Equation 3.9).

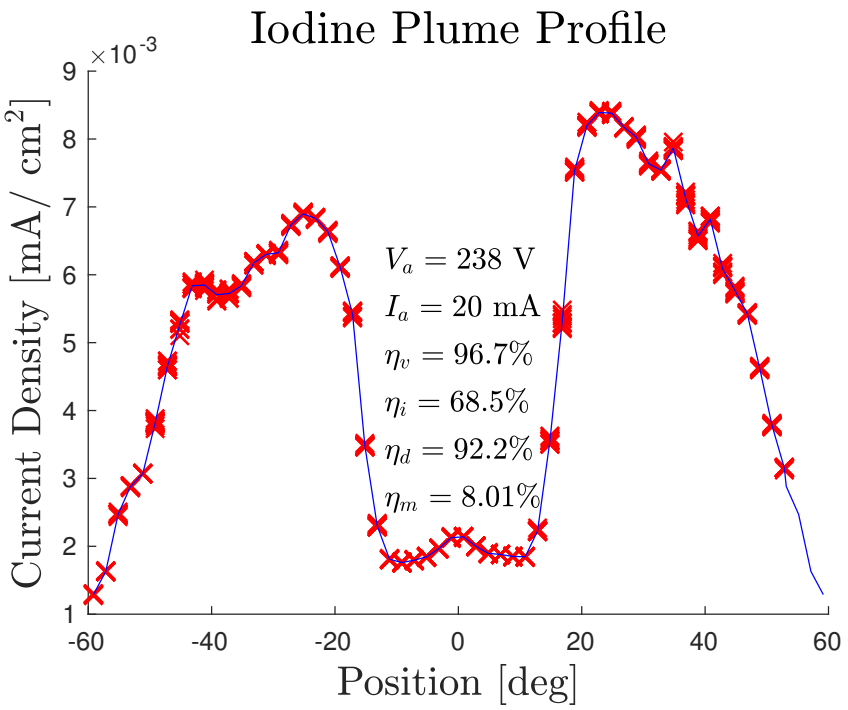

Figure 3.16: Iodine ion plume profile at an anode potential of 238 V. The mass efficiency is estimated since the actual mass flow rate of propellant is not known. The overall efficiency of the thruster is 4.3%.

3.3.3. Comparison of Performance Measurements

The performance of the µACFT with respect to total power consumption, power-to-thrust-ratio, specific impulse, thrust generated, and thruster efficiency were measured and calculated. Here these performance parameters, as well as the total size and mass of the system, are compared to previous µACFT systems, other CubeSat thruster systems, and other iodine thrusters.

Comparison to Previous µACFT Systems Figure 3.17 is a direct comparison of the measurements presented in this thesis with performance measurements of previous µACFT LM and EM at discrete operating points. The ideal region for a performance measurement to inhabit in this plot is the upper left corner. This region of the plot corresponds to a high specific impulse with a simultaneously low power-to-thrust-ratio. Relative to all other measurements and µACFT models, the current limited operating points demonstrated by the current µACFT EM are characterized by higher total thrust and lower power to thrust ratio. The highest specific impulse measured with the current EM is also relatively high in comparison to the previous EM.

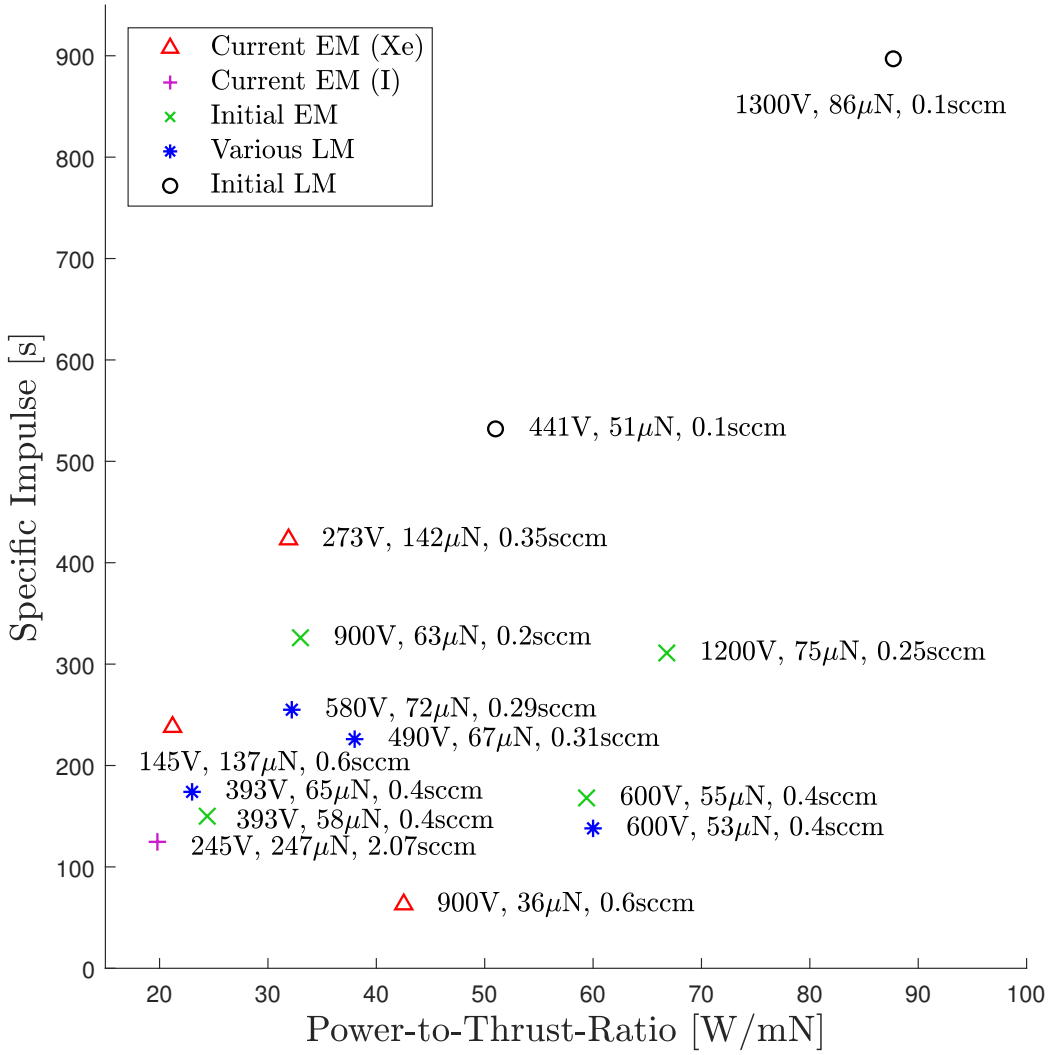

Figure 3.17: Performance achievements with µACFT systems dating back to the initial laboratory model. The ideal region for a measurement is the top left corner, where the thruster is most efficient relative to power consumption (low PTTR) and propellant consumption (high I_{sp}). The current EM demonstrates a low PTTR compared to the other systems. The I_{sp} varies wildly based on the operating point. With high mass flow at 900 V, the I_{sp} is comparable to a cold gas thruster, whereas with 273 V and a lower mass flow, the I_{sp} is higher than most other µACFT systems.

Table 3.9 shows a summarized comparison of the full range of operating points explored with the various μACFT systems.

Table 3.9: Comparison of performance characteristics of μACFT CubeSat engineering model (EM) and laboratory model (LM) systems.

Thruster	**Fuel**	**Anode Power** [W]	**Thrust** [μN]	**Efficiency** [%]
CubeSat LM [41]	Xenon	0.8 - 7.1	29 - 86	2.0 - 7.0
CubeSat EM v.1 [91]	Xenon	1.3 - 6.7	63 - 75	1.0 - 3.0
CubeSat EM v.2	Xenon	1.5 - 9.3	35 - 142	0.6 - 13.9
CubeSat EM v.2	Iodine	4.5 - 8.2	227 - 254	4.3

The μACFT EM presented in this thesis demonstrated exceptional performance with respect to thrust generated, power-to-thrust-ratio, total thruster efficiency, and specific impulse. The current EM demonstrated better performance than the previous μACFT LM and EM systems with respect to power-to-thrust ratio [41, 91]. Furthermore, the highest measured specific impulse is improved compared to the previous EM. However, the best measurements of power-to-thrust-ratio and specific impulse did not take place simultaneously. Furthermore, the best results were measured in the current limited operating state.

The performance of the current μACFT model with respect to the specific impulse is poorer with iodine than with xenon. This is in large part due to the estimated mass flow rate in the iodine test being many times larger than that of xenon. As a result, the thrust generated with iodine is significantly higher, but the specific impulse is much lower. The larger thrust contributes to the low power-to-thrust-ratio measured with iodine.

Comparison to Other Iodine Thrusters A list of iodine thrusters which have been discussed in literature is shown in Table 3.10, alongside measured or expected performance specifications.

Table 3.10: Comparison of performance characteristics of iodine thrusters. * indicates target performance specifications

Thruster	**Total Power** [W]	**Thrust** [mN]	**Efficiency** [%]
Airbus DS μACFT	8.3 - 11.6	0.23 - 0.25	4.3
ThrustMe Neptune [80]	30 - 60 *	0.2 - 0.7 *	N/A
Busek BIT-3 [103]	55 - 75	0.65 - 1.14	N/A
University Giessen RIT-10 [45]	65 - 82	0.1 - 1	N/A
Airbus DS ACFT [111]	104	4.7	N/A
Busek BHT-200I [49]	200	13	31
Busek BHT-600I [49]	600	40	50

The field of iodine thrusters consists of three small systems (μACFT, Neptune and BIT-3), and four larger systems (RIT-10, ACFT, BHT-200I and BHT-600I). The μACFT is the smallest thruster on this list with respect to total volume, power consumption and maximum thrust. Typically, the larger thrusters operate with a lower power-to-thrust-ratio and higher total efficiency compared to the smaller thrusters. However the power-to-thrust ratio of the current iodine μACFT EM is more comparable to the larger thrusters than the smaller ones.

Notable entries in the list include the Neptune thruster from ThrustMe and the BIT-3 from Busek. The Neptune and BIT-3 are both gridded ion engines which are also targeting CubeSat applications, making them the most comparable systems to the iodine μACFT. However both thrusters are many times larger than the μACFT. The BIT-3 takes up 1615 cm^3 (nearly 2U) with a wet mass of 3 kg, and the Neptune 1000 cm^3 (1U) with a wet mass of 1 kg. Furthermore, both the total power consumption and power-to-thrust-ratio of the μACFT are lower than the expected values of the Neptune and the measured values of the BIT-3. However both of these systems are expected to generate a specific impulse which is two to five times higher than that of the μACFT. These differences make the Neptune and BIT-3 more suitable for larger CubeSats, 6U and 12U for example, where the volume and power allowances as well as total CubeSat mass are larger. On the other hand, the μACFT is better suited for a smaller platform with a tighter volume and power budget and lower total mass, such as the 3U+.

Comparison to Other CubeSat Thrusters Figure 3.18 shows the performance of a variety of thrusters available for CubeSat missions ranging up to a power consumption of 50 W and mass of 1 kg. The left-hand side of the plot references only electric thrusters, whereas the right-hand side shows all available thrusters. The operating points at 230 V from Table 3.6 and 245 V from Table 3.8 are featured in the plot.

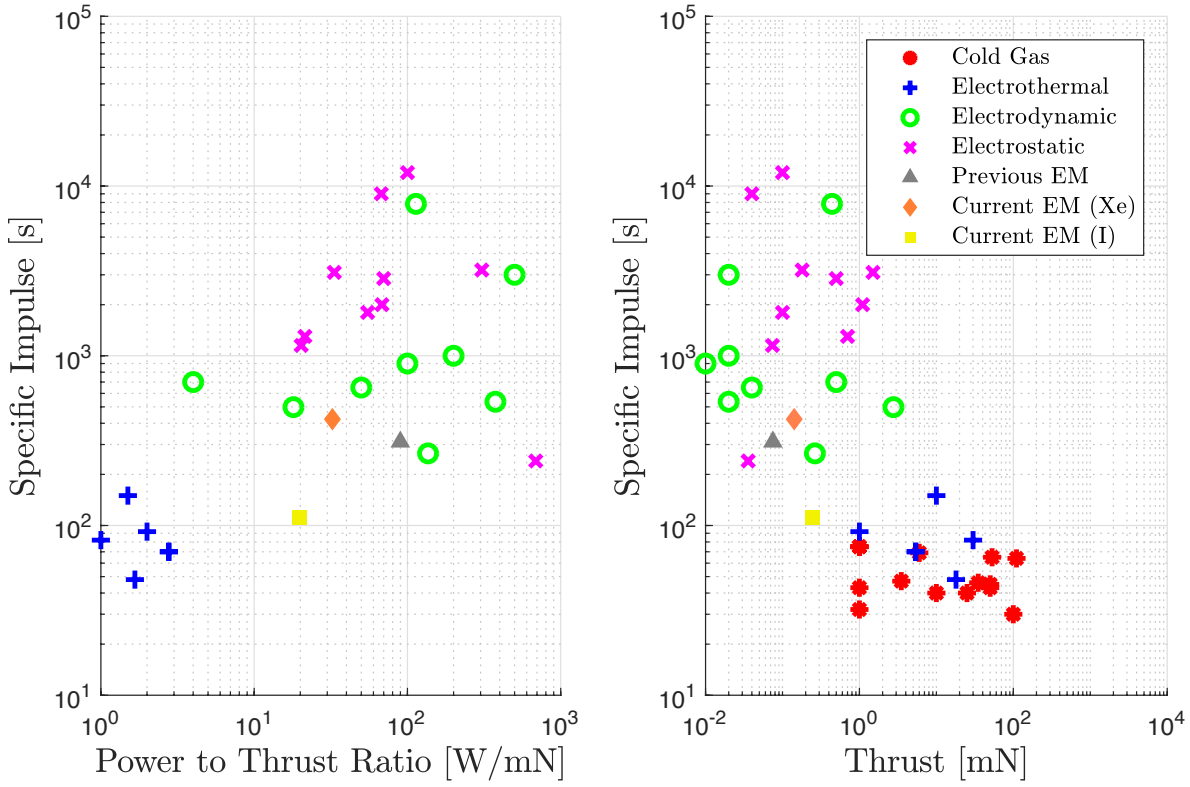

Figure 3.18: Comparison of µACFT performance to other thrusters for CubeSat applications. Data is compiled from [58, 69, 106**?**]. Left: Only electric thrusters, plotted according to power-to-thrust-ratio and specific impulse. Right: all available CubeSat thrusters below 50 W and 1 kg, plotted according to thrust and specific impulse. The µACFT measurements are ranked highly in power-to-thrust-ratio, moderate in thrust, and low in specific impulse compared to electrostatic and electrodynamic thrusters.

In general, the performance measurements µACFT EM fits in with the cluster of electrodynamic thrusters in the region representing low thrust but moderate to high specific impulse and power-to thrust-ratio. Considering only electrodynamic and electrostatic thrusters, to which the µACFT is more comparable, the power-to-thrust-ratio of the current µACFT EM is highly ranked. However the specific impulse of the thruster ranks low in comparison to the thrusters in these categories.

Table 3.11 shows a comparison of the µACFT with a some similar electrodynamic thruster systems [58]. In this comparison, the total power consumption of the µACFT system is considered, not just the power in the thrust chamber. With a total dry mass of 280 g and a 6.4 cm diameter by 5.6 cm height, the µACFT is comparable in size and mass to the smallest options in this field of CubeSat thrusters. However the packaging of the µACFT into the 3U+ tuna can extension is a unique advantage in the context of CubeSat system design, as other thrusters are less isolated from the main body of the CubeSat. Furthermore, the thrust of the µACFT is much greater than that the alternatives in this category. Another advantage is the low EMI of the µACFT, relative to the pulsed plasma thrusters (PPT). However, the notable deviation is still the lower specific impulse of the µACFT.

With an improved specific impulse, the µACFT would be a great option for a 3U+ or larger CubeSat mission. The relatively low power consumption and form factor make it easy it integrate and a higher specific impulse would make it very versatile. Currently, the µACFT would be best suited for 3U+ CubeSat station keeping or de-orbiting.

Table 3.11: Comparison of small electrodynamic thrusters for CubeSats [58].

Thruster (Propellant)	F_t or F_ts	I_{sp}	P_{tot}	Dry Mass	Size
Airbus DS μACFT (Xe)	35 - 142 μN	63 - 423 s	3.15 - 11.6 W	N/A	N/A
Airbus DS μACFT (I)	227 - 254 μN	103 - 115 s	8.3 - 11.6 W	280 g	180 cm^3
Mars Space PPTCUP (PTFE)	40 μNs	~640 s	2 W	280 g	203 cm^3
Fotec GmbH PPT (PTFE)	2.5 - 10 μNs	900 s	< 1 W	300 g	243 cm^3
GWU μCAT (Metal)	1 - 20 μN	3000 s	< 10 W	200 g	200 cm^3
U. Illinois μBLT (Al)	54 μN	N/A	4 W	250 g	64 cm^3 (PPU)

3.4. Discussion and Conclusion

In this chapter, the derivation of system requirements and overall design of the iodine μACFT engineering model is described. The EM is a miniature cusped field electric thruster consisting of an iodine feed system, high voltage anode, magnetic discharge chamber, and thermionic emitter cathode. The thruster is designed so that it integrates inside the tuna can extension of the 3U+ CubeSat structure, taking up only a small fraction of the internal volume of the main body of the spacecraft. The novel element of the μACFT design is the propellant feed system architecture. By using iodine propellant, pressurized gas tanks and feedlines are forgone in favour of two-stage feed system design which supplies propellant to the anode directly from the reservoir. The compact feed system design leads to a small overall form factor, and low power consumption required for heating.

Following the design description is an overview of the testing facility and the methodologies employed in the thruster performance characterization. Then the measurement results are presented for both xenon and iodine propellant. Various comparisons are drawn to previous μACFT systems, as well as other iodine and CubeSat thrusters to contextualize the μACFT performance.

The first test conducted used xenon propellant in order to validate the construction of the μACFT. This also allows the opportunity for direct comparison of thruster performance using both xenon and iodine propellants. The thruster demonstrated two distinct modes of operation with xenon propellant. The first, referred as the standard operating mode, is typical for the μACFT based on previous models [41, 91]. In this mode, the anode potential is very high (700 - 1500 V), and the current low (1.5 - 7.5 mA). The alternate mode, the so-called current limited state, had not been discussed in the context of the legacy of μACFT development. It would occur when the mass flow rate of the thruster was high (≥ 0.4 sccm), and would result in a low anode potential (140 - 300 V), but high current (20 mA, limited by the power supply). While the standard operating points led to performance in terms of specific impulse (100 - 300 s), thrust (35 - 55 μN), and power-to-thrust-ratio (43 - 136 s) which are comparable to previous μACFT systems, the current limited operating points demonstrated superior performance with respect to thrust generated (> 100 μN), specific impulse (238 - 423 s), as well as total thruster efficiency (> 10%). The main disadvantage was that a lower anode potential would lead to a lower acceleration efficiency.

With iodine propellant, only the current limited operating state could be achieved. This is a result of the high mass flow rates which were generated by the feed system. The mass flow rate of the thruster could not be throttled down since at lower mass flow rate, the feed system pressure decreases and the thruster would discharge into the feed system but not the discharge chamber. However, once ignited, the performance of the iodine μACFT exceeded the measurements made in the xenon testing with respect to thrust generated and power-to-thrust-ratio. However much of the additional thrust is likely due to the larger mass flow rate. A large mass flow rate is also responsible for the decrease in specific impulse relative to that measured with xenon. Another notable difference between performance with xenon and iodine was the total power consumption of the thruster while in the current limited operating state. With iodine, the μACFT could run with a minimum of 8.3 W of total power, while with xenon the minimum was 11.6 W. The extra power while testing with xenon was consumed by the neutralizer. If this power was reduced, the thruster would transfer into the standard operating state, and performance would degrade. However the absolute minimum power consumption measured with xenon propellant is 3.5 W.

The μACFT EM presented in this thesis is the first to be operated with iodine propellant, and has demonstrated good performance with respect to thrust, power-to-thrust-ratio, and total thruster efficiency when comparing to previous μACFT systems. With respect to other CubeSat electrostatic and electrodynamic thrusters under 50 W and 1 kg, the power-to-thrust-ratio of the μACFT is very highly ranked. The small size and unique packaging of the μACFT is also notable when comparing to other electrodynamic thruster in it's class. However, despite the specific impulse measured of the μACFT being the highest recorded of any μACFT device since the original LM demonstrator, the specific impulse of the system is very low relative to other electrostatic and electrodynamic thrusters. In most cases, the specific impulse of the μACFT lies in between a high I_{sp} cold gas or electrothermal thruster and low I_{sp} electrostatic or electrodynamic thruster.

Aside from the choice of propellant, some other aspects of the μACFT design had an impact on the performance. For one, the positioning of the discharge chamber relative to the end face of the thruster housing was observed to have a direct effect on the divergence efficiency of the thruster. In the current EM, the discharge chamber is displaced further inward relative to the end face of the thruster. As a result, some ions which would have escaped the chamber at a high divergence angle in the previous μACFT systems collide with the walls of the chamber near the exit. The collision of these ions with the walls leads to a faster degradation of the insulating coating applied in the chamber. Since this is the only significant design change with respect to the discharge chamber of the thruster, the position of the discharge chamber may also contributing to the current limited operating state. However, reducing collisions with the chamber walls by moving the discharge chamber close to the end face may would likely lead to an improvement in the specific impulse of the thruster.

Insulation also plays an important role in the reliability and consistency of the thruster performance. When the magnetic chamber is not properly insulated from the anode voltage, the performance of the thruster degrades since the accelerating voltage across the chamber is reduced. Furthermore, insulation inside the feed system is critical in order to prevent backfiring. In order to achieve this the an insulating material must prevent the vapour in the feed system from coming in contact with any grounded conductors.

4

Feed System Fluidics

The rate of propellant flow through a thruster is a driving factor in generating thrust, and thus it effects the overall performance of the device. For this reason it is critical to be able to be able to predict or monitor the propellant mass flow rate into the thruster. The μACFT operates on granular propellant, which must first be vaporized before being fed into the thruster. Furthermore, in the effort to miniaturize the entire thruster for compatibility with the 3U+ CubeSat, a standard mass flow controller and piping feed system design is abandoned. This simple change is a key difference in the propellant feed system design which obscures the actual mass flow rate in the thruster. Furthermore, the miniature dimensions of the thruster, as well as the relatively high pressure differentials that exist between the propellant reservoir and the vacuum of space, make it difficult to predict what the flow regime of the vapor through the feed lines would be.

The problem of the mass flow rate of propellant into the thruster can be broken into two sub-problems: the rate of generation of vapor in the reservoir, and the flow rate of vapor through the feedlines. In flow modelling of the iSAT thruster, the Polzin et. al. use the Langmuir quasi-equilibrium sublimation equation to estimate the rate of vapor generation [79]. This model can also be used for the μACFT system, so long as it is still applicable in the case that there is no mass flow controller. However aside from the vapour generation rate, the mass flow rate in the thruster also depends on the flow regime in the feed system.

This chapter provides a description of tests conducted to assess the suitability of the Langmuir quasi-equilibrium sublimation equation, as well as to determine the flow regime in the feed system and estimate the mass flow rate through the feed lines. The results of the tests are analyzed and used to create a flow system model for the μACFT. In the conclusion the results of the model and limitations of the model are discussed, as well as the implications on the feed system design.

4.1. Sublimation Rate and Flow Regime

Noting that the propellant feed system can be characterized by the rate of sublimation of iodine and the flow regime of the feed system is the basis for understanding of the feed system fluidics. The rate of vapour generation and flow are dependant on the pressure and temperature of the system as well as the dimensions of the feed system. In order to characterize the feed system, either complicated thermodynamic models or direct measurements of the influential factors are necessary. However due to the size of the feed system, accurate direct pressure measurement in the feed lines is difficult. Likewise, because of the complex thermal and electrodynamic processes in the thruster, theoretical modelling can be very complicated and prone to many simplifications. However, control and monitoring of feed system temperature and measurement of the mass flow rate of vapour out of the feed system is feasible. With measurements of mass flow rate made at multiple temperatures, the pressure profile and flow regime inside the feed system can be inferred.

4.1.1. Methodology

In order to determine the flow regime inside the iodine feed system, and what the sublimation rate of iodine is as a function of the temperature of the feed system, a small number of tests were conducted. The measurements made in the tests are described in Table 4.1

Table 4.1: Summary of measurements for characterization of the iodine feed system, alongside the intended outcomes and underlying motivation.

Measurement	Outcomes	Motivation
Initial and final mass of iodine, time elapsed	Total mass loss rate of iodine, sublimation rate of iodine, flow regime inside feed system.	RQ-2 and all sub-questions, RQ-1 and all sub-questions, PRO-006.
Temperature of propellant reservoir	Sublimation rate of iodine, pressure inside feed system.	RQ-2 and all sub-questions, RQ-1 and all sub-questions.

The tests consisted of filling a variety of tester feed systems, which have dimensions comparable to the actual feed system designed for the μACFT EM and placing them in a vacuum environment to measure to the rate at which the propellant evaporates and passes through the feed system. By measuring the mass flow rate through a feed line with a known geometry, the pressure profile in the feed system and the flow regime in the feed line can be inferred. Ultimately, by comparing the reservoir pressure to the vapour pressure of iodine, it is possible to assess whether the Langmuir quasi-equilibrium sublimation model or the Hertz-Knudsen vacuum evaporation model is most suitable.

The dimensions of the feed system testers are representative of the dimensions of the actual feed system design, detailed in Section 3.2.2. The feed system design concept simply consists of a large reservoir, a smaller secondary chamber, and a long narrow feed line. Ultimately three different test setups were used, all with a 17 mm diameter reservoir, and varying secondary chamber and narrow feed line diameters and lengths. Copper wire windings and PT100 thermistors were used to increase and monitor the temperature of the reservoirs which were heated.

The reservoirs were filled with approximately 20 g of granular iodine to start the test, and placed in the vacuum chamber with the narrow feed line exposed directly to the vacuum environment. The total mass of the filled reservoirs was recorded and compared to the total mass of the reservoirs after the duration of the test. By recording the exact time that the reservoirs were placed in the chamber and the vacuum pumps were started and the time that they were removed, a first order approximation of the mass flow rate out of the feed system tester can be obtained:

$$\dot{m} \sim \frac{\Delta m}{\Delta t} \tag{4.1}$$

4.1.2. Results

The total duration of the experiments was just under six hours for the heated reservoirs, and just over forty hours for the unheated reservoirs, and the pressure in the vacuum chamber was 3×10^{-7} mbar. The total mass loss was between 5 - 10 g from all the cases tested. The total mass flow rate measured in each of the reservoirs was assumed to be constant throughout the duration of the experiments. By assuming equilibrium between the sublimation rate of the iodine and the mass flow rate through the secondary chamber and narrow feed line, it is possible to calculate the pressure in each stage of the feed system tester. First the pressure in the reservoir stage, which is assumed to be uniform, is calculated using both the Langmuir and Hertz-Knudsen models. The solutions to both equations differ by less than 0.3% in all cases tested. This indicates that the rate of iodine evaporation in the reservoir is simultaneously the maximum possible given the temperature and pressure conditions, and that generation of new vapour particles is nearly in equilibrium with the condensation of vapour particles. Furthermore, the calculated pressure indicates that the reservoir was within 1% of the vapour pressure for iodine at the appropriate temperature (Figure 4.1).

It is important to note that the constants used to determine vapour pressure with the Antoine equation are reportedly only accurate for the range 40 - 180°C [98]. However since no alternative could be found, the constants *A*, *B* and *C* quoted in Section 2.2 are used in all vapour pressure calculations.

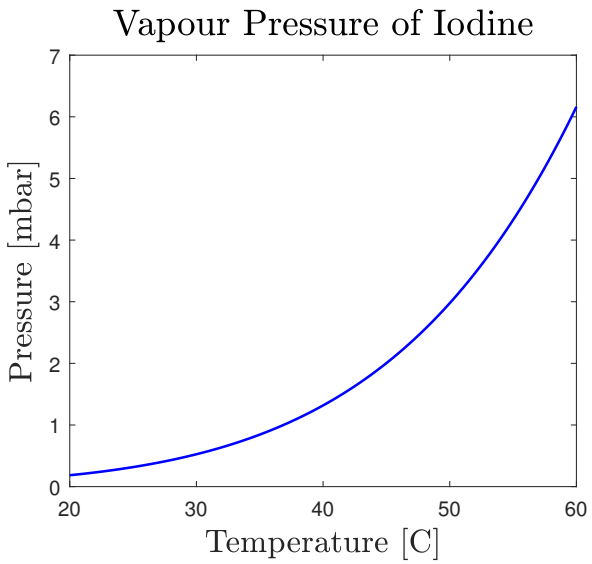

Figure 4.1: Vapour pressure of iodine in temperature range 20 - 60°C. This pressure is nearly equal to the pressure inside the propellant reservoir during testing.

The pressures in the later stages of the feed system testers are calculated using both the equations for laminar flow and for free molecular flow. In doing so, two results for the pressure inside the secondary chamber and narrow feed line were generated for each of the cases tested. However, based on the laminar flow model, positive pressures (> 1 bar) are found, which is implausible based on the surrounding vacuum environment. Thus the results obtained with the free molecular model are used in further analysis.

Figures 4.2 and 4.3 summarize the results of the mass flow rate tests conducted. Shown in the each plot is a quarter section view of the feed system geometry used in the test. Each 'x' indicates the pressure in that section of the feed system which was calculated. In all cases where a second chamber exists, the pressure inside the feed system is minimum at this point. A smooth spline interpolation is included as visual reference for the relative difference in pressures and gradients in the system. The vapour pressure of iodine in the reservoir is also noted, as is the ambient pressure of the vacuum environment that the feed system is surrounded by.

Due to the magnitude of the pressure gradients inside the feed system, there should be a plume with a size on the order of 10 - 20 mm at the outlet. This is assuming that the pressure gradient across the plume is larger than the internal gradients so that vapour is forced to exit the system and not circulate. This plume is a key reason why a pressure differential of multiple orders of magnitude can exist between the feedlines and the surrounding atmosphere environment.

Assuming that the mass flow rate through the feed system was equal at all stages, the pressure is a minimum in the secondary chamber. For this to be the case, the pressure in the narrow feedline must be relieved before more propellant can move forward into this stage, after which the pressure in the narrow feedline rises again. This barrier helps to explain how the pressure in the reservoir can build up to the vapour pressure of the reservoir. Furthermore, this process would result in the propellant vapour puffing out of the exit of the feed system.

The Knudsen number was calculated based on the dimensions of the feed system and the pressures derived from the free molecular flow equation. In the feed system experiments, Kn lies within the range 0.004 - 1.1 across all the feed system stages, indicating that the flow is actually in the transitional regime between laminar and free molecular flow. Generally Kn is lowest in the reservoir, where the pressure is high. In this stage, Kn is in the range 0.04 - 0.2, where Kn falls as the temperature rises. In the secondary chamber, Kn is in the range 0.2 - 1.1, where the lower Kn again corresponds to the higher temperature. Finally, in the long and narrow feedline, Kn falls in the range of 0.02 - 0.2, with the same temperature dependence. Although overall the feed system is in the transitional flow regime, Kn suggests that the flow is closer to laminar in the reservoir and the narrow feedline, but closer to the free molecular limit in the secondary chamber.

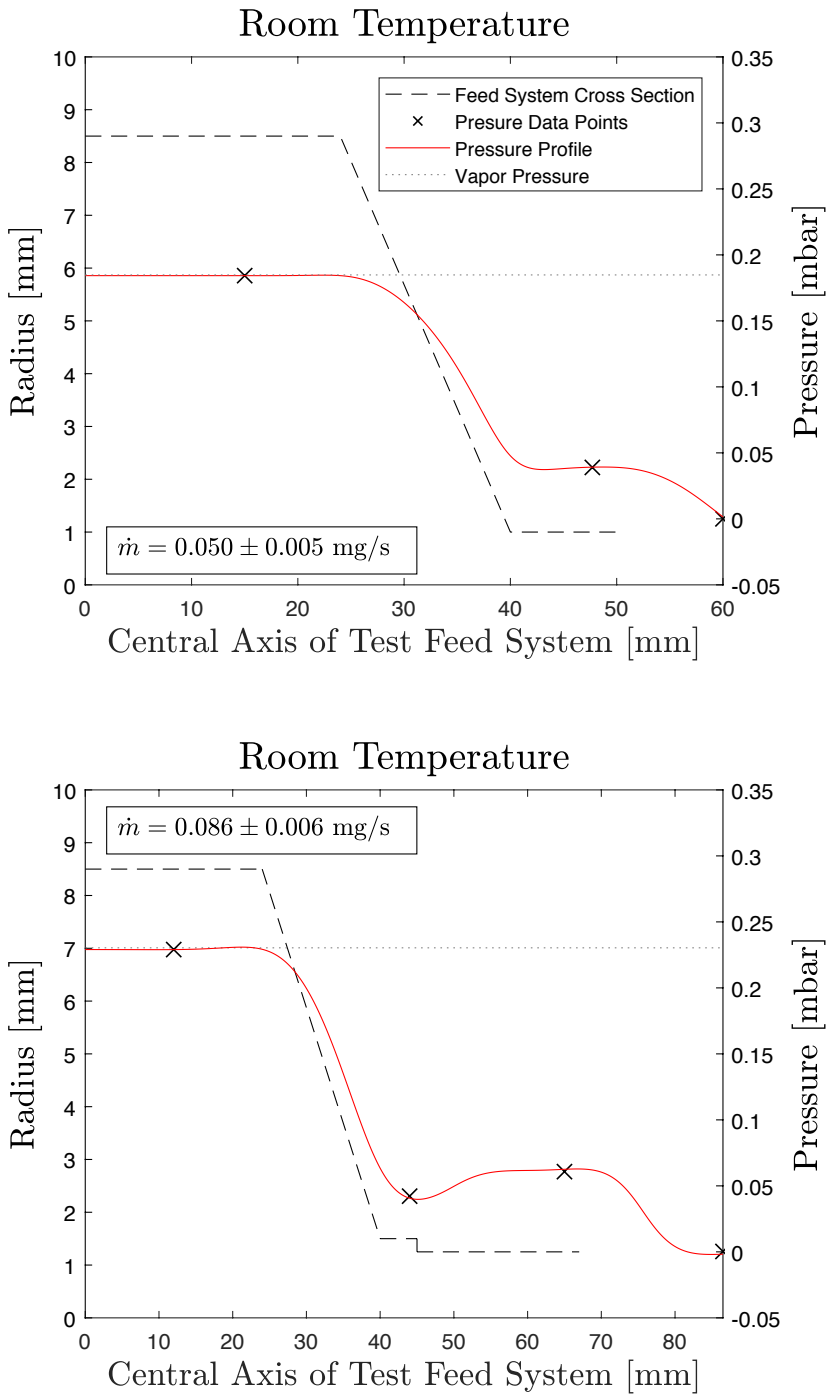

Figure 4.2: Interpolation of pressure profile inside room temperature to-scale feed system model, based on the measured mass flow rate of iodine into the vacuum surroundings at 3×10^{-7} mbar. The pressure inside the propellant reservoir (left side) is near the vapour pressure of iodine, the secondary chambers are at the lowest pressure. A plume of 10 - 20 mm maintains the higher pressures of the feed system.

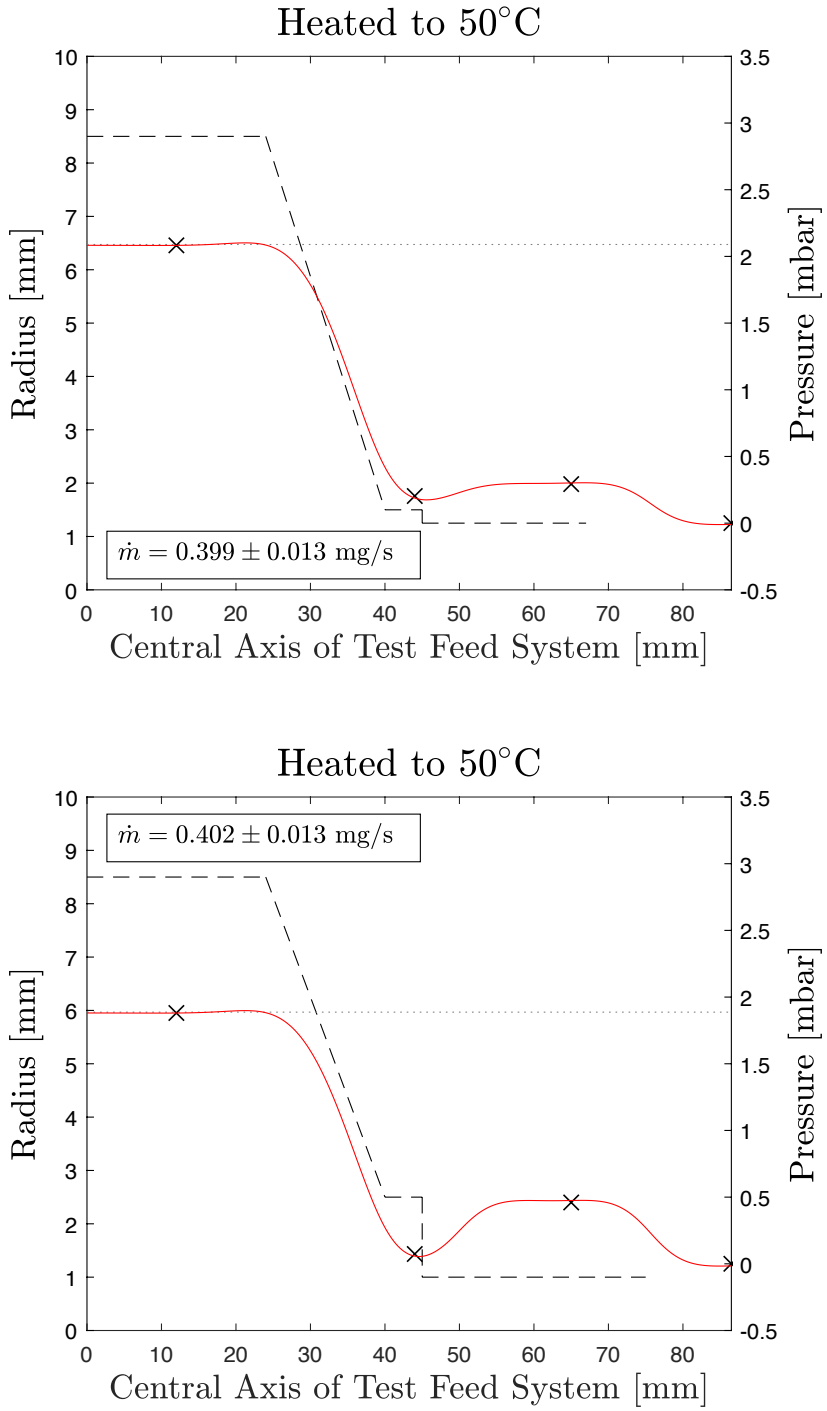

Figure 4.3: Interpolation of pressure profile inside heated to-scale feed system model, based on the measured mass flow rate of iodine into the vacuum surroundings at 3×10^{-7} mbar. The pressure inside the propellant reservoir (left side) is near the vapour pressure of iodine, the secondary chambers are at the lowest pressure. A plume of 10 - 20 mm maintains the higher pressures of the feed system.

4.2. Mass Flow Rate

A key insight from the feed system tests described in Section 4.1 is that the pressure in the propellant reservoir is nearly equal to the vapour pressure of iodine. Another key observation is that the flow occurs in the transitional regime between laminar and free molecular flow. However, the flow tends toward laminar in the propellant reservoir and narrow feedline, while it is closer to the free molecular limit in the secondary chamber of the feed system. Combining these observations with the dimensions of the actual μACFT feed system leads to a model for estimating the mass flow rate through the thruster.

The propellant flow rate is calculated by modelling the feed system in the same three stages that were represented in the tests. The first stage is the propellant reservoir, which is assumed to be at the vapour pressure of iodine P_{vap}. In reality, the reservoir and secondary chamber are separated by an orifice with area A_o, where the mass flow rate through this orifice is described by Equation 2.29. The secondary chamber is defined by a diameter d, and the mass flow through this stage is assumed to be in the free molecular limit. The third stage is the narrow feedline which in reality is the anode of the thruster. The flow through this stage is assumed to be laminar, where the pressure gradient across the channel is given by the difference in pressure between the secondary chamber and the surrounding vacuum environment. This is a key difference in comparison to the analysis in Section 4.1, where the pressure gradient occurs outside the end narrow feedline and not inside. With fixed feed system dimensions, the only free parameter is the temperature of the reservoir. Therefore the flow rate can be solved for as a function of temperature.

The mass flow rate through this simplified feed system model is assumed to be the same at all stages. The pressure in the secondary chamber, P_2, is calculated as the positive solution to Equation 4.2

$$P_2^2\left(\frac{\pi M_{kg} d^4}{32 k_B T}\right) + P_2\left(\frac{2C_v^2 A_o^2 M_{amu} P_{vap}}{RT}\right) - \frac{2C_v^2 A^2 M_{amu} P_{vap}^2}{RT} = 0 \tag{4.2}$$

where M_{amu} is the molecular mass of iodine in units amu or grams per mol, and M_{kg} is the mass of an iodine molecule in kilograms. This quadratic equation is derived by equating the relationships for the mass flow through the orifice (Equation 2.29) and the free molecular flow through the secondary chamber (Equation 2.25), using the width of the chamber as d. The solution found for P_2 is then used to calculate the mass flow rate through the anode using Equation 2.26, where $\Delta P = P_2 - P_{vac}$. The solution to Equation 4.2 and Equation 2.26 is shown for various orifice diameters in Figure 4.4. For the calculation, the 2 mm inner diameter of the anode is taken as the feedline diameter.

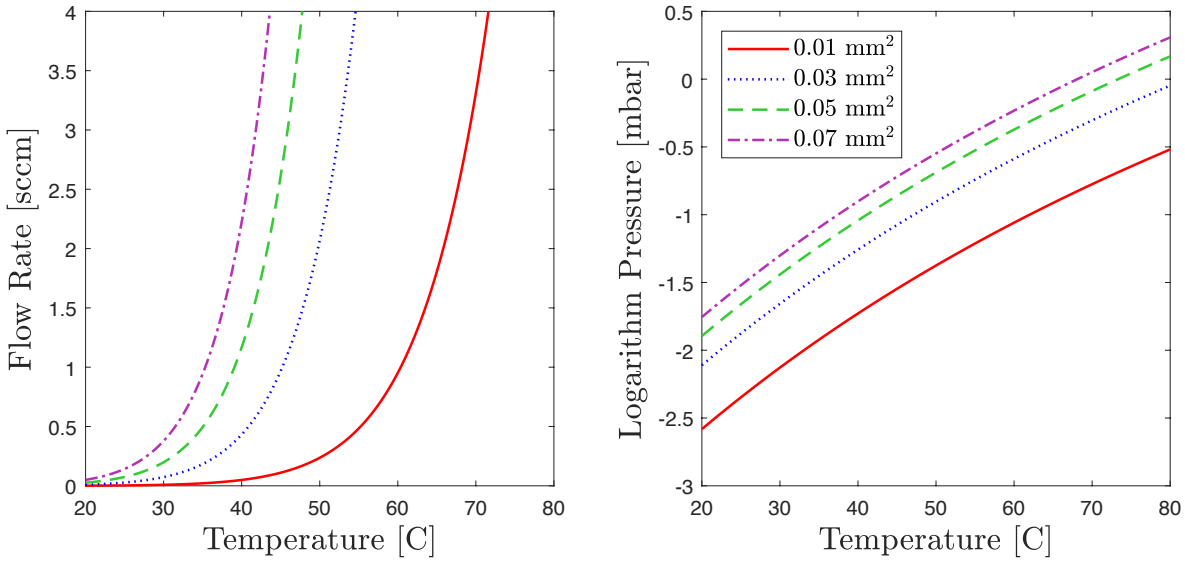

Figure 4.4: Volumetric flow rate through feed system and pressure in second stage chamber for various orifice diameters, based on the three stage feed system model. The flow between the propellant chamber is at the vapour pressure of iodine, and flow to the secondary chamber is controlled by the orifice while the flow through the anode is laminar. The pressure in the secondary chamber is calculated assuming a free molecular flow.

4.3. Discussion and Conclusion

In this chapter, characterization of the iodine μACFT feed system with respect to flow regime and mass flow rate is investigated. Since both aspects of the feed system fluidics rely upon correctly estimating the sublimation rate of solid iodine, the suitability of using the Langmuir quasi-equilibrium sublimation model is first assessed.

A small series of experiments were conducted. The tests consisted of placing four iodine filled reservoirs, with dimensions comparable to the μACFT feed system, inside the vacuum chamber at the LET test facility. The test feed systems consist of three stages: propellant reservoir, secondary chamber and a narrow feedline. The total mass of the reservoirs are measured before and after the going into the chamber in order to estimate the mass flow rate of iodine out of the reservoir. By assuming an equal mass flow through each section of the test reservoirs, a pressure profile could be calculated using the equation for free molecular flow. Two tester reservoirs were heated to 50°C and the others were left at room temperature. In each of the cases tested, the pressure in the reservoir was calculated to be in the range of 99.6 - 99.8% of P_{vap}, while in the feedline the pressure is lower, and in the secondary chamber the pressure is minimum. Calculating the Knudsen number in each region reveals that on average, the entire feed system is in the transition regime between free molecular and laminar flow. However, inside the reservoir and feedline, the flow is closer to laminar, while in the secondary chamber, it is closer to free molecular flow.

The magnitude of the measured mass flow rates at room temperature (0.050 and 0.086 mg/s, corresponding to 0.265 and 0.456 sccm) is comparable to the typical mass flow rate used to ignite and run the μACFT system with xenon. However, the heated test reservoirs generated mass flow rates much higher, approximately 2.1 sccm. This mass flow is higher than what is necessary to ignite the μACFT according to tests conducted with the current and previous μACFT systems. Furthermore, it was noted that it would be possible to operate the thruster at temperatures much lower than the initial design objective of 100°C, since the mass flow rate near room temperature was already sufficient for the μACFT. In practice this observation could be incorporated into the feed system design to reduce the overall power required for heating the device, and simultaneously reduce the burden of excess waste heat in the CubeSat design.

A model of the μACFT feed system is created using the observations regarding flow regime gathered from the tests. The model is based on the three stages of the feed system. The pressure inside the reservoir is assumed to be equal to P_{vap}, and vapour flow between the reservoir and secondary chamber is determined by the cross-sectional area of the orifice. In the secondary chamber, the flow is assumed to be the free molecular limit, while in the anode the flow is assumed to be laminar. Under the assumption that the mass flow rate through each stage of the feed system is equal, the pressure inside the secondary chamber and the overall mass flow rate are calculated.

This model is only an approximation of the actual behaviour of the feed system since it is based on simple equations for laminar and free molecular flow through a pipe, when in reality the feed system is in the transitional regime. Furthermore, the geometry of the secondary chamber is overly simplified and gradients in temperature are not considered. The pressure inside the discharge chamber is also not taken into account, and the gradient across the narrow anode feedline leading into the discharge chamber is assumed to be $\Delta P = P_2 - P_{vac}$. Nonetheless, the model shows that the mass flow rate grows exponentially with temperature. In order to restrict the mass flow to the range where standard operating points are achieved (0.2 - 0.4 sccm), the feed system must either be operated at lower temperatures, or the orifice must become smaller. However as noted in Section 3.3.2, a high temperature is required to maintain high pressure and avoid backfiring. Therefore a redesign of the feed system orifice may be necessary. Both reducing the orifice to the micro-scale and relocating it to the interface between the secondary chamber and the anode could resolve the issue.

5

Resonant DC/DC Converter

The μACFT CubeSat EM is a miniature, low power device which must generate a high voltage for the anode of the thruster with only a 12 V input line. For this purpose a high gain, and low power DC/DC converter is required. This specific combination of attributes is rather niche, and thus design of the converter is favourable to a general purpose COTS option which would not perform optimally.

Commonly used converter topologies used in modular device applications include flyback or buck-boost, two-switch forward, push-pull, and resonant. Due to the characteristically higher efficiency the resonant converter (upwards of 90% in many cases [63, 97, 117]), it is a favoured DC/DC converter topology where power is limited and thus very high efficiency is desired.

In this chapter, the design of an LLC resonant DC/DC converter for the μACFT is described. The results of simulating and testing the device in hardware form are presented. Ultimately, results from the tests, as well as observation and analysis of the LLC converter concept are used to assess the suitability of a simple LLC resonant converter for applications in which a large gain is required to produce a large voltage for a low power load.

5.1. Converter Design

The design methodology used to develop the LLC converter for the μACFT CubeSat EM is outlined in Figure 2.5. From the design flow shown and the equations of the FHA approach, one can see that the key design parameters are the nominal input and output voltages V_{in} and V_{out}, the converter load impedance R_L, and the resonant tank elements L_r, L_m, and C_r. It is noted that different transformer turn ratios are necessary for a full bridge or half bridge converter design. Additional, the equation used for total converter gain, G, differs with these cases as well.

The design methodology in Figure 2.5 was consulted as a framework for designing a DC/DC converter for the μACFT, however some deviations were made in selection of the Q factor, and determining the magnetizing inductance L_m. The reasons are detailed as the design steps are encountered in the discussion. The requirements for the power processing unit are:

PWR-001: The thruster shall be compliant with the PC/104 standard.

PWR-002: The power converter shall provide up to 10 W of power.

PWR-003: The thruster shall operate on a 12 V regulated, or unregulated, input voltage.

PWR-004: The power converter shall provide up to 1.5 kV controllable output voltage.

The first three requirements arise due to the intended CubeSat application, whereas the final requirement is based on cold-starts demonstrated with previous μACFT engineering and laboratory models. Based on the previously demonstrated operating points of the μACFT, it was decided that the nominal output voltage of the converter should be 1200 V [41, 91]. The selection of this nominal output voltage also includes a conservative margin such that in the case that the designed gain cannot be achieved in practice, the thruster may still reach lower operating voltages (400 - 1200 V) [91].

Simple graphical trade offs for the resonant converter switching regulator scheme and the resonant tank topology are shown in Tables 5.1 and 5.2. All criteria in the trade offs have equal weighting and the design options are evaluated as having a positive, neutral, or negative inclination toward the criteria. Green indicates that the design option is well suited with respect to a given criteria, yellow indicates a neutral compatibility, and red indicates a poor compatibility.

All components are assumed to be space-grade, implying that costs could be high. For this reason cost is a criteria in both trade offs. For the switching regulator trade off, the suitability for the low power and high gain application are the other criteria. For the resonant tank, the sensitivity to changes in load and energy storage are considered. The converter should be isolated from changes in the load, which will vary with the voltage and the current of the anode. Furthermore, reduced circulating energy is preferable for reduced EMI and better power transfer.

Table 5.1: Graphical trade off for resonant converter switching regulator scheme.

	Cost	**Low Power Suitability**	**Gain**
Half Bridge	Two transistors required.	Intended for low power applications.	Offers half the gain of full bridge.
Full Bridge	Four transistors required.	Intended for higher power applications.	Offers twice the gain of half bridge.

A half bridge switching regulator topology is selected since it is suitable for a low power application, and the cost is generally lower. However, the main drawback of the half bridge relative to the full bridge is gain.

Table 5.2: Graphical trade off for resonant converter switching regulator scheme.

	Cost	**Sensitivity to Load**	**Energy Storage**
Series	Two components required.	Sensitive to changes in load.	Moderate energy storage in resonant tank.
Parallel	Two components required.	Sensitive to changes in load.	Moderate energy storage in resonant tank.
Series-Parallel	Three components required.	Isolation from changes in load.	Low energy storage in resonant tank.

The series parallel resonant tank design was chosen due to the lower circulating energy leading to reduce waste energy, and reduced sensitivity to load change offered by the series-parallel tank [118]. The additional cost of an LLC resonant tank is outweighed by these attributes.

In order to transform an inverted 12 V signal (6 V peak-to-peak) into a 1200 V DC signal, a transformer with a turns ratio of $n = 200$ is required (Equation 2.31). Based on requirement PWR-003 identifying the possibility of an unregulated input voltage bus, an uncertainty in input voltage of ±2 V is assumed to determine the minimum and maximum input voltages. This leads to minimum and maximum gain requirements of $M_{g,min} = 0.71$ and $M_{g,max} = 1.50$ which correspond to a frequency range of $0.82 < \frac{f_{sw}}{f_{r,1}} < 1.48$. Selection of the inductance ratio L_n was influenced by availability of components for PCB manufacturing, and the magnetizing inductance of available transformers, since COTS components were used in the design.

A resonating inductance $L_r = 1.0 \pm 0.1$ µH was chosen to compliment the measured magnetizing inductance $L_m = 1.4 \pm 0.1$ µH of the transformer. The value of L_m was not selected freely as designing a transformer is necessary to achieve desired magnetizing inductance but instead a COTS option was selected. Figure 5.1 shows the gain curves for an LLC resonant converter with $L_n = 1.4$, for a range of Q factors. The vertical lines show the locations of $f_{r,1}$ and $f_{r,2}$, while the horizontal lines show the levels of $M_{g,min}$ and $M_{g,max}$. As Q increases, the peak of the gain curve moves toward $f_{r,1}$, and as Q decreases it moves toward $f_{r,2}$. A Q factor of $Q \leq 0.86$ is required to ensure both $M_{g,max}$ and $M_{g,min}$ could be achieved. Establishing a range of acceptable Q factors to select from effectively allows the designer to complete the process decision loop in Figure 2.5 in two steps.

The equations for Q and R_e (Equations 2.37 and 2.36)) are then considered to determine what AC impedance is seen by the resonant tank during operations, and what Q factor be realistically chosen based on the loading conditions. Based on the maximum power requirement of 10 W, and the output voltage range of 1000 to 1500 V, the load resistance presented by the μACFT anode should be in the range of $100 < R_L < 225$ kΩ (or larger for less power consumption). Since Q is inversely proportional to $n^2 R_L$, which has an order of magnitude of 10^9, the Q factor is much less than one. For practical design purposes, the Q factor of this converter is equal to zero. This indicates that the resonant tank sees an open circuit at it's output.

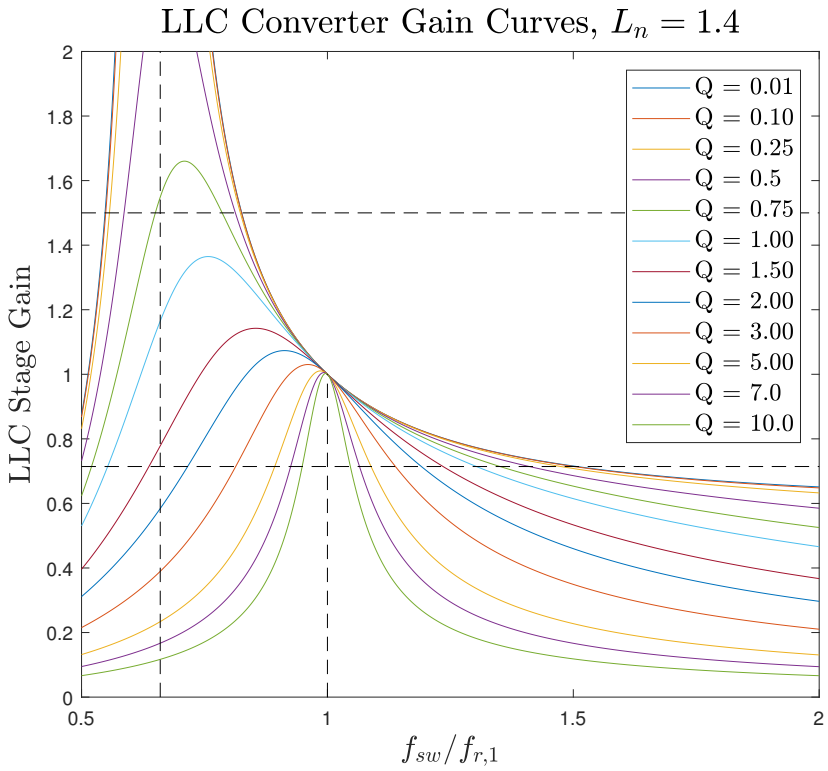

Figure 5.1: Gain curves of L_n = 1.4 LLC resonant DC/DC converter for various Q factors. Noted are the resonant frequencies $f_{r,1}$ and $f_{r,2}$, and the minimum and maximum required gain of the converter, $M_{g,min}$ and $M_{g,max}$. For the μACFT converter, $Q \ll 1$ and the gain curve is nearly identical to the Q = 0.01 curve shown. Therefore the frequency operating range ($0.82 f_r$ - $1.48 f_r$) is the span on the horizontal axis between the intersections of the outermost Q curve with $M_{g,max}$ and $M_{g,min}$.

The final step in the circuit design is acknowledging the need for split resonant capacitors at the primary side of the transformer. These two capacitors connect the V_{in} line and ground, with the mutual node connected to the transformer [97]. With this simple network, the signal in the transformer is isolated from the DC ground, which would drain the circulating energy. However the second capacitor connecting the transformer to ground will introduce additional LC resonance frequencies.

5.2. Simulation and Hardware Testing Activities

Table 5.3 shows the components selected for each element of the half bridge LLC converter design. Development of the converter proceeds from a low voltage breadboard to a high voltage PCB. Both circuit designs are simulated in Multisim to estimate the power and gain characteristics of the design. The measurements conducted during the development are summarized in Table 5.4.

Table 5.3: Hardware overview of DC/DC converter.

Element	Description	Component	Relevant Specifications
Pulse Wave Modulation	Resonant mode controller which offers two alternating PWM output channels with programmable frequency and dead-time as well as soft start feature.	TI UC25600	• Generates pulses up to 22 V in amplitude. • Switching frequencies between 40 kHz and 350 kHz. • Low power consumption.
Switching Regulator	GaN half bridge switching regulator power stage.	TI LMG5200	• 80 V signal rating. • 10 A throughput current rating. • Low power consumption.
Resonant Tank	Surface mount inductor and capacitor	0603 SMD package 1 µH, 440 nF and 200 nF	• 30 V signal rating.
Transformer	1:200 coil miniature surface mount current transformer.	TDK B82801B0925A200	• Voltage-time product 100 Vµs. • 0.6 mΩ primary side and 33.2 Ω secondary side resistance. • Magnetizing inductance 1.4 µH (measured).
Rectifier	High voltage ultra fast surface mount rectifying diodes.	BYG23T	• 1300 V signal rating. • 1.0 A throughout current rating (average). • 75 ns reverse recovery time.

Table 5.4: Summary of DC/DC converter measurements, alongside the intended outcomes and underlying motivation.

Measurement	Outcomes	Motivation
Power input and output	Power consumption and conversion efficiency, comparison to simulation.	RQ-3, PWR-002.
Voltage output	Voltage gain, frequency response of converter, comparison to simulation.	RQ-3, PWR-004.
Switching frequency	Frequency response of converter.	RQ-3.

5.2.1. Low Voltage Breadboard

As a first step, the design concept is implemented on a breadboard setup with a smaller transformer (n = 5) to confirm that the components function together as expected, and to determine whether a high power efficiency could be achieved with the proposed design.

For the breadboard, an $n = 5$ transformer and standard BAT54 30 V Schottky diodes are used with the UCC25600 PWM controller and LMG5200 GaN half bridge, switching at 100 kHz. Ideally 30 V output is produced from a 12 V input with this circuit. The key features of the lower voltage breadboard converter are summarized below.

$V_{out} = 30$ V $\qquad L_r = 40$ nH

$n = 5$ $\qquad L_m = 1.00$ µH

$f_{sw} = 100$ kHz $\qquad C_r = 2.54$ µF

Simulation The lower voltage breadboard circuit was simulated in Multisim (Figure 5.2) to verify the design and to compare with the experimental efficiency measurements. The UCC25600 PWM controller is represented by switches which have are set to alternate at 100 kHz with a dead time between pulses of 0.15 µs for a 47.5% duty cycle. The LMG5200 half bridge power stage is represented by two 2SK2980 high speed power switching MOSFETs as a SPICE model representation of the device was not available.

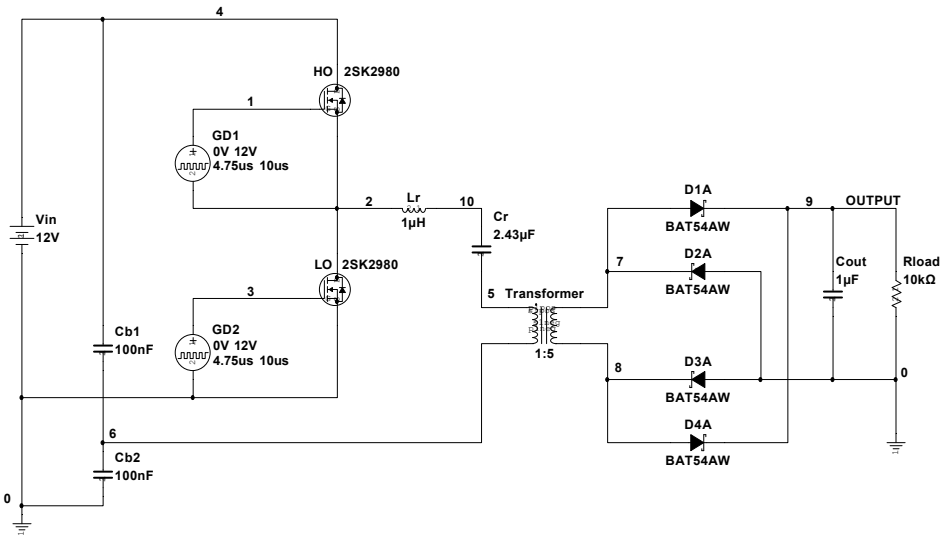

Figure 5.2: Multisim circuit simulation of 30 V LLC DC/DC converter breadboard.

Breadboard The switching mechanism of the PWM controller can be easily tuned between 50 to 250 kHz using a potentiometer connected to RT pin of the UCC25600. Similarly the dead time between pulses can be tuned with a potentiometer on the DT pin. Datasheet recommendations are taken into account when determining what value of capacitor or resistor is appropriate for the VCC pins of the LMG5200 and UCC25600. A 1 µF capacitor is used to create an RC low pass filter with a low cutoff frequency at the output.

This circuit is tested at $f_{sw} = f_r$, where the gain of the resonant tank is unity. The output voltage and power throughput, measured across a range of loads from 50 Ω to 10 kΩ, are shown in Figure 5.3. The output voltage of the converter is stable and greater than 29 V for any load larger than 3 kΩ. The power efficiency of the converter varies across this range of loads, peaking at 77% near 1 kΩ load. The actual power throughput of the converter never exceeds 2 W. The Multisim simulation is used to calculate the the power throughput and conversion efficiency of the design, and the results are also shown in Figure 5.3. At lower load resistances, the power throughput predicted by the simulation grows while in the breadboard circuit it fell off. This may be due to a power limitation of the potentiometer used to vary the load resistance, or a particularity of one of the circuit components which was not implemented in the simulation. Aside from this particular region of the test domain, the experimental measurements and simulation predictions appear to be in agreement, particularly for the power conversion efficiency of the device. This agreement is taken as confirmation that the representation of the PWM controller with switches and half bridge power stage with 2SK2980 transistors in the simulation is adequate.

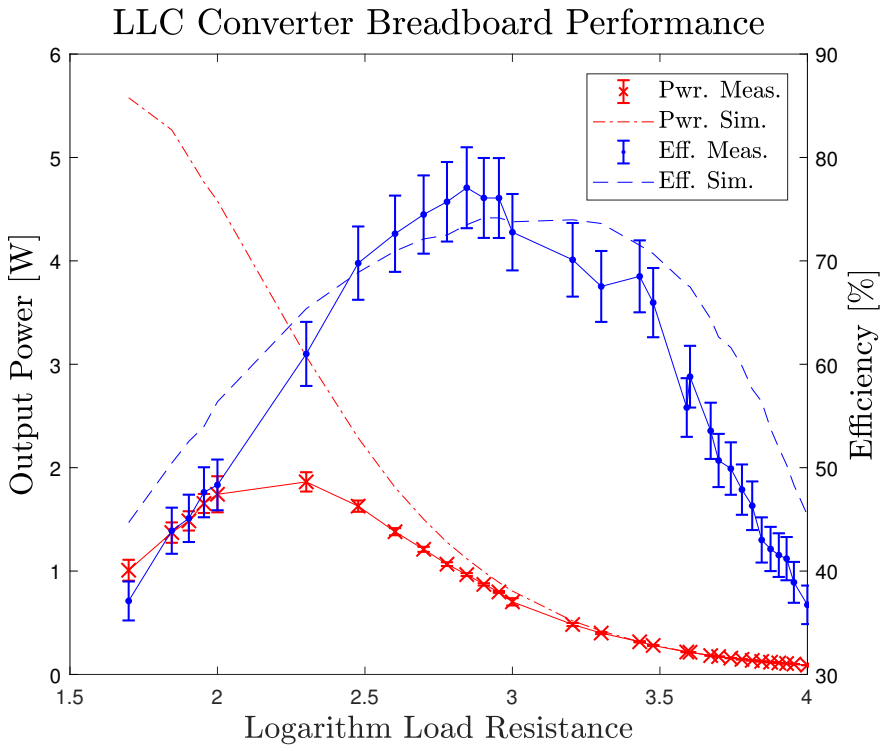

Figure 5.3: Comparison of results from Multisim simulations and breadboard hardware performance of LLC resonant DC/DC converter design. Peak efficiency measured is 77%, and efficiency curve agrees with simulation. Measured power output is below 2 W.

Although the breadboard efficiency peaks at only 77%, limiting parasitic and non-ideal effects in the breadboard circuit by transferring the design onto a PCB should improve the efficiency overall.

5.2.2. High Voltage Circuit Board

The design of the high voltage PCB is very similar to the breadboard, with a few key distinctions. The modifications to the breadboard design include replacing the transformer with one which provides the necessary turns ratio ($n = 200$), replacing the diodes and output filter capacitor with components which can withstand the high voltage, and adjusting the resonant and switching frequencies of the circuit to account for the voltage-time product of the transformer.

The features of the high voltage converter circuit are summarized below.

$V_{out} = 1200$ V $\qquad L_r = 1.08\,\mu$H

$n = 200$ $\qquad L_m = 1.40\,\mu$H

$f_{sw} = 200$ kHz $\qquad C_r = 606$ nF

Simulation The Multisim simulation of the high voltage converter design is shown in Figure 5.4, where the UCC25600 PWM controller and LMG5200 half bridge converter stage are represented the same way as in the previous simulation. The dead time of the switches is 0.11 µs for a 47% duty cycle. A custom Multisim component is created to represent the BYG23T switching diodes in the rectifier. This custom component is assigned the voltage rating, current limit, and reverse recovery time of the actual diode. Furthermore, the transformer model is customized to account for the primary and secondary side resistances and the magnetizing inductance of the actual component. However, the one feature of the transformer not represented in the Multisim component designer is the voltage-time product.

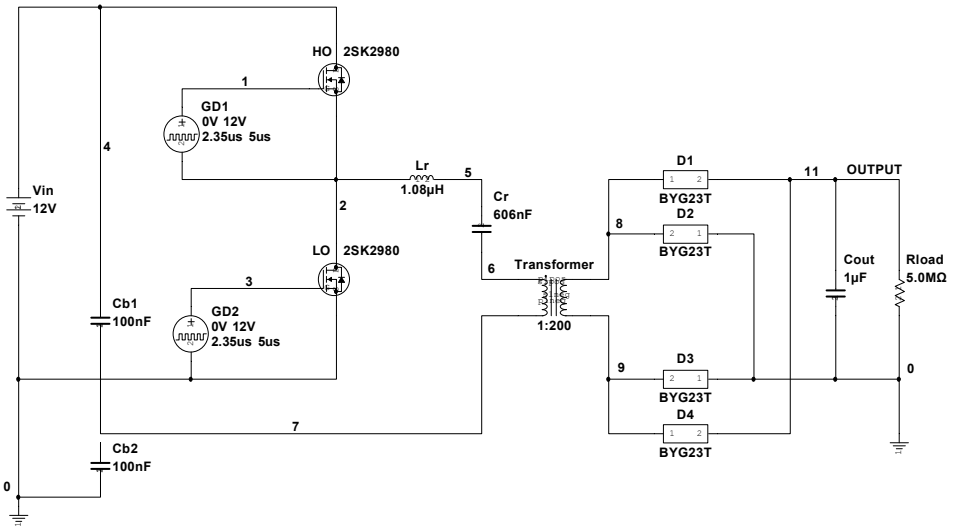

Figure 5.4: Multisim circuit simulation of LLC DC/DC converter printed circuit board.

During investigations with this Multisim circuit, it became apparent that the power conversion efficiency of the circuit at nominal gain had decreased relative to the low voltage design. For a load on the order of 200 kΩ, which is the expected load presented by the anode of the µACFT, the maximum power conversion efficiency which could be achieved is 53%. Both increasing and decreasing the output load from this point results in a decrease in efficiency.

Printed Circuit Board The converter PCB design is created in Eagle. The schematic diagram and routing diagram for the circuit can be seen in Figures B.4 and B.5 respectively in Appendix B. The PCB requires 12 V, 5 V and GND connections, as well as one high voltage output for the anode. However due to the small footprint of the circuit, a board with only one half of the total PC/104 area is used. Furthermore, the 104 pin structure is not used. The fully assembled circuit board can be seen in Figure 5.5.

The output voltage range and power efficiency of the converter are measured by varying the switching frequency and output load, respectively. The measured gain curves of the converter are shown in Figure 5.6, plotted versus the theoretical gain curve based on Equation 2.38. Ultimately, the converter did not achieve the expected gain. The maximum gain measured with the converter was $G = 65$, for an output voltage of $V_{out} = 780$ V. When driven at the resonant frequency of the circuit, the gain of the converter was half of the designed value, achieving 600 V output.

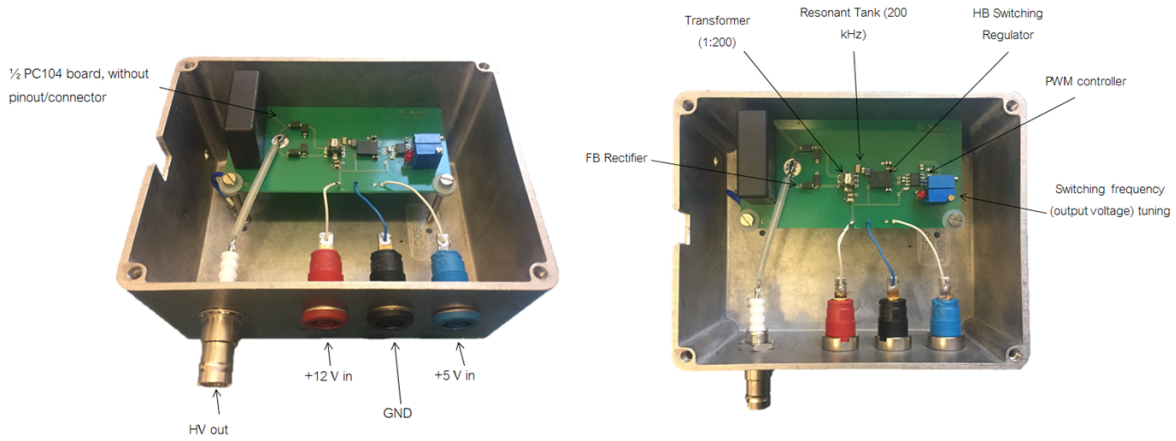

Figure 5.5: LLC resonant DC/DC converter PCB for the μACFT EM, inside grounded housing for safety.

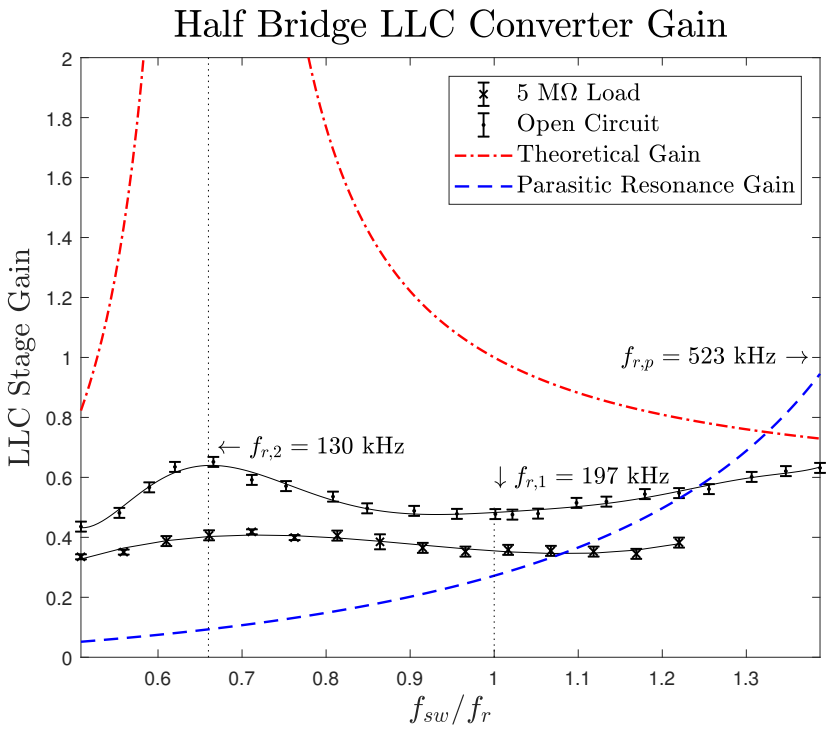

Figure 5.6: Open circuit and loaded gain curves of DC/DC converter PCB. Noted are the theoretical gain curves of the designed LLC converter using fundamental harmonic analysis based on $f_{r,1}$ and $f_{r,2}$, and the effect of the $f_{r,p}$ resonance with the split resonant capacitors.

Noted on the plot are resonant frequencies $f_{r,1}$ and $f_{r,2}$, and a third resonant frequency $f_{r,p}$. The first two resonances refer to those generated by the resonant tank (Equations 2.32 and 2.34), while the third is a resonant frequency associated with the LLC resonant tank components resonating with one of the 100 nF split-resonant capacitors ($C_{s/r}$) used to isolate the transformer from ground.

$$f_{r,p} = \frac{1}{2\pi\sqrt{L_r(C_r^{-1} + C_{s/r}^{-1})^{-1}}} \tag{5.1}$$

Despite the fact that the parasitic resonance is more than 2.5 times higher than the resonant frequency of the LLC circuit, it's influence on the gain of the circuit is not negligible. As shown in Figure 5.6, the gain of the converter continues to climb when $f_{sw} > f_{r,1}$, which is the opposite of the typical behaviour of an LLC converter. In theory, $f_{r,p}$ could be increased, reducing its influence on the gain curve of the converter, by using smaller capacitors for isolating the transformer. However in practice, capacitors smaller than 100 nF led to much weaker isolation and a complete loss of energy coupling into the transformer.

The power conversion efficiency of the converter was tested using a small variety of loads with suitable power ratings. The results are shown in Table 5.5. The agreement between the simulated and measured efficiencies is not as close it is for the low voltage breadboard. However a similar trend in power conversion efficiency as a function of load appears. As the load increases, the simulated and measured efficiencies converge, which is also observed in the breadboard tests. The measurements and simulations indicated that a peak efficiency greater than 15.7% could be achieved at 200 kΩ.

Table 5.5: Gain and efficiency of DC/DC converter with various loads. No power transferred at open circuit (O/C) and so no power efficiency available. Peak simulated efficiency occurs at $R_L = 200\ \text{k}\Omega$ load, but this load has not been bench-top tested.

Load	Measured Gain	Simulated Gain	Measured Efficiency	Simulated Efficiency
O/C	65.0	108.2	N/A	N/A
5 MΩ	35.8	108.2	2.8%	2.3%
1 MΩ	36.6	108.3	9.5%	11.5%
96 kΩ	15.8	50.0	15.7%	36.3%
200 kΩ	N/A	108.3	N/A	53.1%

5.3. Discussion and Conclusion

In this chapter, the design for a low power, high voltage gain resonant LLC DC/DC converter is described with the intention of developing a PC/104 compliant power processing unit for the μACFT device. The driving factors for the design of the converter are the PWR requirements of the μACFT CubeSat EM. The compliance two the PC/104 standard implied a 12 V or 5 V input. The μACFT requires an anode potential on the order of 1 kV. The necessity for a low power consumption ultimately lead to the selection of the resonant LLC converter topology, due to it's characteristically high efficiency. Thus the development of the power processing unit is dependant on what performance can be achieved with an LLC converter in the context of a high voltage gain but low power consumption application.

The converter is designed to transform a 12 V input voltage into a variable 1000 - 1500 V output voltage. The converter is composed of COTS integrated circuits and surface mount components. The circuit design is simulated in Multisim, as well as tested on a low voltage breadboard and a high voltage printed circuit board. Comparison of measurements made with the breadboard circuit validate the design and show that the selected components work together as expected. Furthermore, the Multisim simulation of the design produces results which are in agreement with the breadboard measurements, except in the case of the power output of the converter for small loads. The gain of the breadboard at the resonant frequency of the converter is equal to the gain predicted by the FHA model for an LLC circuit. The maximum measured power conversion efficiency of the breadboard device is 77%, and the maximum power output is 1.9 W. The final high voltage PCB implementation of the converter meets only the power processing unit requirement for input voltage (PWR-001), but not the others and thus it was not used in testing of the μACFT EM.

The performance of the converter is much lower than anticipated in a few key ways. Firstly the maximum gain measurement $G = 65.0$, achieved with an open circuit output, is approximately half the required maximum gain of $G = 150$ (violating PWR-004) and still much less than the minimum gain of $G = 83.3$. When adding a load to the output, the gain decreases significantly. Although the power consumption of the device is very low (< 2.4 W), the measured power conversion efficiency is also very low, and the measured power output of the device never exceeds 0.4 W (violating PWR-002). Ultimately the converter was not used in the testing the μACFT due to the inadequate performance.

Three issues can be identified with the design concept for the LLC converter described in this thesis which lead to lower performance relative to a typical LLC converter. Ultimately, all the points are related to the characteristics of the transformer and the simultaneous requirements on high voltage gain and low power consumption.

Restricted Design Space The design space of the LLC converter is limited in the case that both a high voltage gain and low power consumption are required. This is a result of the fact that a very high turns ratio is required to produce the very large voltage gain, and that the low power consumption at the output implies a large load resistance. By combining Equations 2.36 and 2.37, one can see that $Q \propto \frac{1}{n^2 R_L}$. The Q factor of the LLC circuit is constrained to $Q \ll 1$ when $n^2 \gg 1$. Another factor limiting the choice of Q is the low power requirement. For a high output voltage implies a large output load R_L, and thus a further decrease of Q. In the case presented in this thesis, $Q \sim 10^{-9}$. The only way to counteract this restriction on Q is by increasing the L_r/C_r ratio by multiple (approximately eighteen) orders of magnitude. However this is not practical since C_r would need to so small that the capacitance becomes negligible in comparison to parasitic effects.

The effect of having a restricted design space with respect to the Q factor does not make the design impossible. Several LLC designs with $Q \ll 1$ can be achieved simply by tuning the inductance ratio L_n, such as the one presented in this thesis. However Q is typically a free design parameter in LLC converter design which allows for the designer to select a gain curve which best suits the specific requirements of the converter. However in the specific case where high voltage gain and low power consumption are required, Q is not a free design parameter since all gain curves for $Q < 0.1$ are effectively identical (Figure 5.1).

Limited Gain The gain of the converter appears to be restricted by the voltage-time product of the transformer. The voltage-time product, $V_{\mu s}$ is a measure of the energy density that the transformer is capable of transferring in each half period of the signal. It is typically measured in units of Vμs and is described by Equation 5.2

$$V_{\mu s} = V\frac{T}{2} \tag{5.2}$$

where V is the peak voltage in the transformer and T is the period of the AC signal. For the converter design demonstrated in this thesis, the product on the right-hand side of the equation is 30 Vμs at the transformer primary side, and 3000 Vμs at the secondary side. However the datasheet for the transformer chosen quotes a voltage-time product of 100 Vμs, indicating that the transformer can not accommodate the large output voltage signal at the chosen switching frequency. Furthermore, the transformer is a current sense transformer, who's primary application is reducing large currents to small signals for monitoring or feedback.

Low Efficiency The low efficiency of the demonstrated by the converter, both in the simulations and hardware testing, can also be linked to the transformer and the low power consumption of the device. The transformer chosen is a current sense transformer. As such, the relationship between primary and secondary side current is $I_p = nI_s$. Assuming all currents which are consumed by components in the circuit are negligible in comparison, then $I_p \sim I_{in}$ of the converter, and $I_s \sim I_{out}$. Using these relationships and approximations, the efficiency of the converter η could be estimated with Equation 5.3

$$\begin{aligned}
\eta &= \frac{P_{out}}{P_{in}} \\
\eta &\sim \frac{I_{out}^2 R_L}{I_{in} V_{in}} \\
\eta &\sim \frac{(I_{in}/n)^2 R_L}{I_{in} V_{in}} \\
\eta &\sim \frac{I_{in} R_L}{n^2 V_{in}}
\end{aligned} \tag{5.3}$$

Since the circuit should provide a low output power but large output voltage, R_L is large and on the order of $10^5\ \Omega$. For the case considered in this thesis, $V_{in} = 12$ V, $n = 200$, and ideally $P_{in} \lesssim 10$ W, thus $I_{in} \lesssim 833$ mA. Using the above equation to estimate the efficiency in this case leads to a result of $\eta < 2\%$. With this simplified analysis of the circuit, it is possible to demonstrate how the simultaneous requirements on high gain and low power consumption lead to the power conversion efficiency of the device being low. Clearly the analysis is overly simple and does not accurately describe the actual efficiency of the device across a range of operating points. However it does show the way in which the power efficiency is impacted by the requirements, and that a higher power consumption or lower gain would lead to higher efficiency.

6

Thermionic Cathode Neutralization

A key element of an ion thruster system is the cathode, which serves in establishing the potential difference responsible for accelerating the ions and in providing a neutralizing current so that charge does not build up on the spacecraft. In this chapter, the steps taken to assess whether a thermionic cathode technology would be suitable for the μACFT system are outlined. Analysis of the fundamental limitations of space charge accumulation imposed by the Child-Langmuir limit is provided alongside calculation of the emission current of various thermionic emitters. A design option trade off is executed to select the most suitable option from available technologies, and measurements made during testing of the μACFT are discussed.

6.1. Neutralization Efficacy

The objective of the cathode investigation is to determine whether a thermionic emitter can be effective. The meaning of effective must be defined in the context of neutralization of the μACFT plume. Neutralization of the thruster exhaust plume is considered effective it meets the following criteria.

1. Sufficient thermionic current is produced to sustain thruster operations.
2. Little power is required (< 10 W).
3. The technology is reliable and can sustain long term operations.

In order to address the first criteria, the Poisson equation for electric potential (Equation 2.46) can be analyzed in the context of the μACFT geometry in order to assess the likelyhood that the space charge limitation would impact the performance of a thermionic emitter. The Child-Langmuir space charge limit is calculated for the planar diode case (Equation 2.47), using the separation of the anode and cathode and the area of the anode to find the actual current. The space charge limit, formally a current density limit, is converted to an actual current using the geometry of the thruster. Since the current density in the planar case is more restrictive than in the cylindrical case, the analysis is relatively conservative.

The expected ion beam current is calculated for a range of mass efficiencies and propellant flow rates (Equation 2.6). By comparing this plume current to the Child-Langmuir limit at various thruster operating potentials, it is possible to assess whether this plume current would exceed the current which corresponds to the Child-Langmuir space charge limit. The thermionic emission current of a variety of thermionic emitters is calculated based on Equation 2.42 to determine the operating temperature required to achieve the plume current and the Child-Langmuir current limit.

In Figure 6.1 is a contour map showing the ion beam current of the μACFT as a function of the the mass efficiency and propellant flow rates. Highlighted in white contours are the Child-Langmuir current limit at the 145, 230, 900, and 1500 V operating points identified in Table 3.6. Also shown on the plot are the 145 V and 1300 V operating points for which the mass efficiency was calculated in Section 3.3.2.

In principle, the thermionic emitter must supply a current of electrons at least as large the ion beam current. Thus the proximity of the Child-Langmuir limit to the ion beam current at a given operating point can be used as an indicator for the suitability of a thermionic emitter.

Typically, the µACFT operates in the range 700 - 1500 V, and the Child-Langmuir current limit in this range exceeds the resulting beam current by approximately one order of magnitude. Thus for standard operating points for the µACFT, the cathode is not near the Child-Langmuir limit. However there in the current limited operating state, where anode potential is low and the beam current is high, the situation is the opposite.

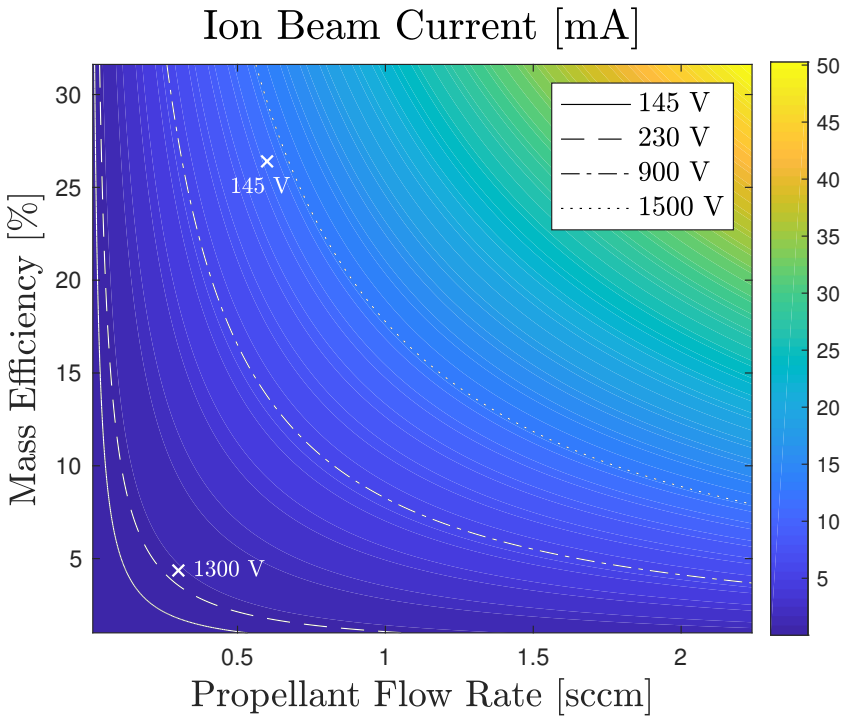

Figure 6.1: Ion beam current of CubeSat µACFT compared to the Child-Langmuir space charge limitation for a planar diode. At low voltage, high current operating points (145 V, 230 V) exceed the limit, while the high voltage operating points are far below the Child-Langmuir limit.

The current of the ion beam in the current limited case exceeds the Child-Langmuir space charge limit on the cathode emitter by nearly one order of magnitude, indicating space charge limitations could impact performance. Although a thermionic cathode technology might not be suitable for operations in the current limited state, it is certainly a feasible method for neutralizing the beam in standard operating states.

6.1.1. Design Option Trade Off

The next step in determining whether a thermionic cathode technology can neutralize the ion exhaust plume in a way that meets the criteria for effectiveness set forth at the start of this chapter is selecting the most suitable technology from the available options.

First, a list of available design options for thermionic cathodes is compiled. For example, Figure 6.2 shows the emitted current of a variety of thermionic materials. In generating the design option list, technologies with commercial availability and short development times are considered in order to comply with the new space design philosophy. In order to rank the design options, a trade off is conducted. The analytic hierarchy process (AHP) is selected as the trade off method. With this method, a number of trade off criteria are established and ranked systematically according to their importance relative to one another. Relative importance is evaluated pairwise. The result of ranking via the AHP is a weighting assigned to each criteria. Then the performance of each design option is scored with respect to each criteria according to defined thresholds. The overall score for each design option is calculated as:

$$T_i = w_j \tau_{ij} \tag{6.1}$$

where T_i is the total score for the ith design option, w_j is the weighting of the j$^{\text{th}}$ trade off criteria, and τ_{ij} is the corresponding score of the design option. Following on from the selection, the chosen technology should be analyzed and tested to assess the performance and ultimately determine if it is a suitable and effective cathode technology.

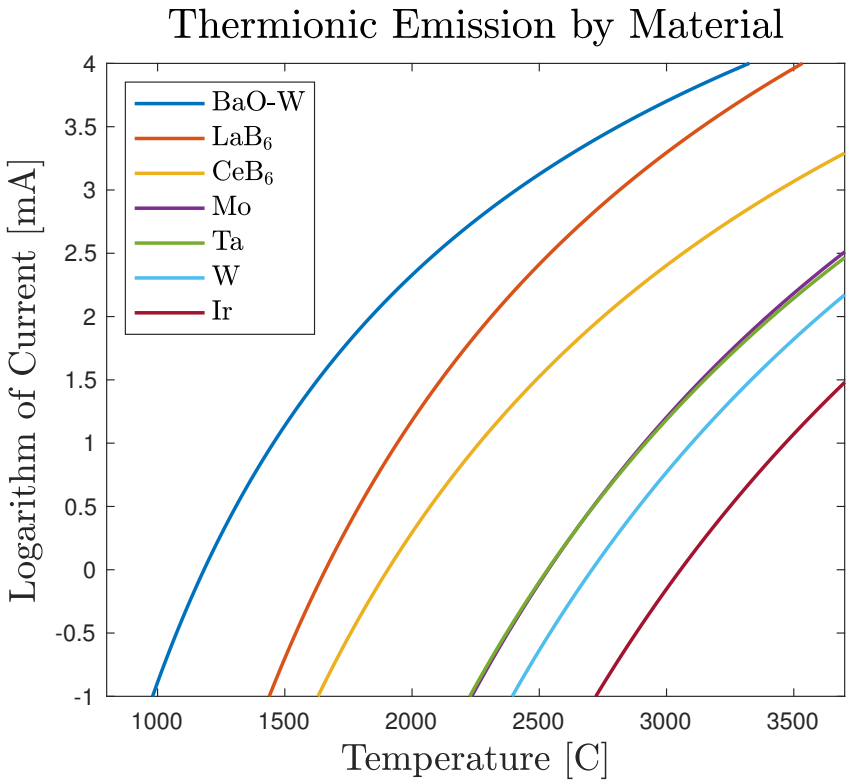

Figure 6.2: The thermionic emission of various cathode material options including refractory metals (Ir, W, Ta, Mo), boride crystals (CeB_6, LaB_6), and an oxide coated crystal (BaO-W).

Design Options The typical design options for thermionic emitters are refractory materials, both metals and ceramics. Refractory materials are those which are able to withstand very high temperatures. Both refractory metallic and ceramic materials can be used as a thermionic cathode. Refractory metals are familiar thermionic emitters which have a variety of commercial and scientific uses. Although the emission efficacy of refractory metal emitters is relatively low, they are reliable and inexpensive. However refractory metals with lower work functions generally require higher operating temperatures, which in turn leads to a higher evaporation rate and shorter lifetime. With respect to refractory ceramics, boride crystals are available commercially in the form of thermionic cathode neutralizers with moderate emission efficacy, but are typically very expensive. These crystals have a long lifetime and relatively high emission efficacy. Another design alternative are coated emitters, which are thermionic emitting materials whose modified surface properties which result in a lower material work function and an improvement in the emission efficacy. Although coated emitters are typically very efficient, they are also very susceptible to corrosion from any source due to the reactivity of the surface coating. On the other hand, boride crystals are strongly resistant to corrosion from atmospheric gases and iodine since they are ceramic refractories. Metals are typically resistant to corrosion when handled in atmospheric conditions, but not necessarily to a corrosive substance such as iodine.

1. Boride Crystal

   ex. Lanthum hexaboride, cerium hexaboride.

2. Coated Emitter

   ex. Barium oxide, thorium oxide, calcium aluminate, aluminum oxide, yttria coated iridium.

3. Refractory Metal

   ex. Molybdenum, tantlum, tungsten, rhenium.

The categories of boride crystal, oxide coated crystal and refractory metal are considered the design options for this trade off. The specific material selected from the winning design option category will depend on availability and cost.

Trade Off Criteria The trade off criteria selected stem from the initial criteria set out in this chapter which define effective neutralization of the exhaust plume. Cost is also included as a criteria in order to incorporate an element of the new space design philosophy, which favours inexpensive commercial products when they are suitable.

1. Reliability: The success rate of thruster ignition when using this design option.
2. Resistance to Corrosion: The ability of the design option to maintain an operating condition during handling and in proximity to iodine.
3. Emission Efficacy: The thermionic emission efficiency of the design option.
4. Lifetime: The length of time for which the design option can maintain thruster operations.
5. Cost: The cost of development or purchasing a product based on the design option.

The decision matrix for the AHP criteria ranking shows the relative importance of the criteria as ranked by the author. A scale of one to nine is used for the pairwise comparisons, where one indicates equal importance and nine indicates a extreme importance in favour of the criteria in the vertical column. In comparisons between criteria, the emphasis is first on the general reliability of the design option with respect to igniting the thruster, resisting corrosion from the iodine and atmospheric gases, and having a longevity suitable for the thruster. The second priority is the performance of the design option with respect to the it's thermionic emission efficacy, as this is directly related to the power consumption of the cathode. The lowest priority is cost.

	Reliability	Resistance to Corrosion	Emission Efficacy	Lifetime	Cost
Reliability	1	2	2	3	4
Resistance to Corrosion	1/2	1	2	3	2
Emission Efficacy	1/2	1/2	1	2	2
Lifetime	1/3	1/3	1/2	1	2
Cost	1/4	1/2	1/2	1/2	1

Solving for the principle eigenvector of this matrix provides the weighting, w_i, of each criteria. The consistency ratio of this decision matrix is 3.1%, indicating that the importance comparisons were self-consistent.

Table 6.1: Thermionic cathode emitter trade off criteria weightings.

Criteria	**Weighting**
Reliability	37.3%
Resistance to Corrosion	25.3%
Emission Efficacy	12.2%
Lifetime	11.4%
Cost	8.8%

Result The scoring of the design options with respect to each criteria is determined based on the thresholds outlined in Table 6.2. When calculating the final score of the design option, low corresponds to $\tau = 1$, acceptable to $\tau = 2$ and superior to $\tau = 3$. Scores are assigned based on available products, known material properties, as well as accumulated knowledge and test results. The scores of each design option are outlined Table 6.3 and the final result is shown in Table 6.4.

Table 6.2: Thermionic cathode technology trade off criteria thresholds used for AHP trade off.

Criteria	Low	Acceptable	Superior
Reliability	< 80%	80 - 90%	> 90%
Resistance to Corrosion	Significant Effect	Minor or Moderate Effect	No Effect
Emission Efficacy	< 2 mA/W	2 - 4 mA / W	> 4 mA/W
Lifetime	< 50 hours	50 - 100 hours	< 100 hours
Cost	> €500	€200 - 500	< €200

Table 6.3: Thermionic cathode design option scores for each AHP trade off criteria.

Design Option	Reliability	Resistance to Corrosion	Emission Efficacy	Lifetime	Cost
Boride Crystal	Acceptable	Superior	Acceptable	Superior	Low
Oxide Coated Crystal	Acceptable	Low	Superior	Superior	Acceptable
Refractory Metal	Superior	Acceptable	Low	Acceptable	Superior

Table 6.4: Result of AHP design option trade off for thermionic cathode emitter.

Design Option	Score
Boride Crystal	2.18
Oxide Coated Crystal	1.88
Refractory Metal	2.24

The result of this AHP trade off indicates that a refractory metal thermionic cathode is the most suitable option for the μACFT. Some decisions made during the analysis of trade off criteria had a large influence over the result. The emphasis on reliability of the design option coupled with the test results from the LET demonstrating that tungsten emitters are a reliable method of igniting the ACFT thrusters, had significant impact on the result. The runner up, boride crystals, is a good design option due to its resistance to corrosion and relatively high efficiency, but the key drawbacks of this option are the comparably low reliability and very high price. Although oxide coated crystals have the highest emission efficacy, they are the least suitable design option due to the low resistance to corrosion, comparably low reliability and moderately high price.

6.1.2. Test Results

The main focus for testing of the thermionic cathodes is based on observing the power consumed by the emitter and the thruster simultaneously. Firstly, the emitter power consumption is monitored to calculate its contribution to the overall power budget. The thruster power is monitored in order to explore the correlation between cathode power and thruster power. The measurements are summarized in Table 6.5.

Table 6.5: Summary of thermionic cathode measurements, alongside the intended outcomes and underlying motivation.

Measurement	Outcomes	Motivation
Cathode emitter input power	Total power consumption.	RQ-4, RQ-1 and all sub-questions.
Thruster input power	Total power consumption.	RQ-4, RQ-1 and all sub-questions.

In testing, typically four to six tungsten filaments were placed near the exit of the discharge chamber, with a single filament taking the place of the cathode 29 mm from the anode. It was observed that typically a large input power (8.7 - 9.6 W) distributed across all the filaments was required to ignite the thruster. However following ignition, the thruster could be operated without the additional filaments, relying on only a single filament in the cathode position.

For a tungsten filament operating at the typical operating temperature of 2500 - 3000 K, the theoretical thermionic current output is between 0.03 - 1.45 mA/cm^2. Measured current densities of the µACFT ion beam are between 1 $\times 10^{-4}$ - 9 $\times 10^{-3}$ mA/cm^2. Thus a single tungsten emitter can emit sufficient neutralizing current to operate the thruster, provided that the recombination rate is sufficiently high and the space charge limit is not reached.

During the xenon test campaign, the thruster was observed to operate reliably at standard operating points using a single tungsten filament with only 1.8 W of input power. On the other hand, the thruster could maintain current limited operations with 7.6 W of input power to the filaments. Further decreasing the cathode power input results in the thruster transitioning back into the standard operating state. During the iodine test campaign, the thruster could be operated at the current limited operating point with only the cathode filament, consuming 2.5 W of input power. Typically, the thruster power would decrease along with the cathode power until the discharge would extinguished. In the other direction, the thruster power would increase with the cathode power. However at a certain point the thruster power saturates and will no longer increase with the cathode power.

6.2. Discussion and Conclusion

In this chapter, the viability of using a thermionic emitter as an effective cathode neutralizer for the iodine µACFT is investigated. Neutralization of the exhaust beam of the thruster is defined as effective if sufficient thermionic current is supplied to sustain operations, little power is consumed by the the neutralizer, and the technology is reliable over a relatively long period of time. Both analytic and experimental methods are employed to explore the issue. A trade off is conducted to determine what the most suitable thermionic technology is for the system, and experimental results obtained during testing of the µACFT are presented.

The design option trade off was conducted to determine whether a boride crystal, coated emitter, or refractory metal is the most suitable thermionic emitter for a cathode. The criteria used in the trade off are reliability, resistance to corrosion, emission efficacy, lifetime and cost. The AHP method was used to rank the criteria based on relative importance, and thresholds are applied to the criteria to assess the performance of each design option relative to each criteria. Ultimately the refractory metal scored highest in this design trade off due to the highly weighted importance of the reliability and resistance to corrosion. In the end a tungsten filament was selected for the µACFT due to the high reliability, easy handling, moderate resistance to iodine, suitable efficiency and lifetime, and very low cost.

The Child-Langmuir law for the space charge density limit in a planar diode is applied to the case of the µACFT to determine whether a thermionic emitter is likely to be space charge limited in the context of µACFT operating points based on the corresponding ion beam current which must be neutralized. The planar diode geometry is selected since it provided a more conservative result compared to the space charge limit in a cylindrical geometry. The space charge limit predicted by the Child-Langmuir law is converted into a current limit on the emitter, which is compared to the typical ion beam currents of the µACFT to assess the risk of the neutralizer becoming space charge limited. This analysis shows that a neutralizer would not be risk of becoming space charge limited in standard operations, where the anode voltage is in the range 700 - 1500 V and the beam current is in the range 1.5 - 7.5 mA. However in current limited operations, where the voltage is less than 300 V and the anode current is 20 mA, the space charge limit may prevent effective neutralization of the ion beam. However in testing, the tungsten emitter is used to successfully ignite and run the thruster in the current limited state. The limitations of the analysis which may have lead to this contradiction between the model and test observations include the geometry of the diode being greatly simplified, and not taking into account the recombination of the electrons with ions in the plume reducing the negative space charge build up.

In testing, the tungsten filament demonstrated adequate performance as a neutralizer across all tested operating points. Although a relatively high power was used during ignition of the thruster, the total power consumption of the thermionic emitters used stayed below 10 W. The total power consumption of the single tungsten filament cathode was as low as 1.8 W during standard operation with xenon, and 2.5 W during current limited operation with iodine.

7

Conclusion

In the new space paradigm, the CubeSat has proven to be an incredibly popular satellite platform which has lead to the emergence of various new companies and engineering groups at universities which are building and operating these spacecraft. Many researchers and developers in the industry are planning for future CubeSat missions which incorporate swarm formation services for Earth, deep space exploration, or debris removal. A key technology which would enable these types of missions is small sized CubeSat compatible propulsion systems. In the field of electric propulsion, iodine based systems may have game changing potential when it comes to CubeSat propulsion systems. Since the propellant can be stored as a solid, the thruster design can become compact and unpressurized. In this thesis, the design, construction and and testing of a miniature iodine-fed advanced cusped field thruster (μACFT) for the 3U+ CubeSat platform is outlined. The overall objective the project is to validate the use of iodine as a viable propellant alternative to xenon in the context of CubeSat electric propulsion systems by demonstrating the concept via an iodine μACFT engineering model.

The performance of the iodine μACFT EM is measured at the Laboratory for Enabling Technologies at Airbus Friedrichshafen. The measured performance is compared to previous μACFT demonstrators, other CubeSat thrusters, as well as other iodine thrusters. Key factors unrelated to propellant choice which impact the performance of the device are identified. Additional research questions related to the thruster subsystems were also explored throughout the project. The topics relate to characterizing the iodine feed system for the thruster, designing an LLC resonant DC/DC converter for the μACFT power processing unit, and determining the suitability of using a thermionic emitting cathode technology. The research objective and questions which guided the activities of the this thesis are as follows:

OBJ-1: To investigate the viability of iodine as a propellant alternative (to xenon) for ion electric propulsion systems in the context of CubeSat applications by constructing and testing a fully integrated engineering model of an iodine-fed μACFT device.

RQ-1: How does the thruster performance compare in the context of the legacy of miniaturized ACFT devices?

RQ-1A: How does the device compare relative to other iodine thrusters?

RQ-1B: How does the performance compare to other CubeSat thruster alternatives?

RQ-1C: Aside from propellant choice, what other aspects of the μACFT design impact the performance?

RQ-2: What flow regime(s) characterizes the iodine vapour feed system?

RQ-2A: What is the sublimation rate of iodine in the context of the feed system? To what extent is it described by the Langmuir sublimation model?

RQ-2B: What is the mass flow rate through the thruster?

RQ-3: What performance can an LLC resonant converter achieve in the proposed low-power, high-voltage application?

RQ-4: Can a thermionic cathode technology effectively neutralize the thruster ion plume?

In the following section, an assessment of the iodine μACFT status with respect to the system requirements is first provided. Then, the key outcomes of each chapter of the report are summarized in a way to address each of the related research questions. Lastly, there is a section discussing ideas and topics for future work.

7.1. Summary and Key Outcomes

In the introduction to this thesis (Chapter 1), the relevant context for CubeSats and electric propulsion are discussed to establish a motivation for the project. In Chapter 2 the fundamentals of electric propulsion are introduced, along with the μACFT concept and theories from plasma physics which are relevant to design of a cusped field thruster. The specific benefits of using iodine as propellant for CubeSat propulsion systems are discussed as well. Then the relevant theories required for the characterization of the feed system fluidics, design of an LLC resonant DC/DC converter, and assessment of thermionic emitters and cathodes are discussed. Following on in Chapter 3, the design of the iodine-fed μACFT is described in detail, beginning with the synthesis of the system requirements. The thruster is designed for use on a 3U+ or larger CubeSat, and is housed inside the tuna-can extension of the spacecraft. Measurements made in performance characterization are discussed and compared to other μACFT devices, CubeSat thrusters, and iodine thrusters. Chapter 4 covers the iodine feed system characterization with respect to the flow regime and mass flow rate. In Chapter 5 is a discussion of the design and testing of a resonant LLC DC/DC converter for the μACFT power processing unit. Finally, in Chapter 6, the the design and assessment of the thermionic cathode neutralizer is described.

μACFT EM Status The μACFT EM was tested with both xenon and iodine propellants. The specifications achieved with the final iodine-fed μACFT EM are summarized in Table 7.1.

Table 7.1: Specifications of iodine μACFT engineering model. * indicates an estimated parameter

Parameter	Specification
Dry Mass (No PPU)	280 g
Iodine Capacity	200 g
Size	180 cm^3
Power	8.3 - 11.6 W
Thrust	227 - 254 (± 1) μN
Specific Impulse *	103 - 115 (± 48) s
Efficiency	4.0%
Δv (3U CubeSat) *	49.3 - 55.0 m/s

The compliance of the thruster with respect to each of the system requirements is shown in Tables 7.2 and 7.3. The key shortcomings of the current design with respect to the requirements are related to the power processing unit (PWR-002, PWR-003, PWR-004, PWR-005) and feed system inhibitor (PRO-003). Other requirements still remain to be verified. These are generally related to which launcher and launch range are chosen for the CubeSat. The selection will dictate the further requirement breakdown of PRO-002, MEC-003, and EMI-002.

Table 7.2: Compliance of μACFT EM with MEC system requirements.

ID	Requirement	Outcome	Remark
MEC-001	The thruster shall fit within a 3U+ CubeSat platform.	Compliant.	System envelope includes tuna-can extensions and one-third of 1U.
MEC-002	The thruster wet mass shall not exceed 1.00 kg, or 25% of the total 3U+ CubeSat mass.	Compliant.	Dry mass is 280 g and the propellant capacity is 200 g.
MEC-003	The thruster shall withstand vibrational and static loads of the chosen launcher.	Unverified	Launcher must be chosen and then the requirement can be elaborated. Both simulation and environmental tests will be necessary.

Table 7.3: Compliance of μACFT EM with PRO, FL, PWR, and EMI system requirements.

ID	Requirement	Outcome	Remark
PRO-001	The thruster shall not incorporate pyrotechnics.	Compliant.	No combustion or pyrotechnics used in thruster design concept.
PRO-002	The thruster shall comply with the AFSPCMAN 91-710 hazardous materials allowances.	Unverified.	Iodine is corrosive to some materials and would likely need to be approved on a mission basis.
PRO-003	The thruster shall comply with AFSPCMAN 91-710 inhibit requirements.	Non-compliant.	Current inhibitor needs to be replaced with an insulating material since it contributes to thruster backfiring.
PRO-004	Stored chemical energy in the thruster shall not exceed 100 Whr.	Compliant.	The heat of vaporization of 200 g of molecular iodine is only 18 Whr.
PRO-005	The thruster shall not incorporate pressurized vessels.	Compliant.	The pressure in the feed system is far below atmospheric levels.
PRO-006	The thruster shall provide at least 10 m/s of Δv capability for a 3U+ CubeSat platform.	Unverified.	According to estimation of the specific impulse, Δv appears to meet the requirement but direct measurement is necessary.
FL-001	The feed system shall incorporate materials which are resistant to iodine vapor corrosion.	Compliant.	Feed system composed of PEEK.
FL-002	The reservoir shall reach a temperature high enough to sublimate Iodine.	Compliant.	Feed system is heated to 50 - 60°C.
FL-003	The feedline temperature shall exceed the reservoir temperature.	Compliant.	Secondary reservoir temperature exceeds reservoir temperature by 10°C.
FL-004	All components shall remain within their operational temperature range.	Complaint.	Thruster operates below maximum temperature of PEEK and the NdFeB magnets.
PWR-001	The power processing unit shall operate on a 12 V regulated, or unregulated, input voltage.	Complaint.	The converter uses the 12 V and 5 V lines of the PC/104 bus.
PWR-002	The power processing unit shall be compliant with the PC/104 standard.	Non-compliant.	Converter uses PC/104 inputs but does not have the PC/104 connection harness.
PWR-003	The power processing unit shall provide up to 10 W of power.	Non-compliant.	Maximum measured power output of the converter is 2.4 W.
PWR-004	The power processing unit duty cycle shall 50%, or greater.	Non-compliant.	The converter was not tested with the thruster for duty cycle measurements.
PWR-005	The power processing unit shall provide up to 1.5 kV controllable output voltage.	Non-compliant	Maximum output achieved is 780 V.
EMI-001	The thruster magnetic field shall not exceed 0.5 G greater than Earth's.	Compliant.	The thruster magnetic field is 40 - 50 μG and thus cannot exceed that of Earth by such a large margin.
EMI-002	The thruster shall comply with the EMI requirements of the chosen launcher.	Unverified	Launcher must be chosen and then requirement can be elaborated.

Thruster Performance Comparison The μACFT EM was tested with both xenon and iodine propellant. Direct thrust and plasma diagnostic measurements were made with both propellants. The outcomes of the measurements include thrust generated, power-to-thrust-ratio, specific impulse and total thruster efficiency. The μACFT operated in standard and current limited operating modes with xenon, but only the current limited mode was possible with iodine.

> **RQ-1**: How does the thruster performance compare in the context of the legacy of miniaturized ACFT devices?

The μACFT EM in this thesis performed well in comparison to previous μACFT demonstrators in terms of power-to-thrust-ratio, specific impulse, total thrust generated and total efficiency. The current EM demonstrated the best recorded thrust, power-to-thrust-ratio, and efficiency of any μACFT system. The best performance measurements were all made when the thruster was in a current limited operating mode. The operating state could be reliably reached with the current EM with a mass flow rate of 0.6 sccm or higher, and sustained with a mass flow rate as low as 0.35 sccm. The operating state was first achieved following an observation that a small current (10's μA) travelling from the thermionic emitter into the anode high voltage line. The combination of the presence of additional charge in the chamber along with a higher mass flow rate may contribute to a more extensive plasma breakdown. During this mode of operations, the thruster demonstrated a greater specific impulse, thrust, power-to-thrust-ratio, as well as divergence, mass and discharge efficiency in comparison to the typical μACFT operating points. However there is a noted disadvantage in the acceleration efficiency when operating at lower anode voltage.

The performance of the thruster with iodine propellant exceeds the performance of all documented operating points of the μACFT using xenon with respect to total thrust and power-to-thrust-ratio. However the specific impulse and efficiency are higher with xenon. The increase in thrust is most likely due to the increase in mass flow during iodine testing, which is estimated to be 2.1 sccm. However, since the mass flow rate in the iodine μACFT is not directly controlled, it is instead estimated using a thermodynamic model. Thus the results presented for specific impulse are estimates and have large uncertainties. Operations are more consistent with xenon since the thruster is very sensitive to fluctuations in temperature when running with iodine. The operating temperatures of 50°C in the reservoir and 60°C in the secondary chamber are critical, as a lower secondary chamber temperature or higher reservoir temperature would result in the discharge extinguishing.

> **RQ-1A**: How does the device compare relative to other iodine thrusters?

The field of iodine thrusters discussed in literature consists of two other CubeSat thrusters (the Neptune and BIT-3), four larger thrusters, and the iodine μACFT. Although the maximum thrust generated by the μACFT is comparatively low, the power consumption is significantly lower than all the others as well. As a result, the power-to-thrust-ratio of the μACFT is very low, and comparable to the larger more efficient thrusters. The size and mass of the μACFT is very small with respect to the other iodine CubeSat thrusters. Ultimately, the μACFT is the smallest iodine thruster which has been built and successfully tested at the time of writing, and the only iodine thruster which is suitable for the 3U+ CubeSat platform due to it's small size and power consumption.

> **RQ-1B**: How does the performance compare to other CubeSat thruster alternatives?

With respect to other CubeSat thrusters, the μACFT performs similar to the other electrodynamic and electrostatic thrusters in the same power and size class. In comparison to cold gas and electrothermal thrusters, the specific impulse of the μACFT is higher, while the thrust is lower. Within the groups of electrostatic and electrodynamic thrusters, the μACFT shows notable deviation from the average in power-to-thrust-ratio, where the μACFT has an advantage, and in specific impulse, where it has a disadvantage. In overall volume, the μACFT is one of the smallest out of the electrodynamic thrusters identified in this thesis which have a comparable size and power consumption. In addition to the small size, making use of the tuna-can housing is a distinct advantage of the μACFT from a systems engineering perspective, since almost no volume is taken up inside the main body of the CubeSat. Another advantage is the relatively low EMI of the μACFT in comparison to the pulsed plasma thrusters (PPT) which are popular in the field of miniature, low power electrodynamic thruster.

RQ-1C: Aside from propellant choice, what other aspects of the μACFT design impact the performance?

Only a small contribution to the change in thruster performance can be attributed to the fundamentally different ionization energy and atomic mass of the iodine and xenon propellant. The most major design change in the iodine μACFT EM relative to the previous EM is the incorporation of the iodine propellant feed system, which was prone to backfiring. Any conductor used inside the assembly of the feed system which comes in contact with iodine vapour could contribute to backfiring. The temperature of the feed system, which is related to the pressure inside, must be raised in order to prevent backfiring. As a result of higher temperature operation, the mass flow rate through the thruster was high, leading to additional thrust, but a reduction in the specific impulse. Aside from the feed system, it was noted that the positioning of the discharge chamber relative to the end face of the thruster may be leading to more collisions with the chamber walls near the exit of the chamber. This leads to erosion of the insulating coating on the chamber, and reduced specific impulse as more ions do not make it to the plume and contribute to the momentum transfer.

Feed System Fluidics The simplified μACFT design excludes a mass flow controller for the sake of reducing size, cost and complexity. As a result, the mass flow rate of iodine propellant is controlled indirectly through the temperature of the feed system. A series of experiments were conducted with true-to-size feed system testers in order to determine the flow regime inside the μACFT feed system and estimate the mass flow rate in the thruster.

RQ-2: What flow regime(s) characterizes the iodine vapour feed system?

The relatively high pressure in the feed system and the small dimensions of the feed system combine such that the flow is in the transitional regime between free molecular and laminar. A three stage feed system model was constructed based on this observation.

RQ-2A: What is the sublimation rate of iodine in the context of the feed system? To what extent is it described by the Langmuir sublimation model?

By measuring the mass loss through a replica feed system into the vacuum environment, the mass flow rate and pressure inside the reservoir are estimated. The measured sublimation rate of iodine was between 0.05 - 0.40 mg/s at 20°C and 50°C respectively. The observations show that the reservoir pressure would rise to within 1% the vapour pressure of iodine, which is typically in the range a 1 - 10 mbar for temperatures below 100°C. This indicates that the Langmuir quasi-equilibrium sublimation equation is certainly applicable as it is intended for estimating the sublimation rate of the materials near the vapour pressure. However it was also noted that the Hertz-Knudsen equation for vacuum evaporation could be used to achieve a nearly identical result, and is more suitable than the Langmuir model for the case that the surrounding pressure is much lower than the vapour pressure of the material.

RQ-2B: What is the mass flow rate through the thruster?

The mass flow rate through the discharge chamber, and the pressure in the secondary chamber of the feed system can be estimated as a function of the temperature using the three stage feed system model. The measurements and model reveal that at temperatures beyond room temperature, the mass flow rate into the discharge chamber grows exponentially. At the operating point tested in this thesis, the reservoir temperature was 50°C, leading to an estimated mass flow rate of 2.1 sccm (0.4 mg/s). This far exceeds the mass flow rates required to operate the μACFT, which was tested in the range of 0.15 - 0.8 sccm using xenon. In principle, a mass flow rate in this range could be achieved at room temperature, but operating at higher temperatures is necessary in order to maintain a high enough pressure in the feed system to prevent backfiring.

Resonant DC/DC Converter The μACFT relies on a high potential anode to accelerate ions and generate thrust. Thus the engineering model requires a power processing unit to convert the 12 V input line available from the CubeSat into a much higher potential. An LLC resonant DC/DC converter was selected for the μACFT since the topology offers a very high power efficiency. However the power requirements of the μACFT system present a mixture of objectives which are not common for DC/DC converters. Namely, the combined low power requirement (PWR-002) and high voltage gain (PWR-004). The suitability of the LLC resonant converter in this context required investigation. The research question guiding the activities is:

> **RQ-3**: What performance can an LLC resonant converter achieve in the proposed low-power, high-voltage application?

A half bridge LLC resonant converter design with an input voltage of 12 V, resonant frequency of 200 kHz, and nominal output voltage of 1200 V was designed using an $n = 200$ current sense transformer. The design was successfully demonstrated on a breadboard using a smaller transformer ($n = 5$) and a Multisim simulation of the circuit was validated based on the breadboard measurements. However after switching in the larger transformer and transferring the design to a printed circuit board, the converter failed to meet the performance requirements for voltage gain and power output.

Three key issues were identified with the LLC resonant converter design which are ultimately related the high voltage gain, low power consumption application. First, achieving a high output voltage and low power consumption simultaneously requires an output load much larger than what is typical for the μACFT. Furthermore, the high voltage gain requires a transformer with a large turns ratio. The combination of large load and large turns ratio results in a quality factor of $Q \sim 0$, meaning the designer no longer has a free design parameter for selecting the converter gain curve. Secondly, the voltage-time product of the chosen transformer is such that a very high switching frequency is required in order to accommodate the very large voltage swings on the secondary side. However selecting a switching frequency high enough to accommodate the voltage time product of the transformer would require the reactive components in the resonant tank to shrink to a point that they are comparable to parasitic elements. Furthermore, power losses in the reactive components increase with frequency, and thus this would result in a decrease in power conversion efficiency. Lastly, a current transformer with a large turns ratio used to step up a voltage for a low power output load results in a low power conversion efficiency. Increasing the power consumption at the load and decreasing the turns ratio of the transformer are both ways to mitigate this effect and improve the efficiency.

Thermionic Cathode Neutralization As an ion thruster, the μACFT requires a neutralizer for the mitigating negative charge build up onboard the CubeSat. The suitability of using a thermionic emitter for beam neutralizing is explored in Chapter 6. The research question related to the cathode activities is:

> **RQ-4**: Can a thermionic cathode technology effectively neutralize the thruster ion plume?

A thermionic cathode technology is considered effective it can provide enough current to ignite and maintain the plasma discharge, consumes little power, and can remain reliable over long term operations.

The Child-Langmuir law is used to estimate the practical limitations of a thermionic cathode when it comes to producing a thermionic current to match the ion beam current. It was found that space charge limitations should have no effect on the μACFT during normal operations where the anode voltage is in the range 700 - 1500 V and the plume current is in the range of 1.5 - 7.5 mA. However in the current limited operating state, the conditions suggested that the cathode would be Child-Langmuir limited.

A design trade off using the analytical hierarchy process was conducted to select the most suitable technology for thermionic neutralization of the ion plume. An emphasis on reliability and resistance to corrosion was made in ranking the relative importance of trade off criteria, resulting in refractory metals being the best design option. Ultimately tungsten was chosen for the μACFT. It was confirmed via experimentation that a tungsten emitter can be used to ignite and maintain the plasma discharge in both the standard and current limited operating points. The tungsten filaments used in testing came from commercial lightbulbs. A single filament of this type is not robust enough to handle the power consumed during ignition. Thus the test results presented serve only as a validation of the concept, but not a validation of the hardware.

7.2. Future Work

With respect to the iodine μACFT as a whole, multiple system requirements are not met with the current EM. Many of these requirements must be verified in collaboration with the CubeSat designer and launch provider. For example, the load tolerances of the mechanical design are not known but must be both analyzed and tested in future work. The compliance with the EMI restrictions, hazardous material allowances, and inhibit requirements are dependant on the chosen launcher. The remaining requirements for which the current EM is non-compliant are related to the power processing unit and the feed system inhibitor.

Despite the feed system design concept used in the iodine μACFT EM being successfully demonstrated in this thesis, various improvements can be made. First of all, the thermal actuator and valve head sealing the propellant reservoir was removed, eliminating the main propellant flow inhibit in the thruster. Since the titanium valve head used in the thermal actuator serves as an electron source for backfiring discharges, it should be replaced with an insulating material. The sealing between the individual parts of the feed system, and between the feed system and the discharge chamber insulation should be improved since in some cases sealing was poor. Integration of the feed system into the thruster could be improved by providing a separate mounting opportunity for the secondary chamber aside from the screws which secure the discharge chamber and ceramics. Lastly, the control of the pressure in the secondary chamber can be improved by moving the orifice away from the interface between the propellant reservoir and the secondary chamber, and instead positioning it between the anode and secondary chamber. As a result, the secondary chamber pressure would increase, and then the risk of backfiring decreases. Furthermore, by manufacturing a micro-scale orifice, the mass flow can be sufficiently limited to mass flow rates below 2 sccm. Alternatively, by incorporating an orifice with an area that can be modulated, the mass flow rate of the thruster could be controlled via this mechanism instead of temperature. This would relieve the current issue of operating at critical temperature points, this could reduce the overall power consumption for heating, and reduce the thermal load on the CubeSat. Lastly, the temperature of the housing of the thruster should be monitored in testing to determine what temperature will be in contact with the CubeSat structure.

The resonant DC/DC converter design concept used for the μACFT failed in that it does not provide the voltage gain nor the power output required for the thruster. Multiple reasons have been identified as to why the performance and design space of the LLC resonant converter are limited when both high gain and low power consumption are desired simultaneously. However specific issues exist with the current design which could be improved in future work. In order to achieve the high gain with the current design while maintaining a reasonable switching frequency, a transformer with a larger voltage time product is required. Furthermore, with a reduction in the resistance of the transformer, a peak efficiency closer to 50% could be achieved. The converter model in Multisim should be improved to account for the voltage time product of the transformer. It may be possible to create an effective model with a low pass filter at the transformer input. Regardless, since the large turns ratio necessary to achieve a high output voltage with only a single gain stage leads to a low power output, redesigning the converter to boost the voltage in multiple stages would likely lead to better performance overall. In order to increase the power throughput of the converter, a full bridge switching regulator should be considered.

A thermionic emitter is shown to be an effective cathode neutralizer for the μACFT system. However, with respect to both the theoretical and practical developments demonstrated in this thesis, many improvements are necessary. Firstly, a more accurate assessment of the space charge can be made with a finite element solution of the Poisson equation. The model should take into account the positive space charge of the plume and the actual geometry of the thruster. Secondly, a more robust mechanical design of the tungsten filament is necessary. A design which either incorporates multiple small filaments, or one larger one, is required in order to accommodate the large power consumption during thruster ignition.

A

Project Planning

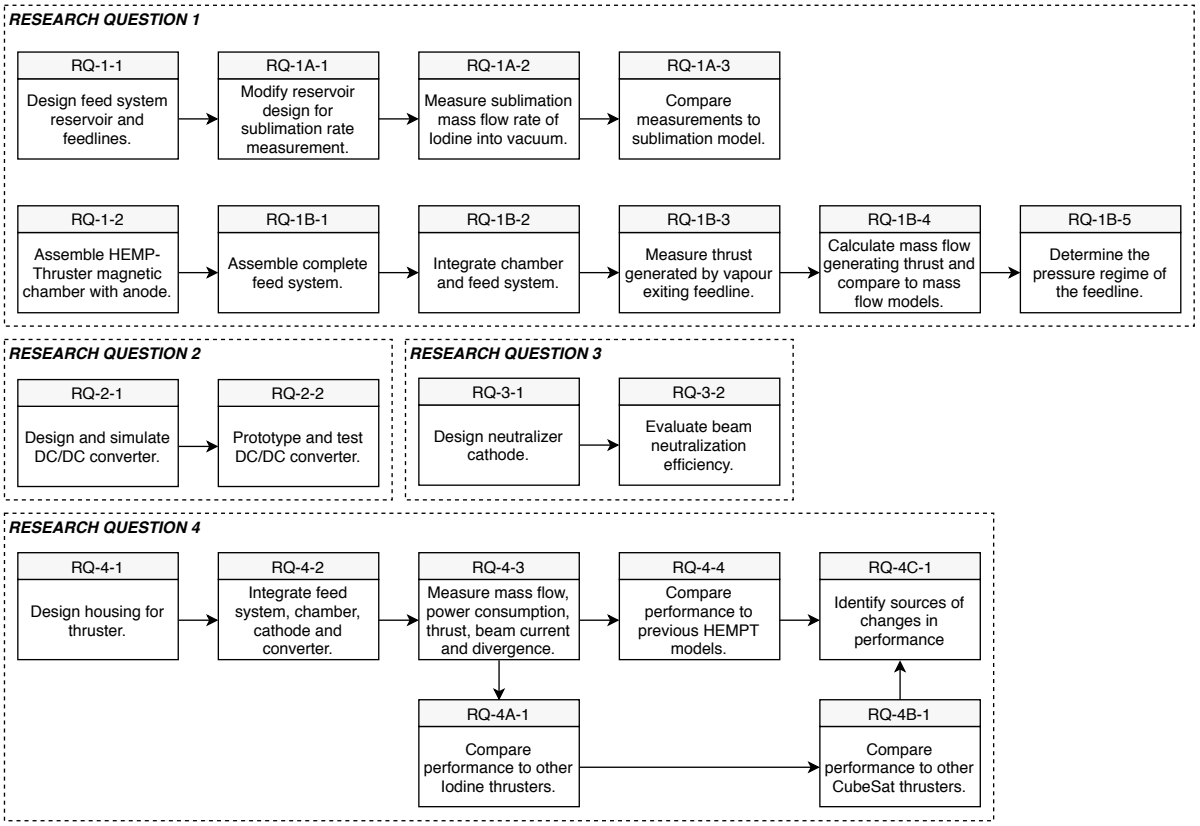

Figure A.1: Work flow diagram for thesis project activities, organized by research questions.

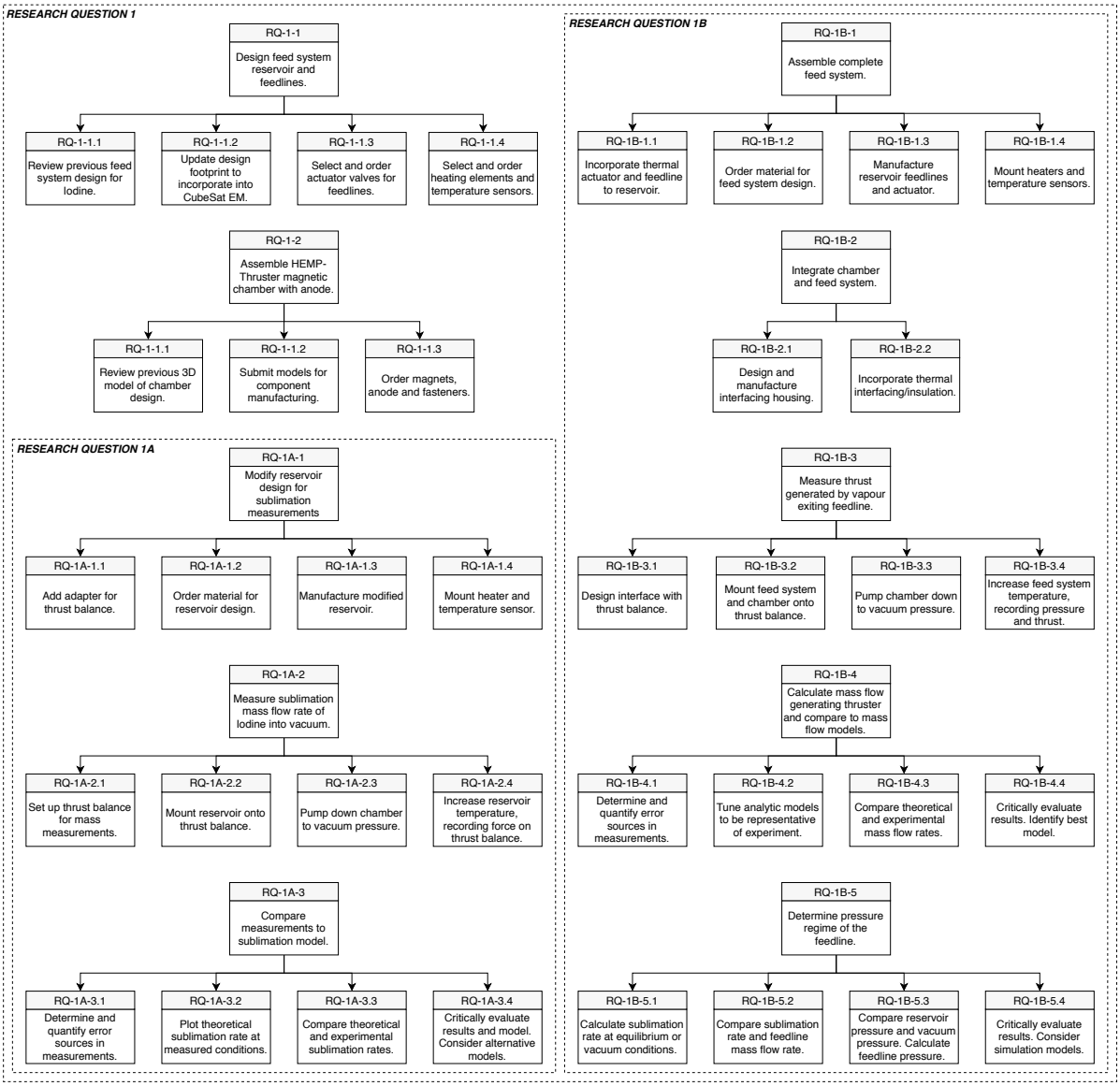

Figure A.2: Work breakdown structure for Research Question 1.

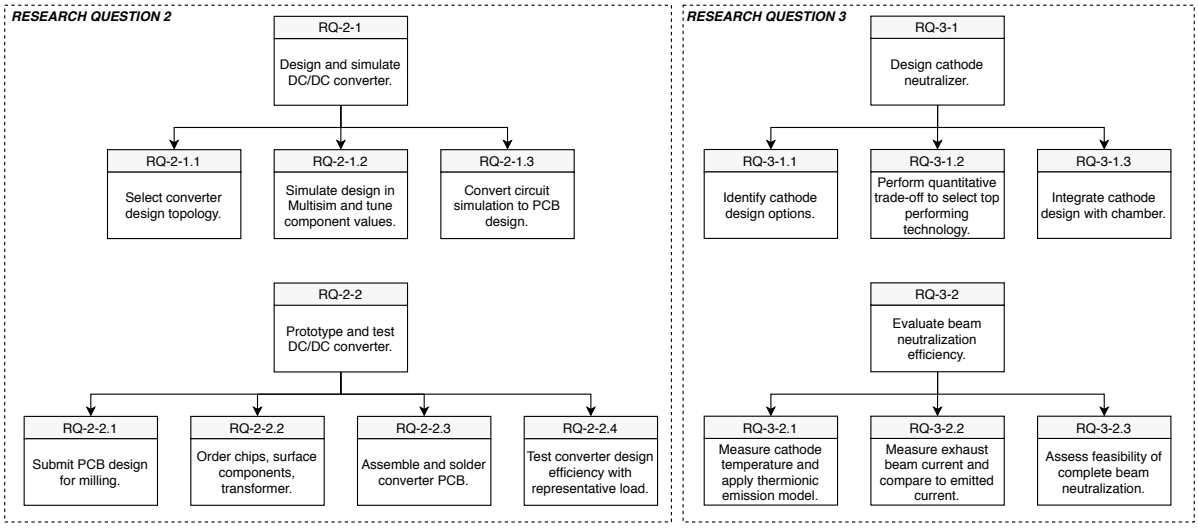

Figure A.3: Work breakdown structure for Research Questions 2 and 3.

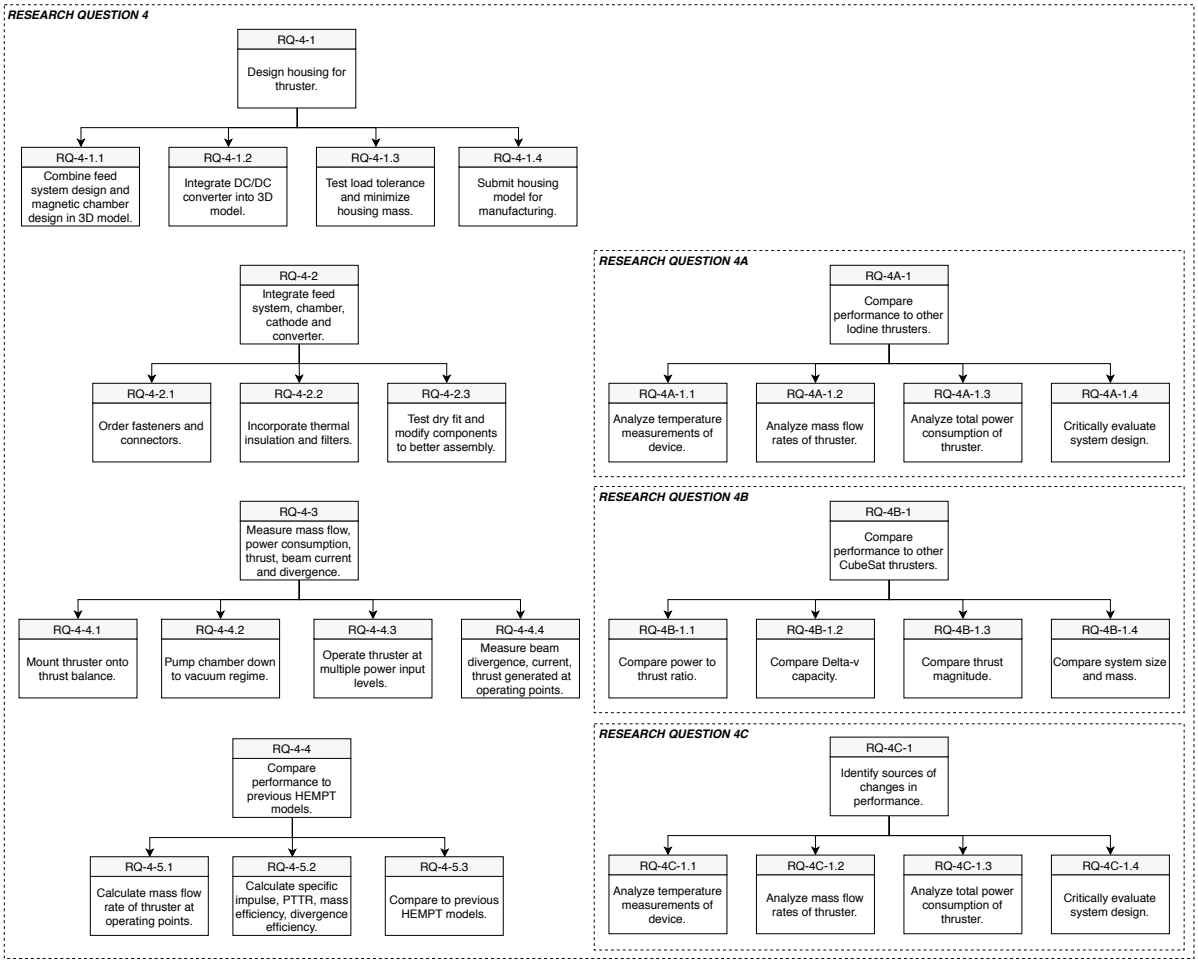

Figure A.4: Work breakdown structure for Research Question 4.

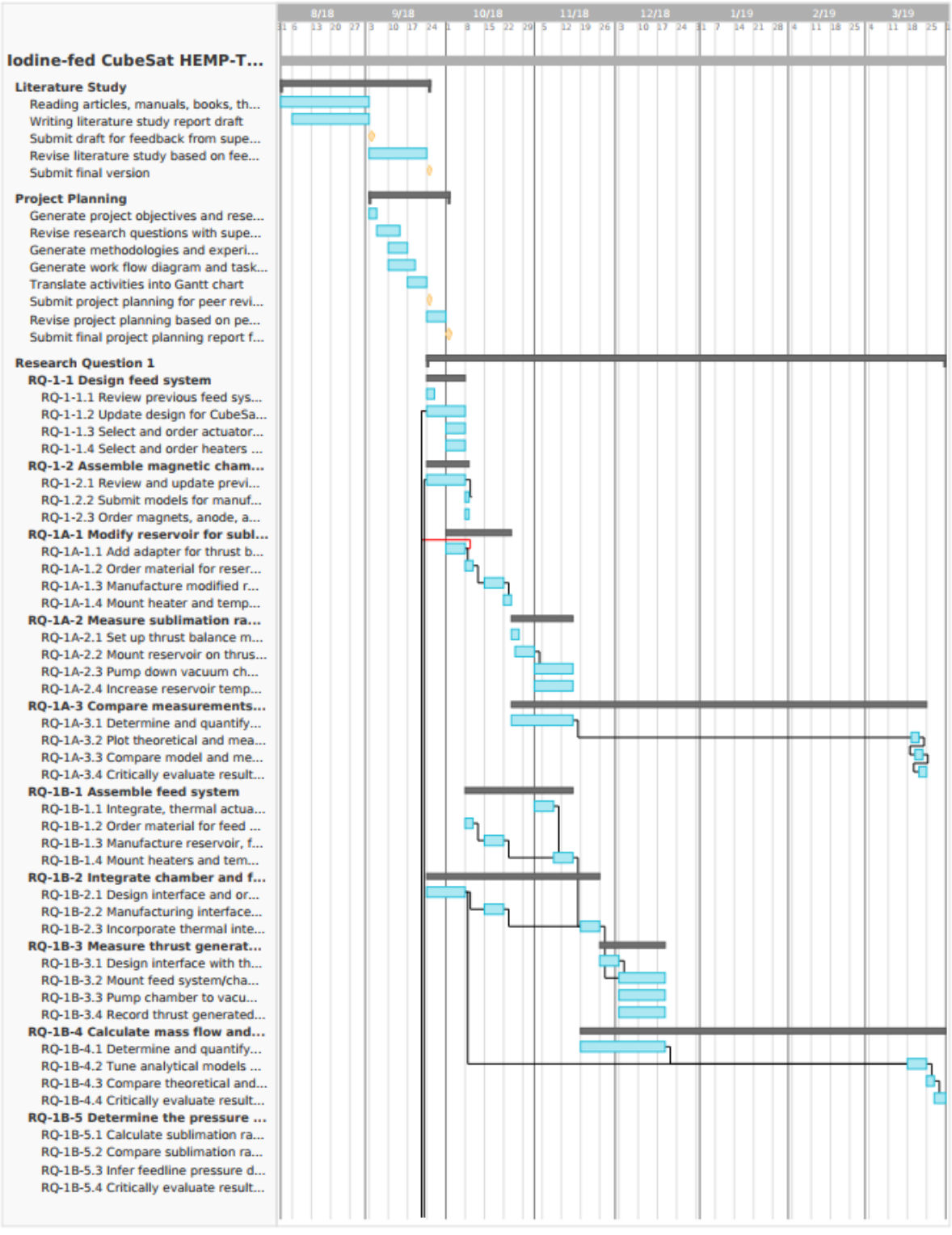
8/18
9/18
10/18
11/18
12/18
1/19
2/19
3/19
Iodine-fed CubeSat HEMP-T...
Literature Study
Reading articles, manuals, books, th...
Writing literature study report draft
Submit draft for feedback from supe...
Revise literature study based on fee...
Submit final version
Project Planning
Generate project objectives and rese...
Revise research questions with supe...
Generate methodologies and experi...
Generate work flow diagram and task...
Translate activities into Gantt chart
Submit project planning for peer revi...
Revise project planning based on pe...
Submit final project planning report f...
Research Question 1
RQ-1-1 Design feed system
RQ-1-1.1 Review previous feed sys...
RQ-1-1.2 Update design for CubeSa...
RQ-1-1.3 Select and order actuator...
RQ-1-1.4 Select and order heaters ...
RQ-1-2 Assemble magnetic cham...
RQ-1-2.1 Review and update previ...
RQ-1.2.2 Submit models for manuf...
RQ-1-2.3 Order magnets, anode, a...
RQ-1A-1 Modify reservoir for subl...
RQ-1A-1.1 Add adapter for thrust b...
RQ-1A-1.2 Order material for reser...
RQ-1A-1.3 Manufacture modified r...
RQ-1A-1.4 Mount heater and temp...
RQ-1A-2 Measure sublimation ra...
RQ-1A-2.1 Set up thrust balance m...
RQ-1A-2.2 Mount reservoir on thrus...
RQ-1A-2.3 Pump down vacuum ch...
RQ-1A-2.4 Increase reservoir temp...
RQ-1A-3 Compare measurements...
RQ-1A-3.1 Determine and quantify...
RQ-1A-3.2 Plot theoretical and mea...
RQ-1A-3.3 Compare model and me...
RQ-1A-3.4 Critically evaluate result...
RQ-1B-1 Assemble feed system
RQ-1B-1.1 Integrate, thermal actua...
RQ-1B-1.2 Order material for feed ...
RQ-1B-1.3 Manufacture reservoir, f...
RQ-1B-1.4 Mount heaters and tem...
RQ-1B-2 Integrate chamber and f...
RQ-1B-2.1 Design interface and or...
RQ-1B-2.2 Manufacturing interface...
RQ-1B-2.3 Incorporate thermal inte...
RQ-1B-3 Measure thrust generat...
RQ-1B-3.1 Design interface with th...
RQ-1B-3.2 Mount feed system/cha...
RQ-1B-3.3 Pump chamber to vacu...
RQ-1B-3.4 Record thrust generated...
RQ-1B-4 Calculate mass flow and...
RQ-1B-4.1 Determine and quantify...
RQ-1B-4.2 Tune analytical models ...
RQ-1B-4.3 Compare theoretical and...
RQ-1B-4.4 Critically evaluate result...
RQ-1B-5 Determine the pressure ...
RQ-1B-5.1 Calculate sublimation ra...
RQ-1B-5.2 Compare sublimation ra...
RQ-1B-5.3 Infer feedline pressure d...
RQ-1B-5.4 Critically evaluate result...

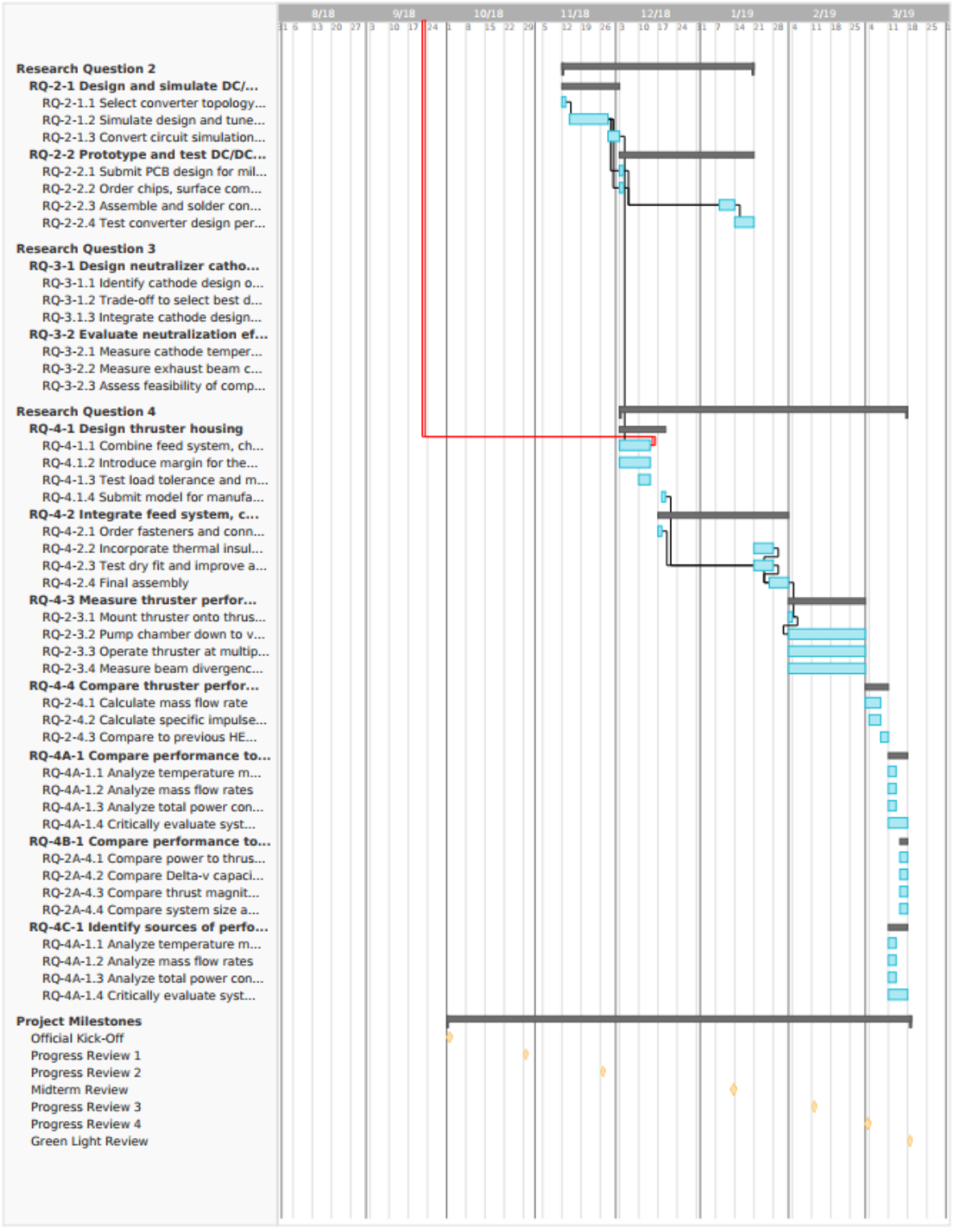

Figure A.5: Gantt chart timeline planning for thesis project.

B

Figures

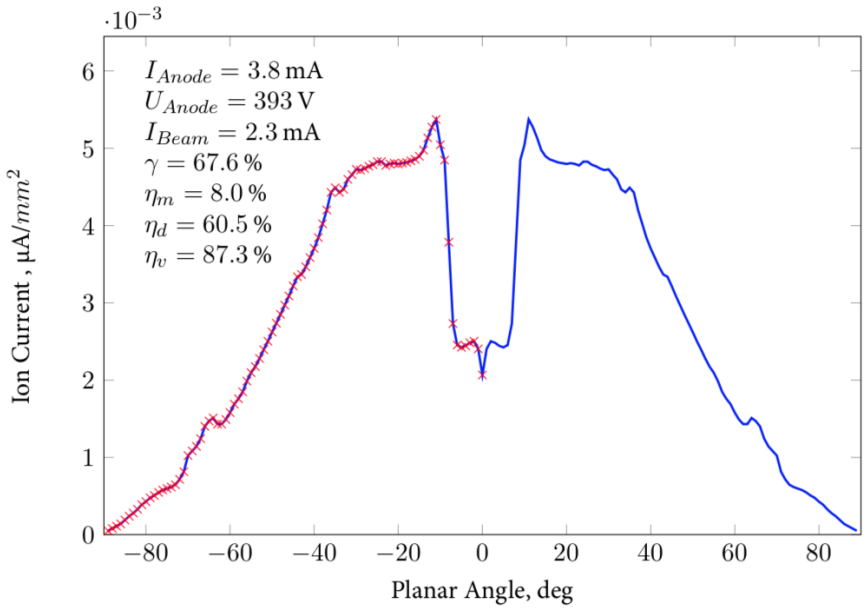

Figure B.1: Plasma plume profile measured with first µACFT CubeSat EM, using xenon propellant [91].

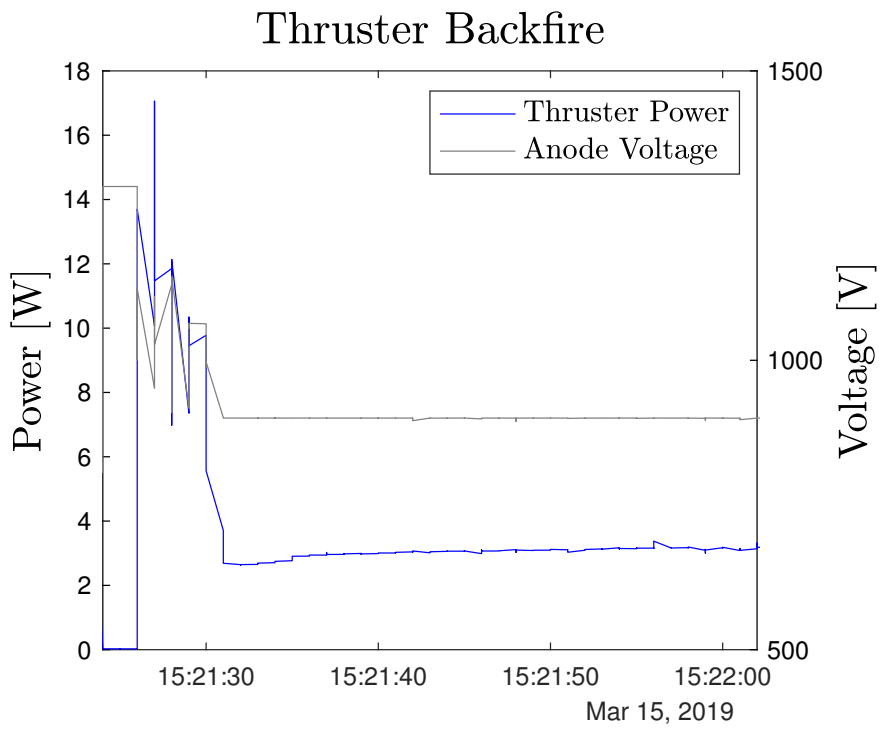

Figure B.2: Ignition of iodine plasma inside the feed system of iodine µACFT with an anode potential of 1300 V.

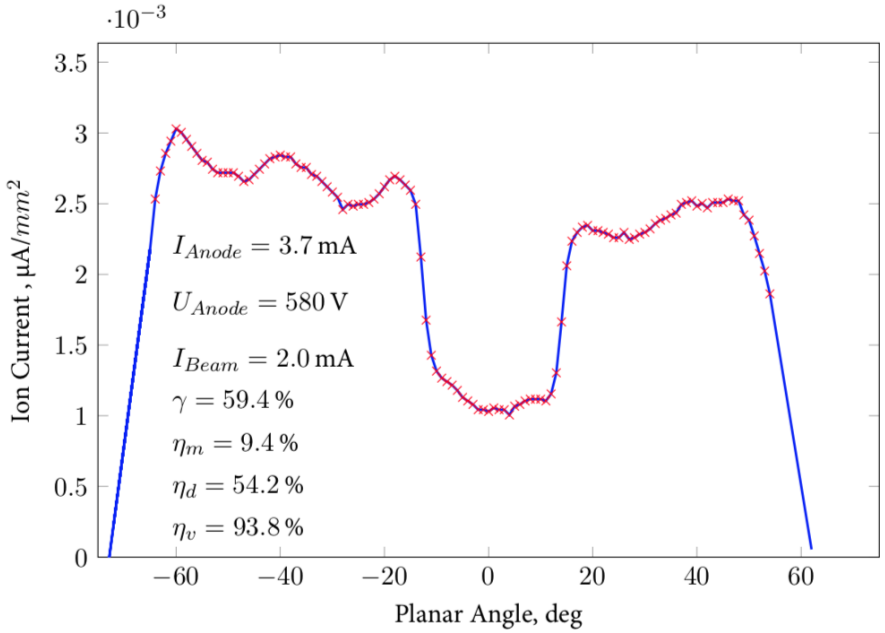

Figure B.3: Plasma plume profile measured with first µACFT CubeSat EM, using xenon propellant [91].

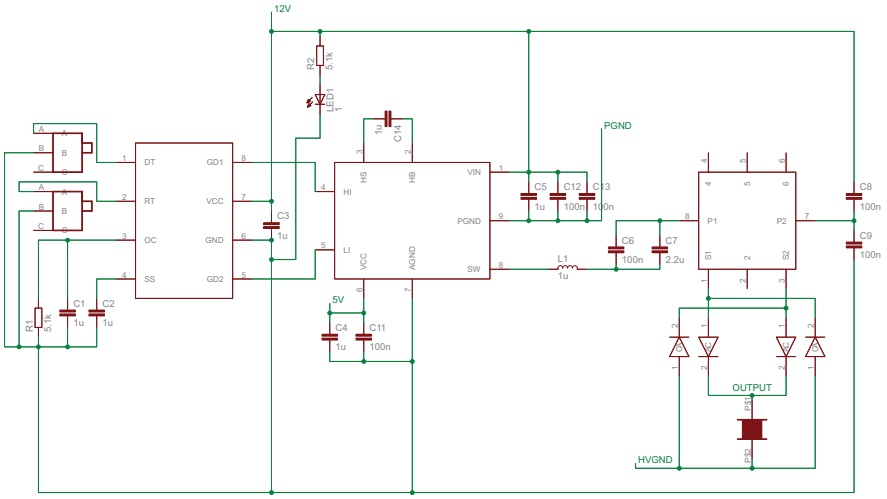

Figure B.4: Schematic diagram of DC/DC converter design in Eagle.

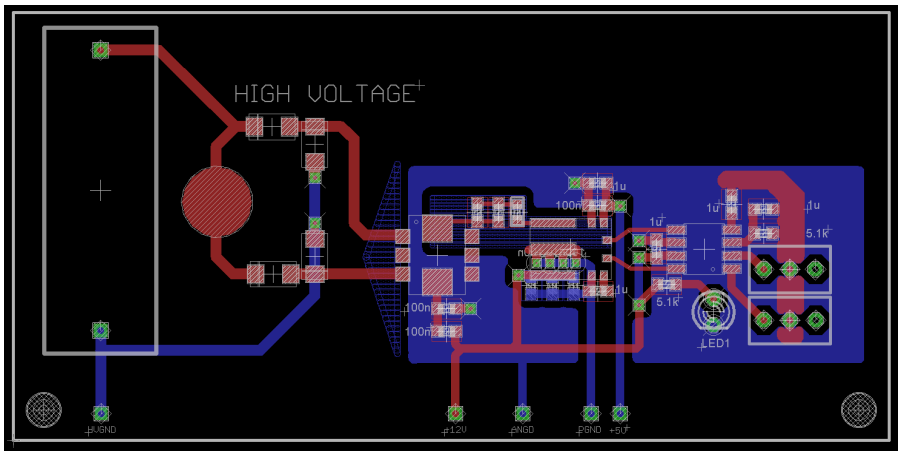

Figure B.5: DC/DC converter PCB design in Eagle.

Bibliography

[1] Accuratus. Boron nitride, bn ceramic properties, 2013. URL https://www.accuratus.com/boron.html.

[2] United Launch Alliance. *Atlas 5 User's Manual*, March 2010.

[3] United Launch Alliance. *Delta IV Launch Services User's Guide*, 6 2013.

[4] Arianespace. *Ariane 5 User's Manual*, 7 2011.

[5] Arianespace. *Vega User's Manual*, April 2014.

[6] K. Barbalace. Periodic table of elements - sorted by 1st ionization potential (ev). https://environmentalchemistry.com/yogi/periodic/1stionization.html, 1995-2018. Accessed: 2018-08-15.

[7] S. Barral. First experimental characterization of a pulsed plasma thruster with non-volatile liquid propellant. *Space Propulsion Conference*, 5 2014.

[8] D. Bock, P. Laufer, and M. Tajmar. Revolutionary propulsion for future spacecraft: Field emission thruster developments at tu dresden towards their first flight application. In *2017 30th International Vacuum Nanoelectronics Conference (IVNC)*, pages 96–97, 7 2017. doi: 10.1109/IVNC.2017.8051560.

[9] J. Bouwmeester, M. Langer, and E. Gill. Survey on the implementation and reliability of CubeSat electrical bus interfaces. *CEAS Space Journal*, 9:163–173, 9 2016. doi: 10.1007/s12567-016-0138-0. URL http://link.springer.com/10.1007/s12567-016-0138-0.

[10] J. E. Brandenburg, J. Kline, and D. Sullivan. The microwave electro-thermal (met) thruster using water vapor propellant. *IEEE Transactions on Plasma Science*, 33(2 II):776–782, 2005. doi: 10.1109/TPS.2005.845252.

[11] Juan Manuel Camacho and Victor Sosa. Alternative method to calculate the magnetic field of permanent magnets with azimuthal symmetry. *Revista mexicana de física E*, 59:8–17, 06 2013.

[12] E. Cardiff and G. Marr. Propulsion options for the lisa mission. 40th AIAA Joint Propulsion Conference, 2004. doi: 10.2514/6.2004-3440. URL https://doi.org/10.2514/6.2004-3440.

[13] D. L. Carroll, J. M. Cardin, R. L. Burton, G. F. Benavides, N. Hejmanowski, C. Woodruff, K. Bassett, D. King, J. Laystrom-Woodard, L. Richardson, C. Day, K. Hageman, and R. Bhandari. Propulsion unit for cubesats (PUC). 2015.

[14] A. Cervone, A. Mancas, and B. Zandbergen. Conceptual design of a low-pressure micro-resistojet based on a sublimating solid propellant. *Acta Astronautica*, 108:30–39, 2015. doi: 10.1016/j.actaastro.2014.12.003.

[15] X. Chen, K. Dickens, E. H. Choi, and M. Kristiansen. Space-charge limited current for 1-d cylindrical diodes. In *Digest of Technical Papers. PPC-2003. 14th IEEE International Pulsed Power Conference (IEEE Cat. No.03CH37472)*, volume 1, pages 467–470 Vol.1, June 2003. doi: 10.1109/PPC.2003.1277752.

[16] L. J. Cheney. Development of safety standards for CubeSat propulsion systems. Master's thesis, California Polytechnic State University, 2014.

[17] CD Child. Discharge from hot cao. *Physical Review (Series I)*, 32(5):492, 1911.

[18] E. Choueiri. A critical history of electric propulsion: The first 50 years (1906-1956). *Journal of Propulsion and Power*, 20(2):193 – 203, 2004. URL https://alfven.princeton.edu/publications/choueiri-jpp-2004.

[19] S. Ciaralli, M. Coletti, and S.B. Gabriel. Results of the qualification test campaign of a pulsed plasma thruster for cubesat propulsion (pptcup). *Acta Astronautica*, 121:314 – 322, 2016. ISSN 0094-5765. doi: https://doi.org/10.1016/j.actaastro.2015.08.016. URL http://www.sciencedirect.com/science/article/pii/S0094576515003318.

[20] Air Force Space Command. *Range Safety User Requirements Manual Volume 3 - Launch Vehicles, Payloads, and Ground Suppourt Systems Requirements*, 7 2004. Certified By: Col. Billy Colwell.

[21] PC/104 Embedded Consortium. *PC/104 Specification*, 10 2008. Version 2.6.

[22] R. W. Conversano and R. E. Wirz. Cubesat lunar mission using a miniature ion thruster. 7 2011. doi: 10.2514/6.2011-6083. URL http://arc.aiaa.org/doi/abs/10.2514/6.2011-6083.

[23] R. W. Conversano and R. E. Wirz. Mission capability assessment of cubesats using a miniature ion thruster. *Journal of Spacecraft and Rockets*, 50:1035–1046, 9 2013. doi: 10.2514/1.a32435. URL http://arc.aiaa.org/doi/10.2514/1.A32435.

[24] R. W. Conversano, D. M. Goebel, R. R. Hofer, T. S. Matlock, and R. E. Wirz. Development and initial testing of a magnetically shielded miniature hall thruster. *IEEE Transactions on Plasma Science*, 43(1): 103–117, Jan 2015. ISSN 0093-3813. doi: 10.1109/TPS.2014.2321107.

[25] G. E. Cook. Luni-solar perturbations of the orbit of an earth satellite. *Geophysical Journal of the Royal Astronomical Society*, 6(3):271–291, 1962.

[26] Quick Cut Gasket Rubber Corporation. Chemical resistance chart. http://www.quickcutgasket.com/pdf/Chemical-Resistance-Chart.pdf, 2014.

[27] D. G. Courtney. Development and characterization of a diverging cusped field thruster and a lanthanum hexaboride hollow cathode. Master's thesis, Massachusetts Institute of Technology, 2008.

[28] J. W. Dankanich. Low-thrust propulsion technologies, mission design, and application. In Thawar T. A., editor, *Aerospace Technologies Advancements*, chapter 12. IntechOpen, 2010. doi: 10.5772/6932. URL https://doi.org/10.5772/6932.

[29] J. W. Dankanich, K. A. Polzin, D. Calvert, and H. Kamhawi. The iodine satellite (isat) hall thruster demonstration mission concept and development. 50th AIAA/ASME/SAE/ASEE Joint Propulsion Conference, 7 2014.

[30] J. W. Dankanich, J. J. Szabo, B. Pote, S. R. Oleson, and H. Kamhawi. Mission and system advantages of iodine hall thrusters. 50th AIAA/ASME/SAE/ASEE Joint Propulsion Conference, 7 2014. doi: 10.2514/6.2014-3905. URL http://arc.aiaa.org/doi/10.2514/6.2014-3905.

[31] S. De Simone, C. Adragna, C. Spini, and G. Gattavari. Design-oriented steady-state analysis of LLC resonant converters based on FHA. pages 200–207, 2006. doi: 10.1109/speedam.2006.1649771. URL http://ieeexplore.ieee.org/document/1649771/.

[32] R. A. Dressler, Y. H. Chiu, and D. J. Levandier. Iodine electric propulsion thrusters. 8 2003. US Grant US6609363B1. Filed Dec. 26, 2000.

[33] T. Duerbaum. First harmonic approximation including design constraints. In *INTELEC - Twentieth International Telecommunications Energy Conference (Cat. No.98CH36263)*, pages 321–328, Oct 1998. doi: 10.1109/INTLEC.1998.793519.

[34] M. C. Eckstein. Optimal station keeping by electric propulsion with thrust operation constraints. *Celestial mechanics*, 21(2):129–147, Feb 1980. ISSN 1572-9478. doi: 10.1007/BF01230889. URL https://doi.org/10.1007/BF01230889.

[35] European Cooperation for Space Standardization Secretariat. *ECCS System Glossary of Terms*, 9 2012.

[36] A. Garulli, A. Giannitrapani, M. Leomanni, and F. Scortecci. Autonomous low-earth-orbit station-keeping with electric propulsion. *Journal of Guidance, Control, and Dynamics*, 34, 2011. doi: 10.2514/1.52985. URL https://doi.org/10.2514/1.52985.

[37] G. S. Gedeon. Tesseral resonance effects on satellite orbits. *Celestial Mechanics*, 1(2):167–189, 1969.

[38] E. Gill, P. Sundaramoorthy, J. Bouwmeester, B. Zandbergen, and R. Reinhard. Formation flying within a constellation of nano-satellites: The qb50 mission. *Acta Astronautica*, 82(1):110 – 117, 2013. ISSN 0094-5765. doi: https://doi.org/10.1016/j.actaastro.2012.04.029. URL http://www.sciencedirect.com/science/article/pii/S0094576512001440. 6th International Workshop on Satellite Constellation and Formation Flying.

[39] Dan M Goebel and Ira Katz. Fundamentals of Electric Propulsion: Ion and Hall Thrusters. page 493.

[40] F. G. Hey. Entladungskammer für ein ionentriebwerk, 1 2017. EP 3 219 987 A1.

[41] F. G. Hey. *Micro Newton Thruster Development*. Springer Vieweg, 1 edition, 2018. doi: 10.1007/978-3-658-21209-4.

[42] F. G. Hey. Propellant delivery system, electric thruster, and method of operating an electric thruster, 1 2019. WO 2019020330A1.

[43] F. G. Hey, M. Vaupel, C. Braxmaier, M. Tajmar, A. Sell, E. Kalrheinz, D. Weise, N. Saks, and U. Johann. Hempt downscaling, way forward to the first em for cubesat applications. 35th International Electric Propulsion Conference, 10 2017. IEPC-2017-274.

[44] F. G. Hey, U. Johann, and G. Kornfeld. Cusped field thruster, 9 2018. US 20180266403A1.

[45] K. Holste, W. Gärtner, D. Zschätzsch, S. Scharmann, P. Köhler, P. Dietz, and P. J. Klar. Performance of an iodine-fueled radio-frequency ion-thruster. *The European Physical Journal D*, 72(1), Jan 2018. doi: 10.1140/epjd/e2017-80498-5. URL https://doi.org/10.1140/epjd/e2017-80498-5.

[46] V. Hruby, M. Gamero-Castaño, P. Falkos, and S. Shenoy. Micro newton colloid thruster system development. 2001.

[47] IPEX. Chemical resistance guide, thermoplastics and elastomers. http://www.gilsoneng.com/reference/ChemRes.pdf, 2001.

[48] ISRO. *Auxiliary Satellite User's Manual*, 12 1999.

[49] H. Kamhawi, T. Haag, G. Benavides, T. Hickman, T. Smith, G. Williams, J. L. Myers, K. A. Polzin, J. W. Dankanich, L. Byrne, J. J. Szabo, and L. P. Lee. Overview of iodine propellant hall thruster development activities at NASA glenn research center. 52nd AIAA/SAE/ASEE Joint Propulsion Conference, 7 2016. doi: 10.2514/6.2016-4729. URL http://arc.aiaa.org/doi/10.2514/6.2016-4729.

[50] A. Keller. *Feasibility of down-scaled HEMP Thruster*. PhD thesis, Justus-Liebig-Unicersity Giessen, 12 2013.

[51] A. T. Klesh, J. D. Baker, J. Bellardo, J. Castillo-Rogez, J. Cutler, L. Halatek, E. G. Lightsey, N. Murphy, and C. Raymond. INSPIRE: Interplanetary nanospacecraft pathfinder in relevant environment. 9 2013. doi: 10.2514/6.2013-5323. URL http://arc.aiaa.org/doi/10.2514/6.2013-5323.

[52] N. Koch, M. Schirra, S. Wies, A. Lazurenko, B. van Reijen, J. Haderspeck, A. Genovese, and P. Holtmann. The hempt concept - a survey on theoretical considerations and experimental evidences. 32nd International Electric Propulsion Conference, 9 2011.

[53] N. G. Kottke. Cathode development for new space applications. Master's thesis, Technische Universität Braunschweig, 9 2018.

[54] D. Krejci and P. Lozano. Space propulsion technology for small spacecraft. 106(3):362–378, March 2018.

[55] U. Kvell, M. Puusepp, F. Kaminski, J. E. Past, K. Palmer, T. A. Grönland, and M. Noorma. Nanosatellite orbit control using MEMS cold gas thrusters. *Proceedings of the Estonian Academy of Sciences*, 63:279, 2014. doi: 10.3176/proc.2014.2s.09. URL http://www.kirj.ee/?id=23803&tpl=1061&c_tpl=1064.

[56] Anas Lahrichi. Heat transfer modeling and simulation of masat1. 05 2017. doi: 10.13140/RG.2.2.29671.91047.

[57] Irving Langmuir. The effect of space charge and residual gases on thermionic currents in high vacuum. *Physical Review*, 2(6):450, 1913.

[58] K. Lemmer. Propulsion for CubeSats. *Acta Astronautica*, 134:231–243, 5 2017. doi: 10.1016/j.actaastro.2017.01.048. URL https://linkinghub.elsevier.com/retrieve/pii/S0094576516308840.

[59] I. Levchenko, K. Bazaka, Y. Ding, Y. Raitses, S. Mazouffre, T. Henning, P. J. Klar, S. Shinohara, J. Schein, L. Garrigues, M.n Kim, Dan Lev, F. Taccogna, Rod W. Boswell, C. Charles, H. Koizumi, Y. Shen, C. Scharlemann, M. Keidar, and S. Xu. Space micropropulsion systems for Cubesats and small satellites: From proximate targets to furthermost frontiers. *Applied Physics Reviews*, 5, March 2018. doi: 10.1063/1.5007734.

[60] I. Levchenko, S. Xu, G. Teel, D. Mariotti, M. L. R. Walker, and M. Keidar. Recent progress and perspectives of space electric propulsion systems based on smart nanomaterials. *Nature Communications*, 9, February 2018. doi: 10.1038/s41467-017-02269-7.

[61] R. G. Livesey. *Foundations of vacuum science and technology*. John Wiley Sons, Inc., 1998. Chapter 2: Flow of Gases Through Tubes and Orifices.

[62] D. Losa, M. Lovera, R. Drai, T. Dargent, and J. Amalric. Electric station keeping of geostationary satellites: a differential inclusion approach. In *Proceedings of the 44th IEEE Conference on Decision and Control*, pages 7484–7489, Dec 2005. doi: 10.1109/CDC.2005.1583369.

[63] L. Ma, J. Hu, and H. Qin. Design of half-bridge LLC resonant converter based on PLC810PG. pages 4431–4434, 9 2011. doi: 10.1109/iceceng.2011.6057926. URL http://ieeexplore.ieee.org/document/6057926/.

[64] T. Mai and A. Lebeda. Apcon AeroSpace & Defense GmbH, Prof.-Messerschmidt-Str. 4, 85577 Neubiberg, Germany. *st International Electric Propulsion Conference*, 2013.

[65] J. M. Martinez, D. Rafalskyi, and A. Aanesland. Iodine - a game-changing propellant for plasma based electric propulsion. Association Aeronautique et Astronautique de France, 5 2018. Space Propulsion.

[66] S. Mazouffre. Electric propulsion for satellites and spacecraft: established technologies and novel approaches. *Plasma Sources Science and Technology*, 25, 6 2016. doi: 10.1088/0963-0252/25/3/033002. URL http://stacks.iop.org/0963-0252/25/i=3/a=033002?key=crossref.9c6a720db6c50120415318928e7b3f98.

[67] A. Mehrparvar. *CubeSat Design Specification*, February 2014. Revision 13.

[68] J. Mueller. Thruster options for microspacecraft - a review and evaluation of existing hardware and emerging technologies. 7 1997. doi: 10.2514/6.1997-3058. URL http://arc.aiaa.org/doi/10.2514/6.1997-3058.

[69] J. Mueller, R. Hofer, and J. Ziemer. Survey of propulsion technologies applicable to cubesats. Joint Army-Navy-NASA-Air Force (JANNAF), 5 2010.

[70] L. Musinski, T. Liu, I. Eu, B. Gilchrist, A. Gallimore, J. Mirecki-Millunchick, and D. Morris. Nanoparticle Field Extraction Thruster (nanoFET): Introduction to, Analysis of, and Experimental Results from the "No-liquid" Configuration. 2008.

[71] NASA. Mars cube one (marco) mission overview, 2019. URL https://www.jpl.nasa.gov/cubesat/missions/marco.php.

[72] R. Nugent and J. Puig-Suari. *6U CubeSat Design Specification*, 7 2018. Revision 1.0.

[73] A. Poghosyan and A. Golkar. Cubesat evolution: Analyzing cubesat capabilities for conducting science missions. *Progress in Aerospace Sciences*, 88:59–83, January 2017. doi: 10.1016/j.paerosci.2016.11.002. URL http://linkinghub.elsevier.com/retrieve/pii/S0376042116300951.

[74] K. A. Polzin and H. Kamhawi. Propulsion system testing for the iodine satellite (iSAT) demonstration mission. 34th International Electric Propulsion Conference, 7 2015.

[75] K. A. Polzin, S. R. Peeples, J. F. Seixal, S. L. Mauro, B. L. Lewis, G. A. Jerman, D. H. Calvert, John Dankanich, H. Kamhawi, T. A. Hickman, J. J. Szabo, and L. Pote, B.and Lee. Propulsion system development for the iodine satellite (isat) demonstration mission. Joint Conference of 30th ISTS, 34th IEPC and 6th NSAT, 7 2014.

[76] K. A. Polzin, S. R. Peeples, J. Cecil, B. L. Lewis, F. Fraticelli, J. C. Molina, and J. P. Clark. Hardware in the loop testing of an iodine-fed hall thruster. 51st AIAA/SAE/ASEE Joint Propulsion Conference, 7 2015.

[77] K. A Polzin, S. R. Peeples, A. O. Burt, A. K. Martin, A. Martinez, J. F. Seixal, and S. Mauro. Development, demonstration, and analysis of an integrated iodine hall thruster feed system. 2016.

[78] K. A. Polzin, S. R. Peeples, A. Martinez, J. F. Seixal, S. Mauro, A. O. Burt, and J. L. Myers. Engineering model propellant feed system development for an iodine hall thruster demonstration mission. 52nd AIAA/SAE/ASEE Joint Propulsion Conference, 7 2016. doi: 10.2514/6.2016-4730. URL `http://arc.aiaa.org/doi/10.2514/6.2016-4730`.

[79] K. A. Polzin, J. F. Seixal, S. Mauro, A. O. Burt, A. Martinez, and S. R. Peeples. The iodine satellite (iSat) propellant feed system - design and demonstration. International Electric Propulsion Conference, 10 2017.

[80] D. Rafalskyi and A. Aanesland. A neutralizer-free gridded ion thruster embedded into a 1u cubesat module. International Electric Propulsion Conference, 10 2017.

[81] M. S. Rødgaard. *Piezoelectric transformer based power converters; design and control.* PhD thesis, Technical University of Denmark, 2012.

[82] A. Ruggiero, P. Pergola, S. Marcuccio, and M. Andrenucci. Low-thrust maneuvers for the efficient correction of orbital elements. 32nd International Electric Propulsion Conference, 9 2011.

[83] Jafar Safarian and Thorvald A. Engh. Vacuum evaporation of pure metals. *Metallurgical and Materials Transactions A*, 44(2):747–753, Feb 2013. ISSN 1543-1940. doi: 10.1007/s11661-012-1464-2. URL `https://doi.org/10.1007/s11661-012-1464-2`.

[84] C. Sarda, K.and Grant, S. Eagleson, D. D. Kekez, and R. E. Zee. Canadian advanced nanospace experiment 2 orbit operations: two years of pushing the nanosatellite performance envelope. 2010.

[85] K. Sarda, C. Grant, S. Eagleson, D. D. Kekez, and R. E. Zee. Canadian advanced nanospace experiment 2: on-orbit experiences with a three-kilogram satellite.

[86] Brian Sauser, Ryan Gove, Eric Forbes, and Jose Emmanuel Ramirez-Marquez. Integration maturity metrics: Development of an integration readiness level. *Information Knowledge Systems Management*, 9:17–46, 01 2010.

[87] C. A. Scharlemann and T. M. York. Pulsed plasma thruster using water propellant, part 11: Thruster operation and performance evaluation. 39th AIAA/ASME/SAE/ASEE Joint Propulsion Conference, 2003.

[88] J. Schein, A. Gerhan, F. Rysanek, and M. Krishnan. Vacuum arc thruster for CubeSat propulsion. page 8, 2003.

[89] M. Schmid. Vapor pressure calculator. `https://www.iap.tuwien.ac.at/www/surface/vapor_pressure`, 2013-2017.

[90] J. Schoolcraft, A. Klesh, and T. Werne. Marco: Interplanetary mission development on a cubesat scale. 2017. doi: DOI10.1007/978-3-319-51941-8_10. in *Space Operaitons: Contributions from the Global Community* by C. Cruzen et al.

[91] M. Schramm. Entwicklung und test eines µHEMPT-engineering-models für die anwendung auf einem CubeSat. Master's thesis, Institut für Raumfahrtsysteme der Universität Stuttgart, 2017.

[92] D. Selva and D. Krejci. A survey and assessment of the capabilities of Cubesats for Earth observation. *Acta Astronautica*, 74:50–68, 5 2012. doi: 10.1016/j.actaastro.2011.12.014. URL `http://linkinghub.elsevier.com/retrieve/pii/S0094576511003742`.

[93] MHI Launch Services. *H-IIA User's Manual*, February 2015.

[94] F Sharipov. Rarefied gas dynamics and its applications to vacuum technology. Vacuum in Accelerators: Specialized Course of Conference, 2007.

[95] SpaceX. *Payload User's Guide*, 10 2015.

[96] Starsem. *Soyuz User's Manual*, April 2001.

[97] STMicroelectronics. *An introduction to LLC resonant half-bridge converter*, 9 2008. AN2644 Application Note, Revision 2.

[98] D. R. Stull. Vapor pressure of pure substances. organic and inorganic compounds. *Industrial & Engineering Chemistry*, 39(4):517–540, 1947. doi: 10.1021/ie50448a022. URL https://doi.org/10.1021/ie50448a022.

[99] J. J. Szabo, M. Robin, S. Paintal, B. Pote, V. Hruby, and C. Freeman. Iodine propellant space propulsion. 33rd International Electric Propulsion Conference, 10 2013.

[100] G. W. Thomson. The antoine equation for vapor-pressure data. *Chemical Reviews*, 38(1):1–39, 1946. doi: 10.1021/cr60119a001. URL https://doi.org/10.1021/cr60119a001. PMID: 21016992.

[101] M. Tittu Varghese, B. T. C. Zandbergen, M. Mihailovic, J. F. Creemer, and P. M. Sarro. A silicon-based mems resistojet for propelling cubesats. 2011.

[102] A. Tomaszuk and A. Krupa. High efficiency high step-up DC/DC converters - a review. *Bulletin of the Polish Academy of Sciences: Technical Sciences*, 59(4):475–483, 12 2011. ISSN 0239-7528. doi: 10.2478/v10175-011-0059-1. URL http://content.sciendo.com/view/journals/bpasts/59/4/article-p475.xml.

[103] M. Tsay. Flight development of iodine BIT-3 RF ion propulsion system for SLS EM-1 CubeSats. AIAA/USU Joint Conference, 8 2016.

[104] M. Tsay, J. Frongillo, K. Hohman, B. K. Malphrus, and M. Drive. LunarCube: A deep space 6U CubeSat with mission enabling ion propulsion technology. page 8, 2015.

[105] M. Tsay, J. Frongillo, and J. Zwahlen. Maturation of iodine fueled bit-3 rf ion thruster and rf neutralizer. In *52nd AIAA/SAE/ASEE Joint Propulsion Conference*, page 4544, 2016.

[106] A. R. Tummala and A. Dutta. An overview of cube-satellite propulsion technologies and trends. *Aerospace*, 12 2017. doi: doi:10.3390/aerospace4040058.

[107] C. Underwood, S. Pellegrino, V. J. Lappas, C. P. Bridges, and J. Baker. Using CubeSat/microsatellite technology to demonstrate the autonomous assembly of a reconfigurable space telescope (AAReST). *Acta Astronautica*, 114:112–122, 9 2015. doi: 10.1016/j.actaastro.2015.04.008. URL http://linkinghub.elsevier.com/retrieve/pii/S0094576515001642.

[108] T. G. E. van't Klooster. Development of a LaB_6 cathode for micro electric thrusters. Master's thesis, TU Delft, 5 2018.

[109] S Varoutis, D Valougeorgis, O Sazhin, and F Sharipov. Rarefied gas flow through short tubes into vacuum. *Journal of Vacuum Science & Technology A: Vacuum, Surfaces, and Films*, 26(2):228–238, 2008.

[110] M. Vaupel. Development and test of a first generation mμhempt engineering model. Master's thesis, Philipps University Marburg, 1 2017.

[111] M. Vaupel. The next generation milli-hewton μHEMPT as potential main thruster for small satellites. International Electric Propulsion Conference, 9 2017.

[112] Vitrex. *PEEK 450G Material Properties*, 7 2014. URL https://www.victrex.com/~/media/datasheets/victrex_tds_450g.pdf.

[113] V. V. Volotsuev, V. V. Salmin, S. F. Safronov, V. V. Stratilatov, I. S. Tkachenko, S. S. Raube, S. V. Shikhanov, and E. G. Shikhanova. Application of electric propulsion for low earth orbit station keeping. *Procedia Engineering*, 185:254 – 260, 2017. ISSN 1877-7058. doi: https://doi.org/10.1016/j.proeng.2017.03.338. URL http://www.sciencedirect.com/science/article/pii/S1877705817314923. Electric Propulsions and Their Application.

[114] A. H. Weber and S. C. Kirsch. The vapor pressure of liquid bismuth between 603 and 638°c. *Phys. Rev.*, 57:1042–1044, 6 1940. doi: 10.1103/PhysRev.57.1042. URL https://link.aps.org/doi/10.1103/PhysRev.57.1042.

[115] N. K. Weiser. Dual high-voltage power supply for use on board a cubesat. 6 2014.

[116] W. P. Wright and P. Ferrer. Electric micropropulsion systems. *Progress in Aerospace Sciences*, 74:48–61, April 2015. doi: 10.1016/j.paerosci.2014.10.003. URL http://linkinghub.elsevier.com/retrieve/pii/S0376042114000979.

[117] B. Yang. *Topology investigation of front end DC/DC converter for distributed power system*. Virginia Polytechnic Institute and State University, 9 2003. URL https://vtechworks.lib.vt.edu/handle/10919/28982.

[118] B. Yang. Topology investigation of front end dc/dc converter for distributed power system. 9 2003. URL https://vtechworks.lib.vt.edu/handle/10919/28982.

[119] B. Zandbergen. Micropropulsion systems for cubesats. Von Karman Institute for Fluid Dynamics, 1 2013.

[120] J. K. Ziemer and M. Gamero-Castano. Colloid micro-newton thruster development for the st7-drs and lisa missions. 41st AIAA/ASME/SAE/ASEE Joint Propulsion Conference, 7 2005.

[121] J. K. Ziemer and S. M. Merkowitz. Microthrust propulsion of the lisa mission. 40th AIAA Joint Propulsion Conference, 7 2004.